Universidade do Minho
Escola de Ciências

Paulo Miguel Babo Cunha Salvador

Deposition and characterization of CdS and ZnO:Al thin films for Cu(In,Ga)Se$_2$ solar cells

outubro de 2016

Universidade do Minho
Escola de Ciências

Paulo Miguel Babo Cunha Salvador

Deposition and characterization of CdS and ZnO:Al thin films for Cu(In,Ga)Se$_2$ solar cells

Dissertação de Mestrado,
Mestrado em Física Aplicada

Trabalho realizado sob orientação do
Professor Dr. João Pedro Santos Hall Agorreta Alpuim
e do
Dr. Sascha Sadewasser

outubro de 2016

ACKNOWLEDGMENTS

Firstly, I want to express my sincere thanks to my practical tutor Dr. Pedro Salomé, whose support was indeed exceptional, for his constant patience and guidance throughout the entire work, and for his profound knowledge on each small step of this thesis. Also, my sincere appreciations to my INL tutor Dr. Sascha Sadewasser, head of the LaNaSC (laboratory for nanostructured solar cells) group at INL, whose council, support and funding were fundamental to the fulfilment of this work. I would like to thank Professor Pedro Alpuim, who accepted to be my Universidade do Minho Supervisor and whose trust and confidence certainly assured possible the development of this project.

I also want to thank Dr. Nicoleta Nicoara, also member of the LaNaSC group, for the provided help in obtaining AFM imaging and in the CdS holder's design; Dr. Miriam Debs for the training and assistance provided during the XRD measurements, and Engineering Physics student Miriam Ahlberg for the aid on electrical and quantum efficiency measurements performed on the CIGS solar cells.

I am also truly appreciated for the warm environment created by all the remaining LaNaSC members, Dr. Kamal Abderrafi, Dr. Vanessa Iglesias and Dr. Rodrigo Andrade, and by all the remaining INL members.

Finally, the acknowledgment of my gratitude to my parents and brother, who always strongly supported me and encouraged me to keep on working forward throughout my academic path.

ABSTRACT

The purpose of this thesis is to establish a baseline methodology for the optimized deposition of CdS thin films by chemical bath deposition (CBD) and ZnO:Al thin films by atomic layer deposition (ALD), for the development of Cu(In,Ga)Se$_2$ (CIGS) solar cells at INL facilities. A background research on several optimized parameters is presented and taken in consideration for both layers' growth methodologies.

A detailed study on how the chemical bath deposition parameters affect the properties of the resulting CdS thin film is made. The reproducibility of CdS layers with thickness 50-70 nm is successfully shown. The studied parameters that were found to heavily affect the deposition were: i) the bath temperature; ii) the pH (indirectly, through the amount of ammonia); iii) the deposition time. A colour-thickness pattern established a naked-eye projection of the grown sample's thickness, which allows for a quick and quantitative evaluation of the deposited films. Further XRD measurements are presented, as well as a statistical particle analysis with the software *ImageJ* applied to optical microscopy images of the samples. Based on these analysis, a modelling for the transition between ion-by-ion deposition and cluster-by-cluster deposition was presented. Further works compass the development of a working sample holder and the production of a detailed experimental protocol.

Concerning the ZnO:Al depositions, ALD, which is a potential industrial friendly technique, was used. The study focused on evaluating the growth rates of the system and on understanding the thickness effects on the transmittance and resistance of the resultant films. Two aluminium doping quantities were also studied and an increase of the bandgap energy is confirmed with increasing aluminium doping. The sample with the lowest sheet resistance of 80 $\Omega.\square^{-1}$ of this work had a thickness of 735 nm, while presenting transmittance values averaging above 90 % for wavelengths values between 400-1200 nm. As part of understanding the thickness effects, scanning electron microscopy, atomic force microscopy and X-ray diffraction analysis were performed, revealing a correlation between the (110) planar orientation and the resistivity values.

Both CdS and ZnO:Al layers are then individually incorporated in (externally manufactured) CIGS solar cells and are characterized. The solar cell results showed that the CIGS layer does not survive the harsh growth conditions of the ALD processing, which demonstrates that more improvements in this technique are needed. Two solar cell devices with 60 nm and a 210 nm CdS layers present fill factors of 0.60 and 0.50 respectively, and efficiency values of 11.6 % and 9.8 %. These results demonstrate better electrical performances for the solar cell with the optimized 60 nm CdS layer, presenting an increase of 1.8 % efficiency with a 150 nm decrease in thickness, highlighting the importance of controlling the CdS deposition procedure.

Keywords: Semiconductors, Thin film solar cells, CdS buffer, ZnO:Al TCO, CIGS.

RESUMO

Esta tese tem como objetivo estabelecer uma metodologia de base para o crescimento otimizado de filmes finos de CdS por deposição em banho químico (CBD) e de ZnO:Al por *atomic layer deposition* (ALD), com o intuito de otimizar células solares de Cu(In,Ga)Se$_2$ (CIGS) nas infraestruturas do INL. Uma pesquisa base na otimização de vários parâmetros base é apresentada, considerando os respetivos métodos de deposição e materiais.

É efetuado um estudo detalhado na influência dos parâmetros de deposição do banho químico nas propriedades dos filmes de CdS resultantes. A reprodutibilidade da deposição de uma camada de 50-70 nm de espessura é assegurada. Os parâmetros estudados que mais afetam a deposição são: i) a temperatura; ii) o pH (indiretamente, a partir da quantidade de amónia); iii) o tempo da deposição. É estabelecido um padrão entre a cor do filme e um alcance de espessuras, para permitir uma aproximação rápida e quantitativa da espessura da amostra a olho nu. São apresentadas medidas de difração de raios-X, juntamente com uma análise estatística de partículas através do *software ImageJ* a imagens das amostras, recolhidas por microscopia ótica. Também foram desenvolvidos um suporte de substratos para a deposição e um protocolo experimental detalhado para o processo de CBD.

Para os filmes de ZnO:Al foi utilizada a técnica de ALD, que é uma técnica potencialmente amiga da indústria. Este estudo foca-se em avaliar os rácios de crescimento do sistema e em compreender os efeitos da espessura na transparência e na resistência dos filmes resultantes. Foram utilizadas duas diferentes quantidades de dopagem com alumínio, e foi confirmado um aumento na energia de hiato com o aumento de percentagem de alumínio nos filmes. A amostra com resistividade de folha inferior deste trabalho, com 80 $\Omega.\square^{-1}$, possuía 735 nm de espessura e apresentava uma média de valores de transmitância acima de 90 %, para comprimentos de onda compreendidos entre 400-1200 nm. Para compreender os efeitos da espessura nos filmes, utilizou-se microscopia eletrónica de varrimento, microscopia de força atómica e difração de raios-X, que revelaram uma correlação entre a orientação planar (110) e os valores de resistividade obtidos para cada amostra.

Ambos os filmes de CdS e de ZnO:Al são incorporados individualmente em células solares CIGS, externamente produzidas, e são caracterizadas. Os resultados das células solares demonstraram que a camada CIGS não sobrevive às condições severas do processo de ALD, o que revela que são necessários mais desenvolvimentos para esta técnica de deposição. Duas células solares com incorporação de CdS com espessuras de 60 nm e 210 nm apresentam valores de *fill factor* de 0.60 e 0.50, respetivamente, e eficiências de 11.6 % e 9.8 %. Estes resultados demonstram uma performance elétrica melhorada para a camada otimizada de CdS com 60 nm, apresentando um aumento de 1.8 % de eficiência com a redução de 150 nm de espessura, evidenciando a importância do controlo do processo de deposição de CdS.

Palavras-chave: Semicondutores, Células solares de filmes finos, CdS *buffer*, ZnO:Al óxido condutor e transparente, CIGS.

INDEX

LIST OF FIGURES

LIST OF TABLES

LIST OF ABBREVIATIONS, INITIALS AND ACRONYMS

AFM	Atomic force microscopy	QE	Quantum efficiency
ALD	Atomic layer deposition	RF	Radio-frequency
CB	Conduction band	r_i	Distance/radius
CBD	Chemical bath deposition	R_S	Sheet resistivity
CBM	Conduction band minimum	s	Substrate refractive index
CIGS	Cu(In,Ga)Se$_2$	SEM	Scanning electron microscopy
CVD	Chemical vapour deposition	SLG	Sola-lime-glass
d	Interplanar distance	SRH	Shockley-Read-Hall
DC	Direct current	T	Temperature
DEZ	Diethyl zinc	t	Thickness
e	Electron charge	TCO	Transparent conducting oxide
E_F	Fermi Energy	TMA	Trimethyl aluminium
E_g	Bandgap energy	T_R	Transmittance
EQE	External quantum efficiency	V	Voltage
FF	Fill factor	VB	Valence band
FWHM	Full width at half maximum	V_{BI}	Built-in voltage
GIXRD	Grazing incident X-ray diffraction	VBM	Valence band maximum
GS	Grain size	V_{OC}	Open-circuit voltage
h	Planck's constant	w	Depletion width
I	Intensity	XRD	X-ray diffraction
IQE	Internal quantum efficiency	α	Absorption coefficient
J	Current density	β	Non-ideal factor
J_{ph}	Photovoltaic current density	η	Efficiency
J_{SC}	Short-circuit current density	λ	Wavelength
k	Shape factor	μ	Mobility
k_B	Boltzmann constant	ρ	Resistivity
MPP	Maximum power point	τ	Crystallite size
n	Refractive index	υ	Frequency
N_A	Concentration of acceptors	φ	Potencial
N_D	Concentration of donors	χ	Absorbance
n_e	Concentration of electrons		
n_f	Concentration of free charge carriers		
σ	Conductivity		
p_n	Concentration of holes		
PV	Photovoltaic		
PVD	Physical vapour deposition		

INTRODUCTION

1. MOTIVATION AND OBJECTIVES

Nowadays, the need for clean renewable energies is no longer a novelty. The tradition fossil fuel sources play many negative roles on our society. Reports on global warming are increasing, due to the emission of green-house gases, and fossils' supply and usage are not sustainable from economic and social perspectives. The answer for a better tomorrow dwell on the development of new and better clean energies to replace the "dirty" ones.

Photovoltaic cells, PV, commonly known as solar cells, are devices that directly transform solar light into direct current electricity, or DC. Among various kinds of renewable energy solutions, PV has attracted many attentions, due to its promising alternative advantages to other energy sources. Firstly, the sun is a reliable abundant energy source that constantly radiates an enormous amount of energy into Earth. Secondly, PV's operation does not require any direct green-house emission, noise or any kind of pollution. Lastly, it is a very reliable energy conversion technique. With low maintenance costs and no moving parts, the main challenge is to develop solar cells with increasing efficiency and reduced industrial production costs.

Thin film solar cells possess the advantage of requiring small amounts of materials, as the active photovoltaic layer of such cells has but a few micrometres of thickness. From within the broad range of thin film solar cell configurations and materials, $Cu(In,Ga)Se_2$ solar cells, or CIGS for short, present one of the most promising candidates.

CIGS is the material used as the absorber layer, i.e. the main layer that transforms the absorbed solar radiation into electricity, and is usually followed by a CdS buffer layer and an aluminium doped ZnO transparent conducting oxide (TCO) layer. These three layers are a common popular configuration, due to their excellent optical and electrical properties. Together, along with several other layer upgrades, this configuration has recently achieved a record certified performance of 22.6 % efficiency in ZSW, *Zentrum für Sonnenenergie- und Wasserstoff-Forschung Baden- Württemberg*, Germany [1].

The International Iberian Nanotechnology Laboratory, INL, has recently invested to help the scientific community to further develop the CIGS solar cells. The main objective of this thesis is to develop and understand a baseline growth procedures for the CdS buffer layer, aiming for thicknesses between 50-70 nm, and to evaluate the use of atomic layer deposition of the ZnO:Al TCO layer, aiming at the same time for the lowest sheet resistivity values and the highest

transparencies, while verifying if the deposition process does not harm the CIGS layer. The CdS baseline growth is performed with well-known chemical bath deposition, CBD, which stands the most promising deposition method for the buffer layer due to (still not completely understandable) better electrical performances over the CIGS stack solar cells. The ZnO:Al growth is performed with atomic layer deposition, ALD, as it is a most promising vacuum easy-to-scale deposition technique that produces thin films with great conformity. After optimization of these layers, they are introduced into CIGS solar cells, fabricated at Uppsala University, following the Ångström Solar Center baseline CIGS solar cell [2], to evaluate their performance.

Firstly, the *Introduction* part of this thesis starts with the discussion of some solar cell device topics in chapter 2, from the mechanisms that allow the radiation-electricity conversion to the characterization of solar cells. The third chapter is reserved to the stack of CIGS solar cell, where its structure is introduced and briefly described, while the forth chapter highlights some important considerations concerning the CdS buffer layer and the ZnO:Al TCO that will be optimized in this work. Finally, the last introductory chapter makes room for the description of all deposition and characterization techniques used throughout this work. Both chemical bath deposition and atomic layer deposition are described, atomic force microscopy (AFM) and scanning electron microscopy (SEM) are also portrayed. X-ray diffraction (XRD), optical spectroscopy and contact profilometry are then depicted, and the fifth chapter is closed with four-point probe.

Follows the *Results and Discussion* part of the thesis. Here, chapter 6 is reserved to the results of the CdS developments. Firstly, an evolution of the bath temperature experiment is performed to evaluate how the temperature of the deposition bath evolves overtime when immersed in an outer bath previously heated to 60º C. Then, a reproducibility test series is run, followed by an individual optimization of several deposition parameters. These parameters cover time, temperature, ammonia (and therefore pH), cadmium acetate and deposition bath quantity. A colour-thickness relation is then established, along with the XRD characterization and a final statistical particle analysis, with the software *ImageJ* applied on optical microscopy pictures of the samples.

The seventh chapter presents the results of the ZnO:Al developments. Four samples are grown, with different thicknesses and aluminium doping, and are characterized. Optical spectroscopy measurements are shown, along with bandgap and thickness calculations, of which the latter are confirmed with contact profilometry. Resistivity and sheet resistivity calculations are then introduced, followed by SEM and AFM results. Bragg-Brentano XRD is then applied to the

samples, and further calculus analysis are presented, performed with the Bragg's law, hexagonal structure equation and Sherrer equation to assess on some structural parameters.

The eighth chapter assesses the CIGS solar cell results, where solar cells are grown and characterized concerning their *J-V* curves, and thus their electrical performances, and external quantum efficiency measurements are performed as well.

Lastly, chapter 9, *Conclusions*, embraces all results and findings retrieved throughout the entire thesis, and chapter 10 presents future work proposals.

2. SOLAR CELL DEVICE TOPICS

2.1 Band structure background

In 1877, backed up by mathematical arguments, Ludwig Boltzmann introduced the concept of discrete energy levels of a physical system, such as a molecule. Boltzmann's rationale for such discrete system had its origins in his statistical thermodynamics and statistical mechanics [3]. Twenty years later, Max Planck, while developing a solution to the black-body radiation problem, empowered the notion of a discrete set of energy levels, along with the first glance of the nowadays quantum theory [4]. Then, in 1905, Einstein explained the photoelectric effect, on which he states [5]:

"*According to the assumption to be contemplated here, when a light ray is spreading from a point, the energy is not distributed continuously over ever-increasing spaces, but consists of a finite number of 'energy quanta' that are localized in points in space, move without dividing, and can be absorbed or generated only as a whole.*"

The energy levels of any physical system are, indeed, discrete. Consider, for example Niels Bohr's quantum model of 1913 of an atom, i.e. a system composed of its nucleus and electrons [6]. The electrons occupy discrete levels of energy, from the ground energy level, the state of lesser energy, to higher energy levels up to the point that the electron is free, unbound to the nucleus. An electron can absorb energy to jump into higher energy levels, or relax into lower energy levels, emitting energy in the process.

When two isolated atoms are brought closer together, their electronic structures will interact. Here, the Principle of Exclusion of Wolfgang Pauli comes into action, stating that two electrons cannot possess the very same quantum state. This results into a splitting of the discrete energy levels of the associated atoms into new levels. The more atoms come together, the more the splitting of energy levels, as is represented in figure 1.
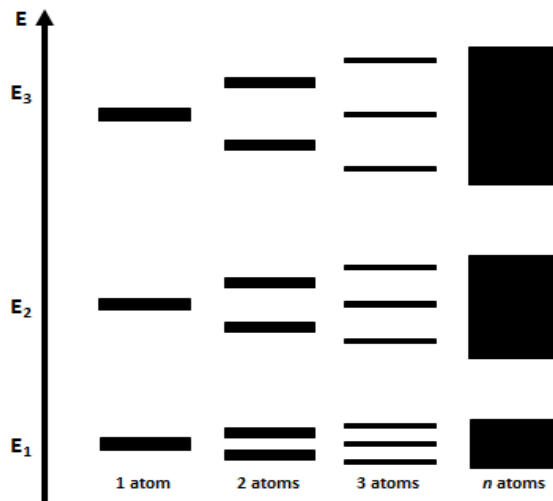
Figure 1 – Energy splitting electrical configuration schematization of an n*-atom system [7].*

Considering a solid, where a considerable amount of atoms are in close proximity, the splitting occurs in such numbers and into such closely spaced levels that they appear to form a continuous "band", as illustrated in the *N* atoms system of figure 1.

When the system is at rest, at 0 Kelvin temperature, all the electrons fill the inner orbit shells, i.e. the lowest energy positions, which results in many energy bands. The most important bands for the electrical conduction process are the highest energy occupied band and the lowest energy unoccupied band. The Fermi energy, E_F, is the energy of the electrons with the highest energy at absolute zero.

From these two bands, the upper band, i.e. the lowest energy unoccupied band, is the conduction band, CB, with which the electrons are very loosely bound. This is the band where the electrons contribute to carrier movement and thus the current flow in a solid. The second, i.e. the highest energy occupied band, is the valence band, VB. It represents the energy states of the atomic valence electrons which form covalent bonds that define the solid. In the case of semiconductors, both bands are separated by a forbidden region of energy, derived from the discrete set of electronic energy states, and this gap width is the bandgap energy, E_g. For undoped semiconductors, the Fermi energy, E_F, stands in the middle of the E_g.

The different materials concerning conductivity characteristics are sorted according to the values of their E_g. Semiconductors have their bandgap lower than insulators, and metals just present one band with no bandgap, due to a band overlap.

In the case of a semiconductor, at 0 Kelvin, the highest energy electrons of a system are in the valence band, thus no current flows, as no charge can move. When an electron is given energy, such as thermal or optical energy, it can jump from the VB into the CB. This process is different throughout the materials, as some present a direct bandgap while others have an indirect

bandgap. In a direct bandgap, the upper energy level of the VB is aligned with the lower energy level of the CB, and the electrons need only enough energy to cross the bandgap, i.e. higher than the bandgap energy, and the excess energy will be dissipated as heat when the electron crosses the bandgap. In the indirect bandgap case, the electrons need both energy and momentum in order to cross the bandgap into the CB, which can be given by a phonon (vibration particle) [8].

2.2 Electron-hole pairs generation and recombination processes

When an electron gets excited with sufficient energy to jump from the VB into the CB, an empty state is created in the VB where the electron was placed, called a hole. The hole is an effective positive charge by lack of a negative charge. If created by the promotion of the electron to upper bands, the process is called electron-hole pair generation.

Holes are as important as electrons when it comes to the conductivity of a material. If an electric field is applied, the holes will flow in the opposite direction of the electrons, which means that the conductivity of a material is not confined to the CB alone but to the VB as well.

Nevertheless, when no electric field is applied, there is no force to drive away electrons and holes from their generation sites. These electrons are in metastable states, and have a probability of losing part of their energy to either crystal vibrations or light emission (photons), transferring into lower energy empty states. This process is called relaxation. When an electron loses energy and fills the hole that was created during the generation of an electron-hole pair, recombination occurs.

Recombination has many facets, depending on the mechanism that is at stake. Radiative recombination occurs as a spontaneous emission of a photon, and it is more common in materials with a direct bandgap, as photons carry relative small momentum. Auger recombination occurs when the released energy is given to a third carrier, which is excited to a higher energy level without shifting into another band. This third carrier will usually lose its excess energy to thermal vibrations. This process is only significant in non-equilibrium conditions when the carrier density is very high, since it is a three-particle interaction and therefore less likely to occur.

Finally, the Shockley-Read-Hall recombination occurs when the electron is relaxed through energy states within the bandgap introduced by defects in the crystal. These energy states are denominated as deep-level traps, and can absorb differences in momentum between carriers.

[9] This is the dominant recombination process in semiconductor materials that contain defects, and in Cu(In,Ga)Se$_2$ solar cells. The three recombination courses are illustrated in figure 2.
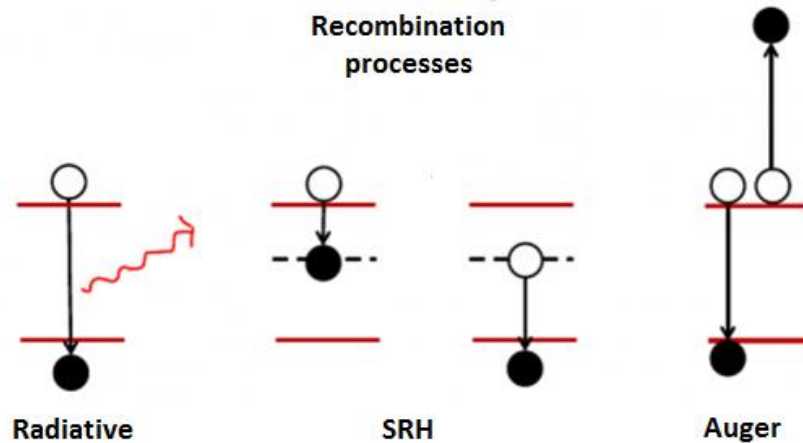
Figure 2 – Recombination processes illustrated [10].

2.3 Doping semiconductors and the p-n junction

Semiconductors can be subcategorized into intrinsic and extrinsic semiconductors. An intrinsic semiconductor is not doped, i.e. the free charge carriers (holes and electrons) are formed by the electron-hole pair genesis alone. An extrinsic semiconductor is a doped semiconductor, on which specific impurities are introduced in order to modify its electrical properties, turning it more suitable for optoelectronic applications such as solar cells.

The doping is consciously introduced by adding impurity atoms into the material. Impurity atoms which introduce unoccupied states in the VB are called acceptors, and create an excess of holes in the material. Thus the p-type doping denomination. In the other hand, impurity atoms that introduce occupied states just below or above the CB are called donors, as they create an excess of electrons in the material. The donors doping is called n-type doping, as electrons are introduced. While an undoped semiconductor has its E_F in the middle of the bandgap, it is therefore logical that this doping process will influence the E_F of the system, as the upper level electrons at 0 Kelvin will occupy different positions in doped materials. While the undoped semiconductor's Fermi energy stands in the middle of the bandgap, n-type doping brings the Fermi energy closer to the CB, and p-type doping reduces the Fermi energy to values just above the VB.

A p-n junction consists of a p-type and an n-type semiconductors brought together, and it possesses very interesting and important electronic characteristics. It can be built with similar semiconductors with different doping, forming a homo-junction, or by different materials, with

different bandgap values and electron affinities, resulting in a hetero-junction. In either case, an electric field is created across the junction of the two doped materials, and leads the charge carriers into opposite directions, turning possible the flow of the current [11].

The formation of the p-n junction in depicted in figure 3.
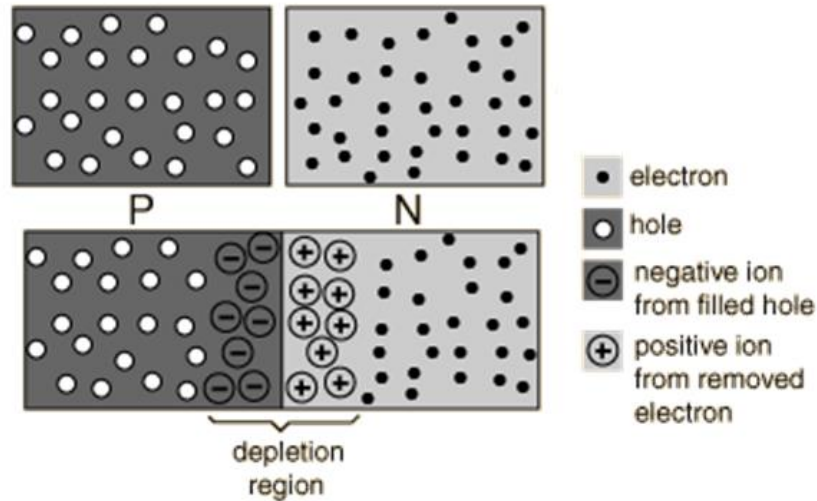
Figure 3 – P-n junction illustrated [12].

On the left and right side of figure 3 we have the p-type and n-type semiconductors, respectively. The excess holes and electrons start to diffuse, converting the donor and acceptor atoms into ions. A diffusion current is generated when the charge carriers diffuse across the junction and recombine, thereby creating an uneven charge distribution, which gives rise to an electric field, generating a drift current, that is empowered by further recombination processes. The physical volume on which the generated electric field spans, i.e. the region constituted of the ionized donors and acceptors, is called depletion region, or space-charge region, and the resulting potential from the integration of this electric field is denominated as built-in potential, V_{bi}. A stronger field eventually counteracts the diffusion current of the excess holes and electrons, and at equilibrium a steady state is established with no flow of electrons or holes, where the current is zero. The current generated by the flow of charge carriers due to the electric field is called the drift current.

Figure 4 schematically represents the process described above within a homojunction structure.
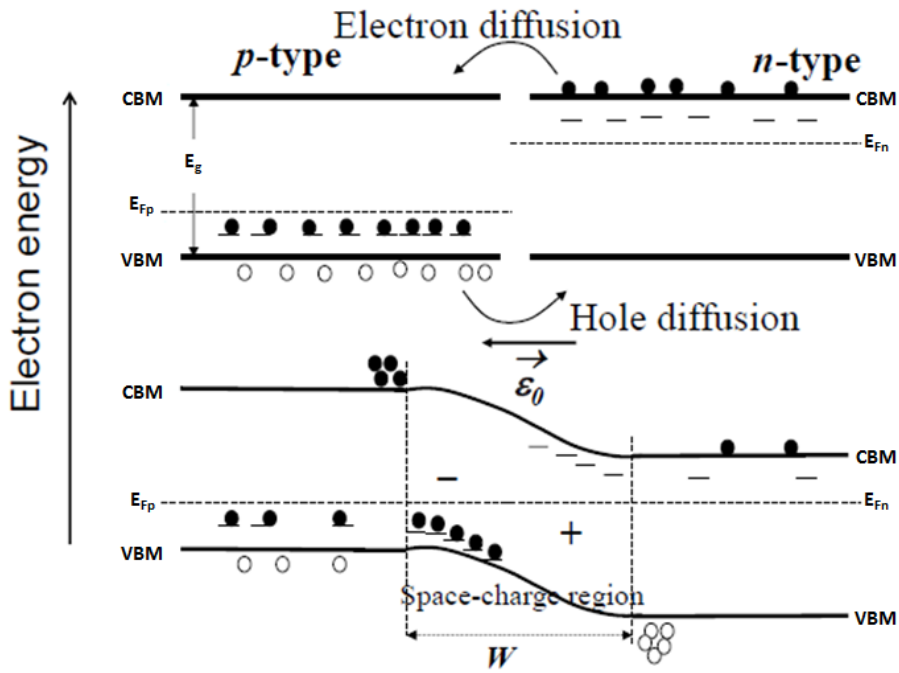
Figure 4 – P-n homojunction band structure schematically represented. CBM, E_F and VBM correspond to the conduction band minimum, the Fermi energy and the valence band maximum, respectively [13].

2.4 Current extraction mechanism

A p-n junction connected to two terminals is called a diode device, and a CIGS solar cell is basically a multi-structured hetero-junction device, in the way that it is formed of semiconductor layers on top of each other, each one of different materials and thus with different bandgap energies. Given so, a mechanism is needed in order to collect the energy of the electron-hole pairs created by the incident photons, since otherwise they will eventually recombine. The gathering of the electrons in the n-type side and holes in the p-side allows to collect the charges by the terminals of the diode. Due to the potential difference, the electrons collected from the n-type side will flow through the circuit to the p-type side through the circuit, creating a direct current, ultimately fed by incoming light [14].

2.5 Ideal diode and the solar cell characterization

Consider a diode at rest in the dark and at room temperature. An electric field is present in the p-n junction, which will prevent the electrons to move from the n-material to the p-material, and at the same time will pull out a much reduced amount of electrons from the n-material to the p-material, due to thermal energy, since the diode is at room temperature. Even in the dark, there is indeed a current flow, but it is very small when no bias is applied to the diode.

Applying an increasing external bias, the electrical barrier will be lowered up to the point that allows a significant amount of electrons to flow from the n-material across the p-material. And, within the same mechanism, the holes will flow from across the opposite direction. Both hole and electron flows contribute to the total current, which, in the case of an ideal diode, is described by equation 1.

$$J = J_0 \left(e^{\frac{qV}{k_B T}} - 1 \right)$$ *Eq. 1*

Here, J is the current density, J_0 is the dark saturation current density (which depends on the semiconductor material properties), V represents the applied external bias voltage, k_B stands for the Boltzmann constant and T is the crystal temperature.

A solar cell is basically a non-ideal diode with an intrinsic photocurrent density, J_{ph} in the presence of illumination. Given so, the equation that describes the total current of a solar cell is very similar to the ideal diode current equation, with a non-ideal factor, β, and the presence of the photocurrent density J_{ph}, described in equation 2 [15].

$$J = J_0 \left(e^{\frac{qV}{\beta k_B T}} - 1 \right) - J_{ph}$$ *Eq. 2*

Figure 5 graphically illustrates the electrical behaviour of a typical solar cell, under illumination and in the dark.
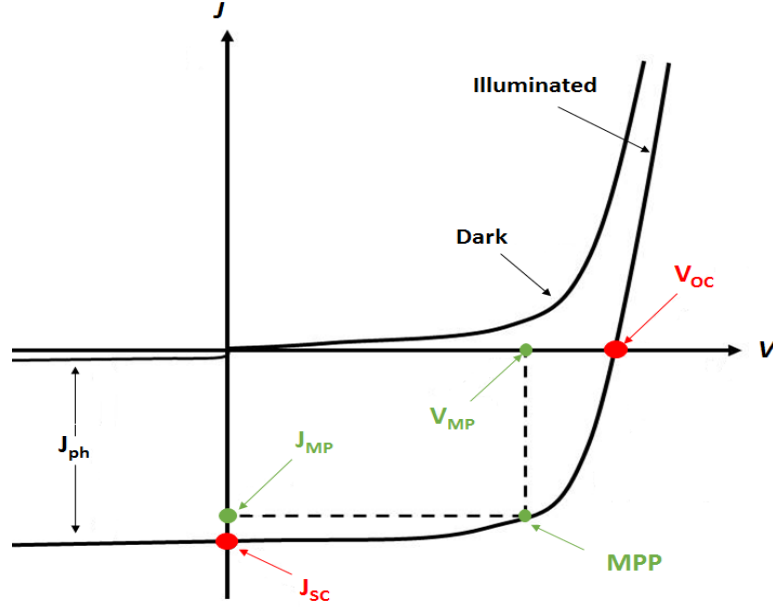
Figure 5 – Typical solar cell J-V plot, under illumination and in the dark. Main features highlighted: V_{oc} (open-circuit voltage), J_{sc} (short-circuit current density), V_{mp} (maximum power voltage), J_{mp} (maximum power current density) and MPP (maximum power point) [16].

From figure 5, several electrical parameters can be retrieved in order to characterize the solar cell electric performance.

J_{sc}, or short circuit current density, is defined as the current density that passes through a short circuit device when no bias is applied, and so it decreases with the bandgap energy of a material, since the wider the bandgap the fewer photons will have enough energy to create electron-hole pairs.

V_{oc}, or open circuit voltage, is the voltage when the forward bias diffusion current equals the photocurrent, i.e. when the total current flow is zero, and therefore is ruled by equation 3:

$$V_{oc} = \frac{\beta k_B T}{q} ln \left(\frac{J_{ph}}{J_0} - 1 \right)$$

Eq. 3

The semiconductor material properties will influence V_{oc}, as it has a direct impact on J_0. There is thereby a trade-off between the V_{oc} and J_{sc}, as it is expected, given that the output power is described by the direct multiplication of the voltage with the current flow as in equation 4.

$$P_{out} = V * I$$

Eq. 4

, where I is the current, and the conversion from current to current density is given by adding the area factor, A, as in equation 5:

$$J = \frac{I}{A}$$

Eq. 5

The point of maximum output power, or MPP in the figure 5, is obviously an important electrical parameter as well. As in equation 4, it is given by the direct multiplication of V_{MP} with J_{MP}, maximum power voltage and current density.

It is now most appropriate to define the fill factor, FF, and the efficiency, η, of a solar cell, which are the final parameters that determinate the electric performance of a solar cell. FF is basically the measure of how close the product of V_{MP} with J_{MP} is to the product of V_{oc} with J_{sc}, and is given by the ratio between them described in equation 6.

$$FF = \frac{V_{MP}J_{MP}}{V_{oc}J_{sc}}$$

Eq. 6

As for the efficiency, it is the ratio between the incoming power of the radiation, P_{in}, and the output power, P_{out}, as described in equation 7 [15]:

$$\eta = \frac{P_{out}}{P_{in}} = \frac{V_{MP}J_{MP}}{P_{in}} = \frac{V_{oc}J_{sc}FF}{P_{in}}$$

Eq. 7

Finally, stepping out of the electrical parameters that can be extracted from the J-V curves of a solar cell, one more important electrical behaviour is the quantum efficiency, QE, often subcategorized into internal quantum efficiency (IQE) and external quantum efficiencies (EQE). IQE is the ratio of the number or charge carriers produced by the solar cell to the number of photons absorbed by the solar cell, while EQE is the ratio of the number of charge carriers collected by the solar cell to all incident photons on the cell. Basically, IQE is not affected by reflections that occur in the front contact of the solar cell, while EQE accounts for the real performance of a solar cell [17].

Naturally, the QE depends on the energy of the photons that are radiated into the solar cell, i.e. the wavelength of the radiation, and on the bandgap energies of the solar cell. From EQE(λ) plots, it is possible to estimate bandgap values for the CIGS layer and the window layer, along with the J_{sc} of the device.

All *J-V* measurements are performed with the same light intensity, i.e. in AM1.5 conditions, with integrating power of 1000 W. The EQE(λ) measurements are usually performed after a calibration of the equipment, which is done by measuring the EQE of a silicon baseline solar cell and comparing it with the spectrum of the same silicon sample, intrinsically maintained within the software of the equipment. This way, the intensity of these measurements is relative, and not absolute.

3. CU(IN,GA)SE₂ SOLAR CELL

A CIGS solar cell consists of a hetero p-n junction, and its standard design embraces five thin layers, supported by a glass substrate, represented in figure 6.
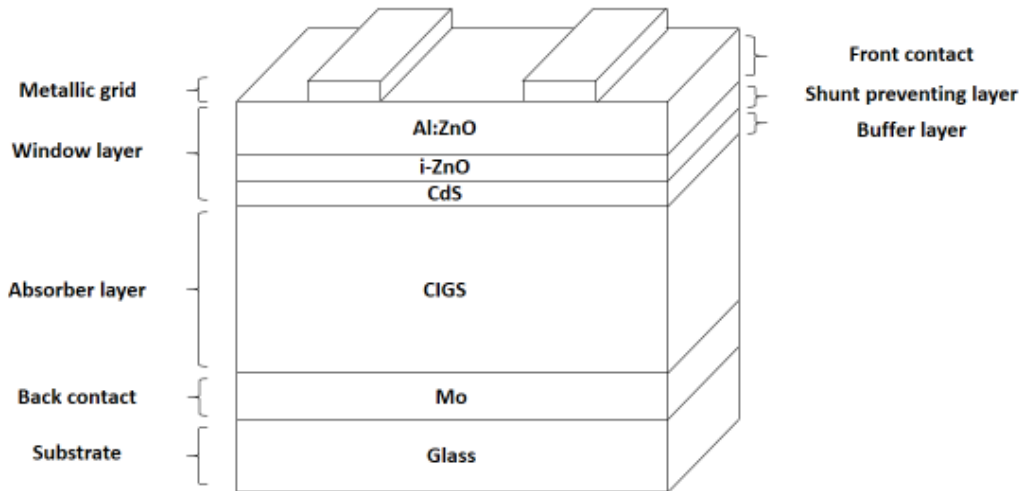
Figure 6 – Typical CIGS stack structure, not to scale.

Bottom to top, this structure consists in a glass substrate, followed by a molybdenum back contact on which the CIGS absorber layer is laid. An entire window layer follows, consisting in the CdS buffer layer, the shunt preventing intrinsic ZnO layer, i-ZnO, and the ZnO:Al front contact. Laboratory scale cells are usually equipped with a Ni-Al-Ni grid for current collection on the front contact [18]. Some cells also present an anti-reflective layer on top of the ZnO:Al layer, involving the grid in such way that the grid still touches the ZnO:Al front contact layer. The window layer constitutes the n-doped part of the p-n junction, while CIGS is moderately p-doped. The top ZnO layer is intentionally doped, while the doping in both CIGS and CdS layers is built on intrinsic defects in the material.

The resulting CIGS complex band diagram is given by figure 7. This diagram is representative from the EMPA CIGS solar cell, and it is important to note that the band diagram configuration might change with the configuration of the CIGS growth, i.e. deposition processes and layers' properties, which naturally is not constant between research groups. This figure represents but a suggestion of the band diagram of a typical CIGS solar cell.
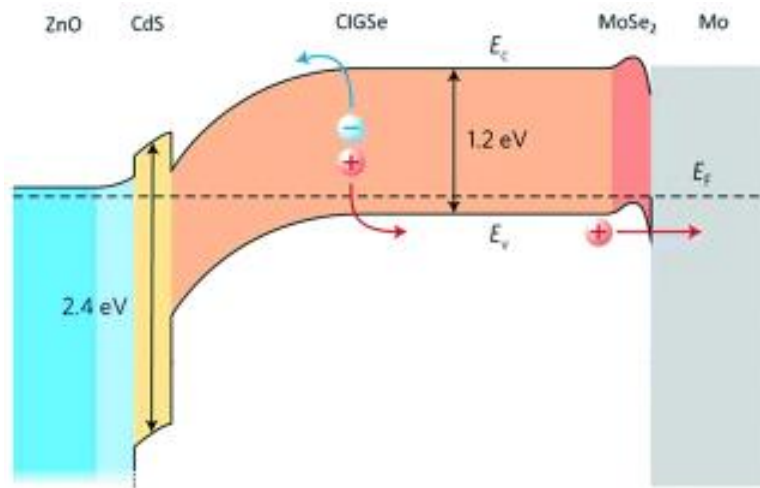
Figure 7 – CIGS heterojunction band diagram as discussed by the research group EMPA, not to scale [19].

Also, it should be noted that even nowadays the exact band bending located at each interface is the topic of several publications and discussion in the CIGS research community, hence its full explanation is out of the scope of this thesis.

Each layer will be further described in the next section, bottom to top, with special attention to the CdS buffer layer and to the ZnO:Al front contact layer. In this thesis the layers from Uppsala University (soda lime glass substrate, back contact Mo, absorber CIGS and Ni-Al-Ni grid) were combined with the ones grown and studied at INL (CdS buffer layer and ZnO:Al TCO). The description of the thicknesses and properties of the layers follows the Uppsala's CIGS solar cells because it is the state-of-art CIGS solar cell and because some layers were prepared in their facilities.

Each layer presents the respective deposition process used by Uppsala University as well, used as standard process for each steps in the Ångström Solar Centre. Further details can be found in the respective paper [2].

3.1 Substrate and back contact

Several substrates have been used for CIGS solar cells, such as glass, flexible steel or different types of plastics. As for the back contact, some materials have been investigated as well. Still, the most common substrate and back contact layer are soda lime glass (SLG) substrates and Mo back contacts, given the powerful combo they constitute. Beyond the mechanical support the SLG provides to the rest of the solar cell, it also provides Na atoms by diffusion into the CIGS layer, which has been proven to increase the efficiency of the solar cell for several reasons. It alters the structure of the layer, yielding a larger grain size and an overall better layer

morphology. A thin Mo back contact layer facilitates the Na atoms to diffuse into the CIGS, further empowering the solar cell [20, 21, 22].

Uppsala's deposition of Mo is the most common deposition technique for this layer, DC sputtering, aiming for 350 ± 20 nm and reaching typical sheet resistances of $0.6 \pm 0.1 \ \Omega.\square^{-1}$ [2]. The SLG substrates used are cleaned previous to the deposition.

3.2   CIGS absorber layer

$Cu(In,Ga)Se_2$ compound belongs to the semiconducting I-III-VI$_2$ materials that crystallizes in the tetragonal chalcopyrite structure. It is a p-type alloy resulting from the mixture of $CuInSe_2$ with $CuGaSe_2$, which have bandgap energies of 1.04 eV and 1.68 eV respectively [23].

As a tetragonal chalcopyrite structure material, CIGS has the interesting property of a variable bandgap energy, obtainable by varying the amount of Ga, from which naturally results a bandgap between 1.04 eV and 1.68 eV.

With respect to the solar spectrum, the optimal theoretical bandgap value stands close to 1.5 eV [24], while the empirical best performance for CIGS solar cells is found about 1.2 eV for [Ga]/([In]+[Ga]) of 0.2-0.3 [22].

The most common deposition techniques applied for CIGS absorber layer is thermal co-evaporation of Cu, In, Ga and Se. Common values of CIGS thicknesses are in the order of 1700 $\pm$ 300 nm, deposited by thermal co-evaporation. CIGS is a very complex semiconductor, and a full explanation of its properties is out of the scope of this thesis.

3.3   Buffer layer

The quality of the buffer layer has great influence on the efficiency gain of thin film solar cells, as it constitutes the n-type part of the p-n junction. The electrical performance of the thin film solar cells greatly depends upon the quality and thickness of the buffer layer. The standard CIGS solar cell uses an optimized buffer layer able to drive out the photo generated carriers with minimal absorption and recombination losses while coupling light to the junction. A wide bandgap is expected, as it provides more light towards the junction region and absorber layer, which is the most reliable way of increasing the efficiency of a solar cell.

Since this is an n-type material, its mobility values for holes are very low [25], and thus the light absorbed by this layer photo-generates charge carriers that will not contribute to the

photocurrent of the solar cell, for many carriers are lost to many electrical losses such as recombination.

For the buffer layer, CdS offers a very good n-type match to the p-type CIGS. It presents high photosensitivity and absorption and favourable bandgap energy of 2.4 eV. Furthermore, CdS is fairly easy to deposit by means of conventional deposition techniques such as CBD, which allows a large area conformal deposition with great homogeneity [26].

Attempts to replace the CdS have been made due to the toxicity of the material and due to the interruption of the vacuum process with the typical CBD deposition of the CdS. Nevertheless, CdS by CBD stands the most efficient buffer layer for CIGS cells [27]. A better analysis on the overall buffer layer characteristics and advantages within the solar cell are overviewed in chapter *4.1 CdS Buffer Layer*.

Common values for the CdS thickness in the literature are close to 60±10 nm [22].

3.4   Shunt preventing layer

The shunt preventing layer in CIGS solar cells is an intrinsic zinc oxide layer, i-ZnO, with bandgap energy of approximately 3.3 eV. It reduces the influence of shunt currents and electrical inhomogeneities over the device area of the solar cell [15], thus improving the performance of the cell. For small area solar cells, its omission can be beneficial, depending on the window layer materials chosen, but it is used in-between the conventional CIGS CdS-ZnO:Al window stack. For solar modules, due to the lower quality of the CIGS layer, this layer is always needed [28].

Radio-frequency (RF) sputtering aiming for 90 nm i-ZnO is the most common configuration of this layer for CIGS solar cells [2].

3.5   Transparent conductive oxide

The role of this layer is to allow the passage and collection of the current, and at the same time to be as transparent as possible, allowing the incoming light to arrive to the absorber layer. Very low sheet resistance values are needed, since the current flows in the horizontal plane of the solar cells. Regardless of the material to use, an important trade-off emerges. It is very important that the front contact has high bandgap energy, a high transmittance throughout the wavelength region of the absorber layer and high lateral conductivity in order to reduce resistive losses. In one hand, in terms of material properties, the conductivity mainly depends on the free

charge carrier density and the mobility, and absolute conductivity values depend on the thickness of the sample. Thick samples will have higher values of sheet conductivity compared with thin samples. In the other hand, these free charge carriers can absorb some of the energy in the near infrared, reducing the absorbing radiation of the absorber layer, therefore reducing the yield of the solar cell [29, 30].

This way, a thick front contact will have high conductivity and low resistive losses, but will absorb more of the incoming light. The critical competing parameters for the TCO layer are thus sheet resistivity and optical transmittance. A more thorough analysis is shown in chapter *4.2 ZnO:Al TCO*.

Typical contact layer materials are fluorine doped tin oxide, FTO, tin doped indium oxide, ITO, and doped zinc oxide, ZnO (Al, Ga, B). Even though ITO has been target of more studies [referência], aluminium doped zinc oxide, ZnO:Al or simply AZO, is the most used front contact material for CIGS. Depending on the dopping, the values of bandgap energy can increase up to 3.77 eV, and resistivity can go from 17 $\Omega.cm^{-1}$ down to 3 $\Omega.cm^{-1}$. A weight dopping of 1.5-2.5 % aluminium in the ZnO is shown to obtain the best properties for the solar cell [31-33]. Typical optical transmittances for small area solar cells (for research purposes) above 85 % are obtained, as well as sheet resistivities of 20-30 $\Omega.\square^{-1}$ [15], and therefore the common denomination of this layer as transparent conductive oxide, TCO.

The standard CIGS baseline from Uppsala deposits the ZnO:Al front contact after the i-ZnO layer in the same sputtering system, resulting in an ZnO:Al layer with thickness of 350 ± 20 nm and sheet resistivity of 30 $\Omega.\square^{-1}$ [2]. This is also the standard value that needs to be achieved if other deposition methods are used.

3.6 Grid

In laboratory research cells, the devices are measured with electrical probes, which reinforce the need to use metal grids on top of the TCO layer. A metal grid establishes this contact, while benefiting of a reduction in resistive losses in the cell, resulting in the possibility to thin down the TCO layer. The downside of the grid appliance is the shadowing of an area percentage of the solar cell, leading to a decrease in the incoming light into the cell, and therefore design specifications are required and have been developed both experimentally and by simulations [34-36].

Uppsala's baseline grid consists on a Ni-Al-Ni stack, where both layers of Ni prevent the aluminium to react with the air and to oxide. The second Ni layer further facilitates an Ohmic

contact between the grid and the measuring probe. For this work the grid was deposited to reach 3000 ± 500 nm by evaporation, with values of sheet resistance of 0.01-0.02 $\Omega.\square^{-1}$ [2].

4. BACKGROUND ZnO:Al TCO AND CdS BUFFER LAYER CONSIDERATIONS

All layers of the CIGS solar cells were carefully developed to reach the current record beyond 22 % efficiency [1, 2]. To reach such efficiencies many considerations and experimental results were taken into account for each layer of the CIGS. As the layers under investigation in this thesis are both ZnO:Al TCO and CdS buffer layer, an overall overview of their main desired characteristics for the CIGS solar cell will be approached and conducted throughout the experimental work.

4.1 CdS buffer layer

As previously mentioned in chapter *3.3 Buffer layer*, the standard CIGS solar cell benefits of an optimized layer that is capable of driving out the photo generated carriers with minimal absorption and recombination losses while coupling light to the junction. This is the role that the buffer layer plays.

The buffer layer should also modify the absorber surface chemistry by passivating surface states, granting protection to the CIGS solar cell from the subsequent window layer depositions and increasing the durability of the cell. It should also provide an alignment of the conduction band with the active CIGS, i.e. provide a pathway for a proper conduction of the electrons through the solar cell into the front contact, in order to yield better efficiency.

Among all possible buffer layers, CdS has shown to have the best properties acting as an n-type layer in the p-n hetero-junction of the CIGS, and is used in the recent CIGS solar cell performance record with 22.6 % efficiency [1].

CdS deposition can be performed by many possible methods, such as PVD, RF sputtering, ion-layer gas reaction and CBD [37-40]. The record solar cell uses CBD as deposition process for the CdS layer.

CdS by CBD is related to the minimization of the surface recombination, modifying native defects at the Cu-poor surface of CIGS by occupation of Cd atoms in the Cu sites [41-43]. On the other hand, CdS has low bandgap energy of approximately 2.4 eV, and so it prevents high energy photons from arriving to the CIGS layer; it contains Cd, which is a toxic element; lastly,

it is deposited with a non-vacuum method which interrupts all other vacuum-methods right in the middle of the fabrication of the solar cell.

The optimization of this layer compasses the thickness of the layer, and the deposition parameters. The latter are quite a few, for they also vary with the geometry of the deposition setup, and cover the concentrations of each deposition precursor and the temperature, pH, time and stirring of the deposition.

Concerning its thickness, CdS must be present with a minimal thickness in order to buffer the solar cell, by protecting the CIGS and by allowing a proper conduction of the electrons towards the collecting front contact. But, if it gets too thick, it will absorb even more high energy photons, and the electrons generated by this layer do not contribute to the output current [25]. Due to environmental reasons, too much Cd is to be avoided as well. Plus, an important consideration must be introduced: the depletion region factor.

Introduced in chapter *2.3 Doping semiconductors and the p-n junction*, the depletion region is the physical volume constituted of the ionized donors and acceptors on which the generated electric field spans. In this region, even though the charge particles are being drifted apart, their charges' sum should equal zero through the charge neutrality relationship described in equation 8:

$$p + N_D = n + N_A \qquad \text{Eq. 8}$$

, i.e. the number of holes, p, plus the number of ionized donors, N_D, equal the number of electrons, n, plus the number of ionized acceptors, N_A. Assuming that p and n can be neglected due to much larger values of N_D and N_A, this implies that the carrier concentration over the depletion area of each side of the hetero-junction must be equal, which means equation 9 takes form:

$$N_A w_P = N_D w_N \qquad \text{Eq. 9}$$

, where w_P and w_N are the depletion region width of the respective (p or n) side of the junction. So, for the same thickness of the absorber layer and thus for the same N_D and w_N, a thickening of the buffer layer will result on a decrease of its carrier concentration, leading to a lowered built in potential, V_{in}; as it increases with increasing depletion region width, and ultimately resulting in a decrease in the V_{OC} of the solar cell [44, 45].

This way, an optimized thickness for the CdS sample of 50-100 nm forecasts a better performance of the overall CIGS solar cell [46-48].

Finally, the deposition parameters must be evaluated. In terms of chemical precursors, the source of cadmium can affect the bandgap energy, the stress of the grown film and other

properties of the layer, and here cadmium acetate is a good source of Cd^{2+} ions [49]. The morphology and topology of the CdS are affected by the deposition temperature and pH as well. Most literature reports decide to calibrate the pH with values above 9, which seem to be acceptable values, even in the papers that do not intend to evaluate pH variations [50]. As for the temperature, recent papers show better results for temperatures of 80º C and 90º C [51], and yet Uppsala's baseline buffer layer is deposited with bath temperature of 60ºC, temperature that it constantly repeated throughout solar cells with the best performance. Note that the measurement of the temperature in this thesis is performed in the outer bath on which the deposition bath is immersed, and these temperatures can vary with the geometry of the setup and with the way the bath is heated.

Despite these discrepancies, 60º C was the temperature chosen for reference depositions, as the purpose of the work is to obtain a calibration of the thickness and the morphology of the layer with the variation of many parameters. The pH and amount of Cd and S of the CBD processes conducted throughout this thesis are strictly controlled through the concentrations of the ammonia and the Cd and S sources of the deposition, which were taken from the Uppsala's baseline CdS by CDB process, with values of 1.1 M (ammonia), 0.1 M (thiourea) and 0.003 M (cadmium acetate) [2].

4.2 ZnO:Al TCO

As mentioned before in chapter *3.5 Transparent conductive oxide*, the TCO plays a very important role in the CIGS solar cell. The choice of the material is very important, and some properties of the material are crucial for a better functioning of the solar cell.

In terms of intrinsic electrical properties, the conductivity of a material, σ (S.cm^{-1}), is determined by both the free carrier concentration, n_e (cm^{-3}), and by the carrier mobility, μ (cm^2.V^{-1}.s^{-1}), as given by equation 10:

$$\sigma = n_e e \mu \qquad \textit{Eq. 10}$$

, where e is the electric charge. The resistivity, ρ (Ω.cm), given by the inverse of the conductivity, an intrinsic property as well, along with the thickness of the sample, t, allows to calculate the sheet resistivity, R_s ($\Omega.\square^{-1}$), which is given by equation 11:

$$R_S = \frac{\rho}{t} \qquad \textit{Eq. 11}$$

The sheet resistivity is very important for solar cells, as the current flows in the horizontal plane.

These parameters, along with the transmittance of the material, are the electrical and optical properties of major importance for the TCO. Many other properties influence the performance of this layer, such as surface morphology, stability during processing and environmental stability. Other yet more specialized properties may also be relevant, among flexibility, hardness, work function, deposition parameters, choice of doping concentration and choice of thickness.

Considering all these factors, some trade-offs start to emerge. Higher doping concentration increases carrier concentration and hence conductivity, but also increases the optical absorption. Surpassing a certain doping level will reduce the carrier mobility and thus film conductivity may no longer increase. While the sheet resistivity can be easily decreased by thickening the film, this would imply an increase of the optical absorption of the film, leading to a reduction of the J_{sc} of the solar cell since less light arrives to the absorber layer. The optimal film thickness that minimizes the total power loss of a solar cell will then depend on the integrated optical absorption across the wavelength range of interest and the distance over which current has to travel in the TCO. Further theoretical developments can be found in *Handbook of photovoltaic science and engineering*, chapter *17 Transparent Conducting Oxides for Photovoltaics* [29].

ZnO:Al was the chosen material for the TCO layer of this thesis, as the objective is to reproduce the typical CIGS solar cell with ALD for the layer preparation. It stands the most promising material for TCO, and several deposition techniques have been studied, such as sputtering, chemical vapour deposition, pulsed laser ablation and atomic layer deposition [30, 52-54]. RF magnetron sputtering provides high quality ZnO:Al films, with resistivities as low as $1.4*10^{-4}$ Ω.cm at deposition temperature of 230ºC [55]. Even though atomic layer deposition presents typical values of 10^{-3} Ω.cm, it provides more accurate control on both thickness and doping, and such high temperatures are not required. Furthermore, it is much harder to reproduce the ZnO:Al properties found in the literature that are grown by sputtering. So, atomic layer deposition was chosen, and the next steps comprehend a background study on the deposition parameters, mainly the doping, deposition temperature and thickness of the TCO.

The aluminium doping is inserted in-between the ZnO, and its percentage is nicely controlled. Many studies suggest that the optimized Al doping stands between 1.5-2 % [30-32, 56, 57], which corresponds to Zn:Al deposition ratios between 20:1 and 15:1, respectively. This doping range optimizes carrier mobility and carrier concentration, and thus conductivity/resistivity, and surface roughness. Also, with increasing Al doping, the bandgap energy increases as well,

reducing the amount of energy absorbed by the layer, and so the main chosen Zn:Al deposition cycle ratio for this work is 20:1.

As for the deposition temperature, 150º C seems to be the most promising consideration, given that the CIGS absorber layer cannot withstand much higher temperatures for long periods of time without degrading.

Finally, the thickness range which gives rise to better results stand between 350-500 nm, usually closer to the latter [58]. Uppsala's baseline ZnO:Al layer presents an average thickness of 350 nm, due to considerable conductivity already achieved with no further thickening of the sample required.

Last note for the intrinsic ZnO layer, i-ZnO, deposited in-between the buffer layer and the TCO, which can easily be introduced by ALD just before the ZnO:Al layer, by simply eliminating the aluminium deposition cycles. Despite its acknowledgment as an improving factor, its role on the solar cell performance is not yet clear. It is generally thought that this 100 nm layer minimises the detrimental effect of short-circuit pathways and weak diodes, which may develop in the presence of pinholes in the CIGS or buffer layers, hence increasing the shunt resistance, FF and V_{oc} [59].

5. EXPERIMENTAL TECHNIQUES

The improvement of the CdS and ZnO:Al layers naturally embraces two steps: deposition and characterization. The deposition of CdS was performed with chemical bath deposition, CBD, and the ZnO:Al samples were grown with atomic layer deposition, ALD. The characterization techniques aim to characterize several distinct parameters of the layers grown, such as optical, electrical, structural, topological, and composition parameters.

This chapter's purpose is to explain the *modus operandi* of deposition and characterization techniques. The deposition techniques' ground configurations are explained along this chapter, while the characterization technique's ground configurations are presented over the *Results and Discussion* chapter.

5.1 Chemical bath deposition

Chemical bath deposition of thin films occurs from aqueous solutions at low temperatures by chemical reactions between dissolved precursors, supported by a complexing agent. It has been extensively used for II-VI semiconductor growth purposes [60-65], particularly for CdS growth purposes as a buffer layer for CIGS solar cells [66-70].

This deposition process uses a controlled chemical reaction to deposit material onto a substrate by precipitation. Typically, a substrate is immersed in an alkaline solution with a chalcogenide source, a metal ion and an added base. The bath must be supersaturated in order to obtain the deposition of solid material, which means the bath must be thermodynamically unstable with respect to precipitation of the solid phase formed [71].

There are two possible parent reactions leading to solid material: homogeneous and heterogeneous precipitations. The first occurs within the bulk of the solution, whilst the later occurs at the surface of the sample. Still, when it comes to the growth of thin films, the literature tends to discuss the deposition of thin films in terms of two mechanisms. The following discussion follows reference [72].

The first one is ion-by-ion deposition, which is characterized by the condensation of the ions at the reacting surface of the sample to form the film. The second one is called cluster-by-cluster deposition, or colloidal deposition, in which agglomerates of colloidal particles, pre-formed in the solution by the homogeneous reaction, are adsorbed at the surface of the sample to particulate films. These colloids grow in size over time and form the particulate part of the film.

Figure 8 schematically represents these processes.
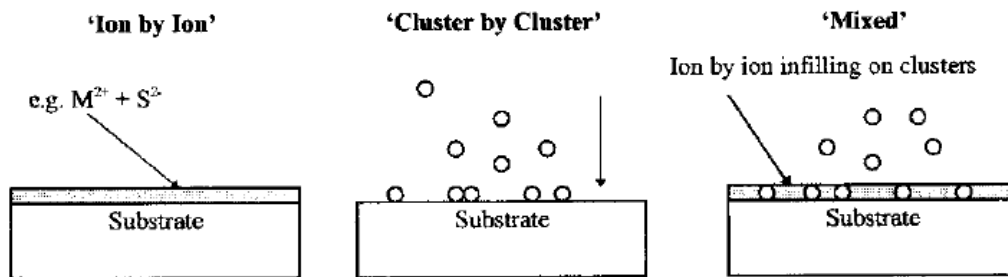
Figure 8 – Schematic representation of the processes which could lead to the deposition of a thin film. [71].

In practice, both processes coexist, leading to films in which colloidal material is included in the growing film by a mixed deposition of these two mechanisms. The predominance of one mechanism over another is governed by the extent of homogeneous or heterogeneous nucleation.

The deposition medium of generalized "AB" thin films consists of one or more salts of a group II metal ion A^{2+} (Cd^{2+}, Zn^{2+}), a source for the chalcogen B^{2-} (S^{2-}, O^{2-}) and usually a complexing agent, in an aqueous solution. Acetates, sulfates and nitrates are good metal precursors, since they have moderate to high solubility in water. Chalcogen sources typically include thiourea (thiocarbamide) or thiosulfate for S^{2-} ions, while the dissociation of water itself provides oxygen in the form of ions OH^-. The complexing agent, such as ammonia or ethanolamine, provide ligands for the reactions.

Four fundamental steps are believed to ground the CBD process [71]:

1. Complexing agent – water equilibrium.
2. Formation/dissociation of ionic metal-ligand complexes.
3. Hydrolysis of the chalcogen.
4. Formation of the solid.

Most of the control of the CBD process lays on the adjustment of the last three steps. Basically, it all sums up to whether the solid forms as a film or as dispersed particles in the liquid, i.e. whether the dominant deposition proceeds by ion-by-ion growth on the substrate (heterogeneous deposition) or by adsorption of the colloids formed in the solution (homogeneous deposition).

The control of these steps determines the composition, growth rate, microstructure and topography of the resulting film [71].

The main advantages of the CBD technique are the following:

- Starting chemicals are commonly available and inexpensive.
- Preparation parameters are easily controllable to improve the topology of the film.
- Is suitable for coating surfaces of any morphology and geometry, given that the surface is insoluble.
- Low temperature process avoids oxidation and corrosion of metallic substrates, as well as the merging of material inside the substrate.
- A large number of substrates can be coated in a single run.

These characteristics altogether turn the CBD process into a very simple, low temperature and inexpensive large-area deposition technique.

In the context of this work, the major drawback is the fact that CBD is the only wet process which pauses the vacuum processes of the growth of CIGS solar cells.

5.1.1 CdS growth by chemical bath deposition

The chemical reactions that occur for the CdS deposition to take place are stated from equation 12 to 14:

$$(NH_2)_2 CS + 2OH^- \rightarrow S^{2-} + CN_2H_2 + 2H_2O \qquad \text{\textit{Eq. 12}}$$

$$Cd(NH_3)_4^{2+} \rightarrow Cd^{2+} + 4NH_3 \qquad \text{\textit{Eq. 13}}$$

$$Cd^{2+} + S^{2-} \rightarrow CdS \qquad \text{\textit{Eq. 14}}$$
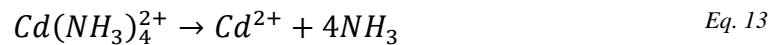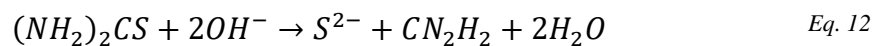
The hydrolysis of thiourea releases sulphide ions. In the meantime, Cd^{2+} ions form tetraaminecadmium (II) complex ions by combining with the ammonia. These $Cd(NH_3)^{2+}_4$ complexes adsorb on the glass, and the heterogeneous nucleation and growth takes place by ionic exchange reaction with S^{2-} ions. The proper control of these processes lead to the most-suited CdS films for CIGS solar cells [73].

Several parameter considerations were previously presented in chapter *4.1 CdS buffer layer*, and will be later outlined in *Results and Discussion* chapter. Nevertheless, some ground preparation specifications will now be given.

Molybdenum samples 5x5 cm were cut into four, in order to grow the CdS samples onto 2.5x2.5 cm Mo samples. Mo substrates were used instead of glass substrates to ease the contact profilometry and GIXRD measurements, as the deposited and non-deposited areas of CdS contrast a lot more on the Mo substrates. The samples were previously cleaned with acetone, isopropanol and deionized water, followed by N_2 pressurized gas for drying purposes.

Cadmium acetate (Alfa Aesar, 99.999 %), thiourea (Alfa Aesar, 99 %) and ammonia (Sigma-Aldrich, 28.0-30.0 %) were used as Cd source salt, chalcogen and complexing agent, respectively.

The bath's solution for this thesis is composed of 1.2 M ammonia, 0.13 M thiourea and 0.004 M cadmium acetate.

An outer water bath is previously heated to the desired temperature, while all the solutions are prepared in order to proceed with the deposition. Cadmium acetate and thiourea quantities were measured in a normal scale, 0.005 g of error. The powder quantity measurements proved to be a considerable challenge due to the mass fluctuations observed in the scale. An ultrasound system (Fisher Scientific) is used to help dissolving the thiourea in deionized water.

The samples were placed in a Teflon substrate holder, specifically designed and built for this work, concerning the whole geometry of the deposition system.

Figure 9 shows the system in which the depositions took place.
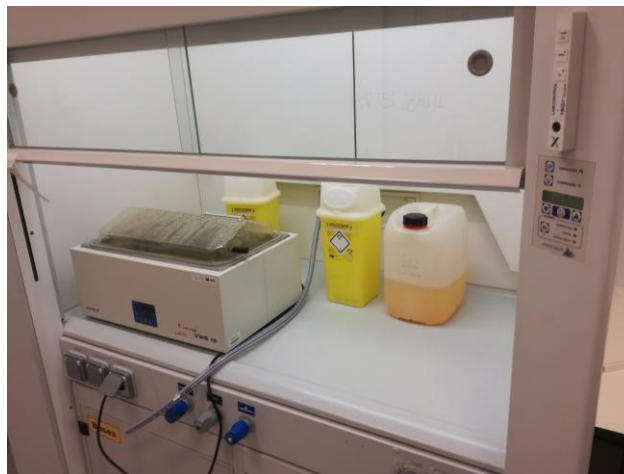
Figure 9 – Equipment used for CBD depositions.

After deposition, the samples were submersed in deionized water, to eliminate possible chemical reactions still under process, and a N_2 pressurized pump was used to dry the samples. Annexes *I* and *II* show the design of the sample holder that was developed and tested during this thesis and the developed protocol to ease further CdS depositions.

5.2 Atomic layer deposition

ALD is a vapour phase deposition technique, popularly introduced as atomic layer epitaxy (ALE) in the 70s, when ZnS was deposited for flat panel displays [74, 75]. Metals and metal oxides were further introduced in this process, and the ALD name was adopted since many of these materials were deposited non-epitaxially. Initially, the characteristic low growth rate was

clearly a limiting factor for its applications, but further size reduction of semiconductor devices' fabrication and interest in dielectric oxides renewed an increasing interest in the technique. Nowadays it is considered to be one of the most promising thin film and nanostructure fabrication methods.

In a typical chemical vapour deposition (CVD) process, all reactants are introduced at the same time into the deposition chamber to react altogether. The ALD is based on sequential self-limiting reactions, featuring an alternation of the pulse of the precursor gases and vapours onto the substrate surface at considerable lower temperatures. The interaction of the molecules with the substrate leads to the deposited film, and can be divided in two general classes: chemisorption and physisorption [76].

In chemisorption, the electronic structure of the precursor molecules changes when new covalent/ionic bonds are formed between the precursor molecules/elements and the molecules/elements at the substrate. The places in the surface where this chemical bond can occur are called reaction sites, and they limit the number of absorbed molecules so that only a monolayer of the precursor species is adsorbed. Given so, the amount of atoms each precursor pulse adds to a surface, considering an ideal ALD precursor pulse, is decided by both number of reactive surface sites, which depend on the substrate, and the steric hindrance, which depends on the size of the precursor molecules.

Physisorption is a form of interaction as chemisorption, but rather weaker, caused by Van der Waals forces that occur between a molecule and a surface. The precursor usually undergoes minimal changes in this process, and, as this interaction is not specific to a certain reaction site, can lead to the physisorption of multilayers.

The adsorption of molecules to a surface can be irreversible or not, depending on the temperature of the process. To grow a self-terminating ALD process, an irreversible adsorption is necessary.

A general ALD process is illustrated in figure 10.

27
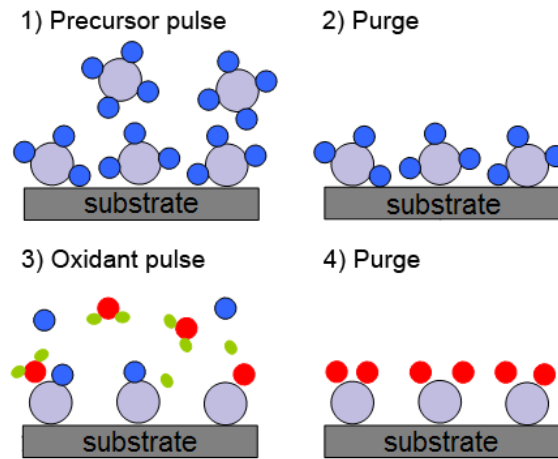
Figure 10 – One ALD cycle process, description below [77].

Firstly, a precursor flows through the chamber and reacts with the surface of the substrate. This is a self-limiting process of which results one chemisorbed monolayer of the precursor at the surface, plus some extra precursor that did not react (1). Then, a purging gas passes through the chamber to remove the excess precursor, leaving but a monolayer of the first precursor (2). Follows a second precursor gas, pulsed into the chamber, that reacts with the first precursor's monolayer, leaving one monolayer of the desired material plus some reaction by-products (3), which will be removed with a second purging gas flow inside the chamber (4). The final result is one monolayer of the desired material deposited on the substrate surface [74].

The flow time of each precursor through the chamber is critical up to the limit that guarantees a full reaction between the precursor and the sample. The purging time is critical as well to assure that all excessive material is purged away from the sample. Typical purging gases used are N_2 and Ar. In an ideal ALD process, the surface is exposed to each precursor long enough for the surface to become saturated by precursor absorbents.

The primary advantages and disadvantages of the ALD process are all derived from its characteristic sequential self-saturating gas-surface reaction control of the deposition process [74, 76]:

- **Thickness precisely controlled by the number of cycles of deposition.**

  A wide variety of materials can be deposited with this technique, each one with a summarized growth per cycle in previous reviews [78, 79]. Different research groups usually get different cycle ratios for the same material, depending on the geometry of the equipment and the pulse time of each precursor and purging gas. Still, as this process is self-restricted to layer-by-layer growth, the thickness will certainly be linearly influenced by the number of cycles during the deposition.

28

- **Composition control.**

  Multiple ALD cycles can lead to an ALD "supercycle", constructed with a ratio of cycles of two components, such as the ZnO:Al TCO layer developed in this thesis. Composition control has been demonstrated with materials such as ZTO and $SrTiO_3$ [80, 81]. ALD is vastly used to deposit binary, ternary and quaternary materials, although some complications might occur with each extra component.

- **Good reproducibility and straightforward scale-up.**

  Due to its linear dependence of number of cycles with thickness, scale-up is straightforward. Reproducibility is favourable as there are few parameters to adjust. The chosen precursors and both precursors and purging gases flow time through the chamber can be raised to assure the monolayer deposition and the leftovers cleaning, granting a good reproducibility apart from the equipment's geometry.

- **Uniform and homogeneous films with conformity of high aspect ratio and three dimensionally-structured materials.**

  With sufficient precursor pulse times, the precursor can disperse into deep trenches, allowing for complete reaction with the entire surface. By restricting the reaction at the surface to no more than one layer of precursor at a time, the process allows the subsequent cycles to lead to a uniform growth on high aspect ratio structures, whereas typical CVD and physical vapour deposition (PVD) processes may suffer from non-uniformity due to faster surface reactions and shadowing effects, respectively. Pinhole-free layers are the outcomes.

- **Low deposition rates.**

  Due to the long cycle times involved in pulsing and purging and the layer-by-layer nature of the technique, this is a major drawback for deposition of thick samples [82].

- **Waste of material.**

  The precursor gases fill the whole deposition chamber, yet only one layer is deposited onto the substrate at a time, which makes but a small fraction of the whole surface that the precursor will cover.

The deposition rates are strongly dependent on the reactor design and on the aspect ratio of the substrate. As the surface area and volume of the reactor decrease, so does the time needed for

pulsing and purging. High aspect ratio substrates require longer pulse and purge times to allow the precursor to disperse into the (possible existent) three dimensional features of the substrate. Nevertheless, as the technique is scalable up to very large substrates, it has caught a great deal of attention in the industry. It is a very promising method to deposit TCO films for advanced solar cells and organic light-emitting diodes which require 3D structures or low deposition temperatures.

5.2.1   ZnO:Al growth by atomic layer deposition

The main chemical reactions involved in both ZnO and Al_2O_3 depositions by ALD are described in the following equations 15 and 16:

$$Zn(C_2H_5)_2(g) + H_2O(g) \rightarrow ZnO(s) + 2C_2H_6(g) \qquad \text{Eq. 15}$$

$$2Al(CH_3)_3(g) + 3H_2O(g) \rightarrow Al_2O_3(s) + 6CH_4(g) \qquad \text{Eq. 16}$$
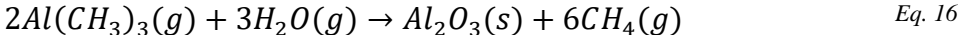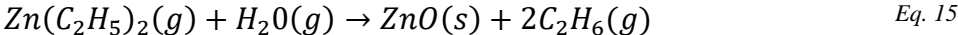
All the ground configurations for this technique must assure that these equations take part as flawless as possible.

ZnO:Al samples were grown by ALD onto 76x26 mm glass samples at 150º C. The samples were previously cleaned with acetone, isopropanol and deionized water, followed by N_2 pressurized gas for drying purposes. Diethyl-Zinc (DEZ) and trimethyl-aluminium (TMA) were used as precursors for the ZnO and Al_2O_3 layers deposition, along with H_2O for both layers. The purging gas used was nitrogen, N_2. The sequence of deposition for each layer is schematized in figure 11, along with the respective pulse times for each material.
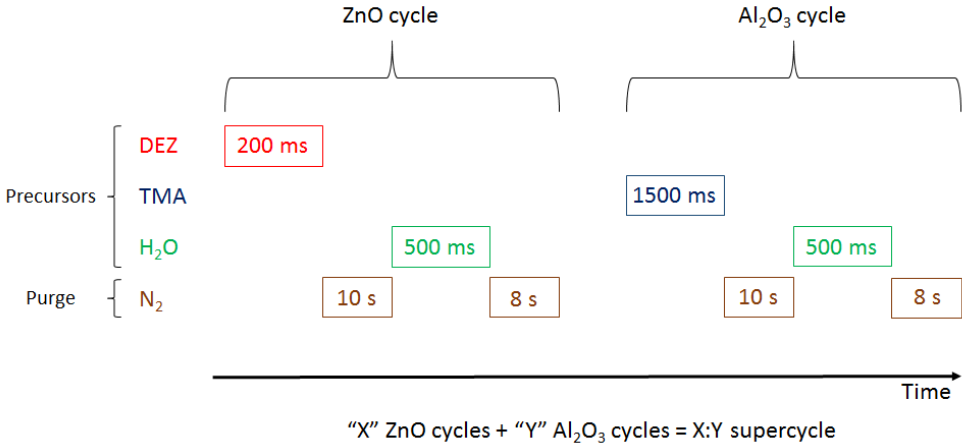
Figure 11 – Precursors' and purging gases' timeline for the ALD process.

Each of the precursor pulses is followed by a purging gas pulse. DEZ pulse lasted 200 ms, TMA took 500 ms, H_2O pulses for 500 ms and the purging gases were introduced for 8-10 s every

time. A supercycle of 20:1, for example, stands for 20 cycles of ZnO plus 1 cycle of Al_2O_3, as depicted above.

There is a very significant discrepancy among the literature concerning the pulsed times of the purging gases, varying from 500 ms up to 20 s [31, 57, 83-86]. 8 and 10 seconds were chosen to assure enough purging times to cleanse the whole surface.

This way, a deposition of 160 supercycles 20:1, as an example, will take approximately 17 hours and 30 minutes, which is a considerable time given that the whole deposition process is performed under 150º C.

While all the parameters were chosen to optimize the characteristics of the ZnO:Al layer, the deposition system is designed to perform ALD in 200 mm diameter inch silicon wafers.

Figure 12 shows the used equipment, Beneq TFS 200.

Figure 12 – Beneq TFS 200 ALD equipment [87].

5.3 Atomic force microscopy

AFM is a powerful and versatile characterization technique. It can provide various sorts of surface measurements, as well as imaging of three-dimensional topography, with atomic resolution up to the angstrom scale resolution.

A sharp probe is brought into close proximity with the sample, and then it moves relative to the sample in a raster pattern. AFM measures the height of the surface by "touching" it with the sharp probe, while measuring the vertical displacements. The sharp tip is attached to a flexible cantilever which bends under the influence of force. The bending produces a change in the inclination angle of the cantilever, measured by a bouncing laser beam off to the cantilever and into a position-sensitive detector. This detector gauges small movements of the laser spot. The

vertical tip movement is then quantified from this cantilever bending [88]. This apparatus is depicted in figure 13.
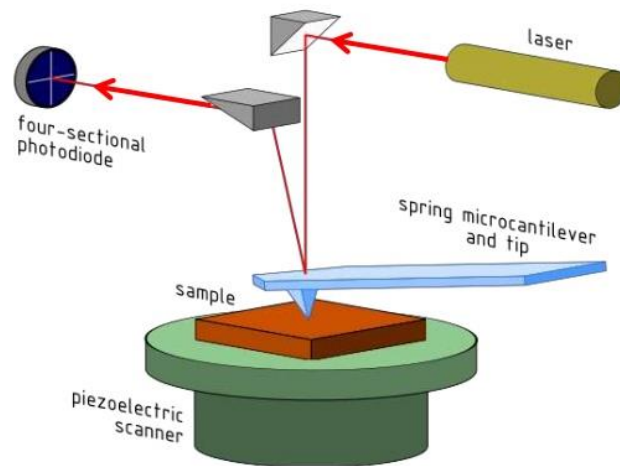
Figure 13 – Schematized AFM apparatus [89].

There are two kinds of basic AFM modes: contact mode and tapping mode. With the contact mode, the tip scans the sample in close contact with the surface of the sample, which can cause problems with excessive tracking forces applied by the probe to the sample. If the sample is rough, at the highest deviations of force atop hills, the tip or sample might mechanically abrade; conversely, in the deepest valleys, the tip and sample might separate or disengage.

For this work, the tapping mode was used. Tapping mode overcomes problems associated with friction, adhesion and other difficulties of the contact mode by alternately placing the tip in contact with the surface to provide high resolution and then lifting the tip off the surface to avoid dragging the tip across the surface. Tapping mode imaging is implemented in ambient air by oscillating the cantilever assembly at or near the cantilever's resonant frequency using a piezoelectric crystal. The piezo motion causes the cantilever to oscillate with a high amplitude (typically greater than 20 nm) when the tip is not in contact with the surface. As the oscillating cantilever begins to intermittently contact the surface, the cantilever oscillation is necessarily reduced due to energy loss caused by the tip contacting the surface. The reduction in oscillation amplitude is used to identify and measure surface features [88].

Figure 14 depicts the AFM equipment used for this work, Bruker-Dimension Icon.

Figure 14 – AFM equipment, Bruker-Dimension Icon.

It is important to note that, even though the measurements were performed by someone else, the interpretation of the AFM results were personally performed.

5.4 Scanning electron microscopy

SEM is a microscopy technique that produces images of the samples through the scanning of its surface with a focused high-energy electron beam. SEM uses accelerated electrons as a source of illumination, and, as the electrons' wavelength can be up to 100 000 times smaller than visible light photons, it generates images with high resolution and can reveal the structure of smaller domains.

The main SEM systems contains several components, and is schematized in figure 15.
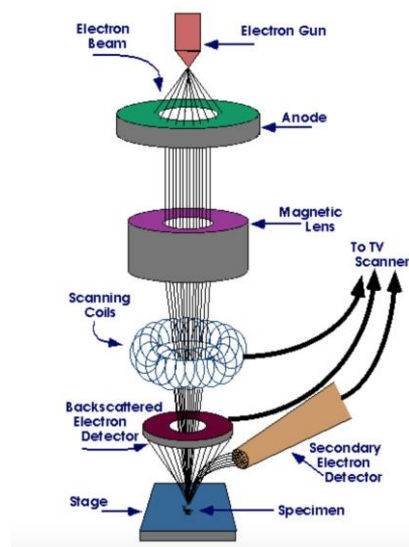
Figure 15 – Main SEM system schematization [90].

The source of electrons, a solid state crystal or a field emission gun, emits electrons into a column. This column is composed of a series of optic elements, such as magnetic lenses, scanning coils and objective lenses, and is responsible for the focusing and redirecting of the electrons through the column into the stage, where the sample is inserted [91, 92].

When the electrons hit the surface, they penetrate onto the surface up to a few microns, depending on the accelerating voltage and the density of the sample, resulting on the emission of several signals, according to the type of interaction, such as: characteristic X-rays, secondary electrons and backscattered electrons. Characteristic X-rays occur when outer-shell electrons fill vacancies in the inner-shell of the sample's atom, releasing X-rays. Secondary electrons are low-energy electrons produced when the electrons are ejected from the k-orbitals of the sample atoms by the imaging beam, while backscattered electrons are higher energy electrons that are elastically backscattered by the atoms of the sample. These signals will be collected by respective detectors, and the most common type of imaging uses the secondary electrons for that purpose [91, 92].

The volume of interaction SEM-sample depends on a significant amount of parameters, such as acceleration voltage applied, the material constitution and density [92]. Figure 16 depicts SEM's volume of interaction and the various signals that it generates within a sample.
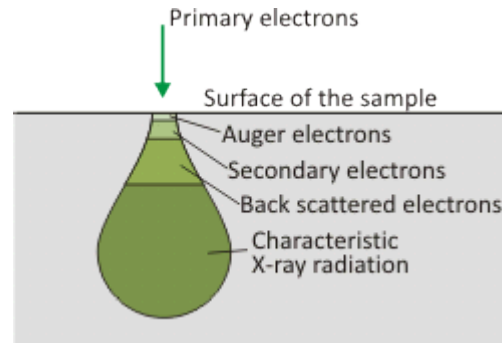
Figure 16 – Shape of electron interaction volume and signals generated within a sample [93].

The maximum resolution obtained from a SEM depends on several factors, such as the electron interaction volume of the electron beam with the sample. Even though it cannot achieve atomic resolution, typical modern full-sized SEM systems provide resolutions between 10-50 nm (for specific samples with strict conditions).

Figure 17 depicts the SEM equipment used for this work, Quanta FEG 650.

Figure 17 – SEM equipment Quanta FEG 650.

5.5 X-ray diffraction

XRD is a characterization technique which collects information on the crystalline structure of a material. X-rays are characterized as a short-wavelength high-energy form of electromagnetic radiation, with wavelength between 0.01 nm and 1 nm, and typical photon energies ranging from 100 eV to 100 keV. With wavelength comparable to the size of atoms, X-rays easily penetrate most materials, offering a unique possibility to investigate structural arrangements of atoms and molecules in a wide range of compounds.

A focused monochromatic beam hits a crystalline structure, and the interaction between the radiation and the array of atoms in the material gives rise to a diffraction pattern. X-rays are scattered by the electrons of the atoms without changing their wavelength. The electrons absorb the incident X-rays, by exciting themselves to higher unstable energy levels, and then emit the radiation by relaxation, releasing energy of the same frequency and wavelength as the absorbed. If the wavelength of these scattered X-rays remains the same, the photons did not lose any energy, they only changed their momentum. This process of energy conservation and momentum transfer is called elastic scattering, or Thompson Scattering.

As X-rays penetrate and interact with the compound's atoms, if they are regularly arrayed, they will produce a regular array of diffractions, and, even though the intensity of the diffracted X-rays cancels out in most directions through destructive interference, it will add constructively in a few specific directions. For a given set of lattice planes, the condition for a diffraction to occur can be given by Bragg's law, defined by equation 17:

$$2d\sin\theta = n\lambda \qquad\qquad Eq.\ 17$$

, where d is the spacing between diffracting planes (and therefore the interplanar distance of the material), θ is the incident angle, n represents an integer of the order of the diffraction peak and λ the wavelength of the incident beam. By collecting information on the angles and intensities of these diffracted X-rays, a diffractogram is built, matching the intensity of the received signal from the detector with the angle of diffraction with which the detector received the signal.

Inelastic scattering, or Compton Scattering, also occurs, when X-rays transfer some of their energy to the electrons and the scattered X-rays have a different wavelength than the incident radiation. These inelastic scattering resulting X-rays will contribute a slowly varying background radiation to the experiment [94].

As each material has its own crystalline structure, each one possesses a specific signature diffracted pattern. By comparison with the literature peaks and intensities accepted by the scientific community, these diffractograms provide information such as the present crystalline phases and the atomic orientation of the plans, and allow us to calculate approximate values of the lattice parameters and crystallites' size. It may also allow us to infer some information on the existence of possible residual tensions of traction or compression, according either to the deviation of the peaks from their correspondents in the literature or to the deviation of the structure parameter values.

Figure 18 depicts the XRD equipment used for this work, X'Pert PRO PANalytical.

Figure 18 – X'Pert PRO PANalytical XRD equipment.

It is important to note that a training to correctly use the equipment was personally received, and all measurements were personally performed.

5.6 Optical spectroscopy

When a beam of light hits a solid, several events take place. The beam may be reflected, transmitted, diffused, absorbed, refracted or polarized, and each event has its own likelihood of taking place, depending on the properties of the material and the incident beam's angle of incidence.

Figure 19 schematizes the interaction between a beam of light and a solid, and all possible physical phenomena that may occur.
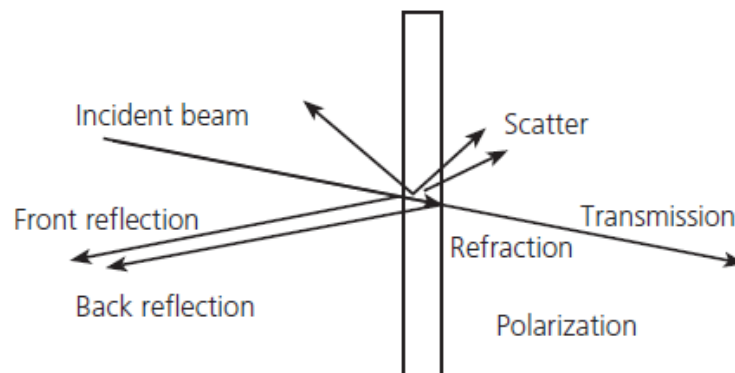
Figure 19 – Light-solid interaction phenomena [95].

Optical spectroscopy consists on emitting a beam of light with ultra-violet, visible or infra-red wavelengths onto a material and measuring the quantity of light that is transmitted, reflected or absorbed for each wavelength, always taking into account of every possible outcome of events (diffusion, refraction and polarization) [95]. The spectral range covered by this technique varies with the equipment, ranging from 150 nm up to 5000 nm.

5.6.1 Transmittance measurements

There are two kinds of transmittance to take into account. Direct transmittance is the part of the incident beam that is transmitted at the same angle as the angle of incidence and diffuse transmittance is the part of the incident beam transmitted in all directions. There are several possible reasons to deviate the incident beam, such as refraction, uneven surface of the sample, convex/concave surfaces, etc. To measure the overall transmittance, an integrating sphere modulus is needed [95].

A double beam of radiation (with the wanted wavelength) is projected towards two targets: the sample to measure on, and a reference sample, the substrate. The substrates' measurements will calibrate de equipment, and thus the retrieved measurements belong to the film alone.

Figure 20 schematically illustrates the optical path inside the spectrometer.
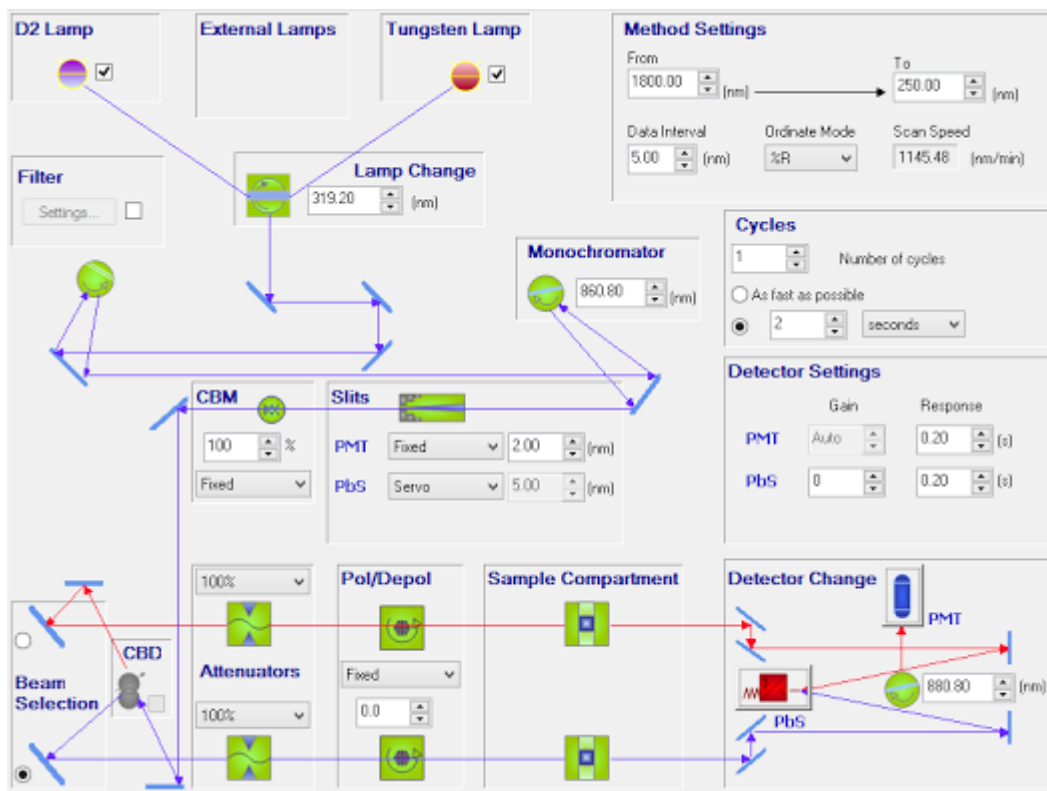
Figure 20 – Schematic illustration of the optical path inside the spectrometer.

The spectrometer is equipped with two sources of radiation and two detectors. A deuterium and a tungsten lamps provide the light generation, and a PbS and a PMT detectors receive the incoming radiation. By adjusting both the sources and the detectors, the spectrometer has an optimized response for the measurements.

Figure 21 depicts the equipment used for transmittance measurements, PerkinElmer UV/VIS/NIR Spectrometer Lambda 950. A 2D Detector Module was used. All measurements were personally performed.
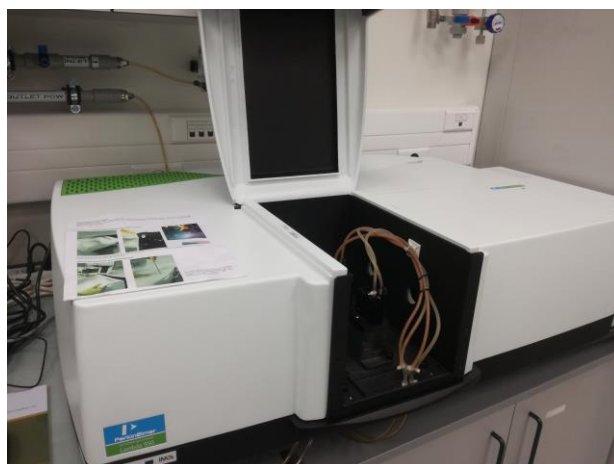
Figure 21 – PerkinElmer UV/VIS/NIR Spectrometer Lambra 950.

5.6.2   Swanepoel method

The Swanepoel method is a powerful theoretical fitting procedure to calculate the thickness of a film, t, given a transmittance spectrum of a film, T_R, with a claimed accuracy of better than 1 % and similar accuracies in the values of the refractive index, n. It is a simple and fast procedure with general mathematic equations and also with approximations for several transparency regions, taking into account approximations on both values of the absorption coefficient, α, and absorbance, x, which is given by equation 19:

$$x = e^{-\alpha t}$$

<div align="right">Eq. 19</div>

It is important to notice that this method only works if the transmittance spectrum contains interference fringes, which appear if the film thickness is of the same order of magnitude that the wavelength of incident light. These fringes are the result of constructive and destructive interference, and will give values of maximum local transmittance, T_M, and minimum local transmittance, T_m.

Figure 22 depicts the transmittance spectrum of the sample AZO160, as an example.
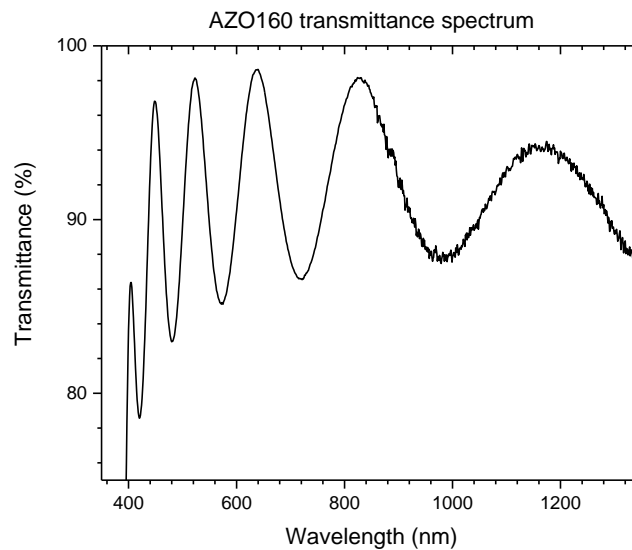
Figure 22 – Transmittance spectrum, $T_R(\lambda)$, of the sample AZO160.

This thesis only encloses the transparent region, and the full development of the methodology is found on reference [96].

In the transparent region, the values of the absorption coefficient, α, and absorbance, x, are approximated to 0 and 1 respectively. For this region, the parameters needed to apply this method are the transmittance of the substrate, $T_s(\lambda)$, which is fairly constant throughout all the

wavelength values, and the minimum transmittance values from the fringes, $T_m(\lambda)$, results of the destructive interference, which is a function of the incident wavelength.

Given these values, the refractive index of the substrate, s, is given by equation 20:

$$s = \frac{1}{T_s} + \sqrt{\frac{1}{T_s^2} - 1}$$

Eq. 20

The next step is to calculate the auxiliary function $M(\lambda)$, through equation 21:

$$M(\lambda) = \frac{2s}{T_m(\lambda)} - \frac{s^2 + 1}{2}$$

Eq. 21

Function $M(\lambda)$ has no physical interpretation, and is merely a helpful parameter to ease calculations. Now, we can calculate the refractive index of the sample, $n(\lambda)$, with equation 22:

$$n(\lambda) = \left[M(\lambda) + \{M(\lambda)^2 - s^2\}^{1/2} \right]^{1/2}$$

Eq. 22

Finally, the thickness t can be calculated using the diffraction indexes for two consecutive minima and their respective wavelengths, as equation 23 allows:

$$t = \frac{\lambda_1 \lambda_2}{2(\lambda_1 n_2 - \lambda_2 n_1)}$$

Eq. 23

5.7 Contact profilometry

A profilometer is an instrument used to measure a surface's profile, quantifying the roughness in a surface and height differences between small scaled structures. All measurements taken for this thesis were personally conducted with a contact profilometer, though both contact and optical profilometers are common.

In a contact profilometer, a stylus is used as a probe, which physically moves vertically in contact with the sample and scans horizontally along the surface of the sample for specified distances and contact forces, in order to acquire information on the surface's differences in height. A feedback system keeps the arm with a specific torque on it, and the changes in the z position of the arm holder can then be used to reconstruct the surface: an analog signal is generated with the variation of the height of the stylus, as it moves vertically; this analog signal is then converted into a digital signal, analysed and displayed.

As this technique requires force feedback and physically touching the surface, it is extremely sensitive and therefore provides high z resolution, even though it is more sensitive to soft

surfaces and the probe can become contaminated by the surface. The gain is also balanced with slower measurements when compared with optical profilometry. It can be used to measure thin film thickness providing that there is a trench in the film that covers it whole depth [97, 98]. During the course of this work, the realization of the trenches has been the biggest source of error for contact profilometry measurements.

Figure 23 shows the contact profilometer used throughout this work, *KLA Tencor Profiler P-16*, which is placed inside INL's cleanroom.
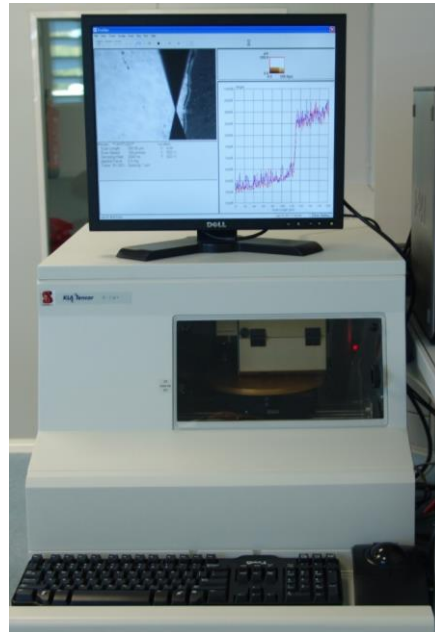
Figure 23 – KLA Tencor Profiler P-16 contact profilometry equipment.

5.8   Four-point probe

Four-point probe is a technique that measures the resistivity of a sample. It consists on separate pairs of current-carrying and voltage-sensing electrodes, and the separation of these electrodes eliminate the lead resistance and contact resistance from the measurement, obtaining more accurate data than the more common two terminal sensing, especially for low resistance values. Figure 24 shows the four-point probe system. Both the outer current-carrying and the inner voltage-sensing electrode pairs touch the surface, equally spaced among them, to obtain the sheet resistivity measurements.
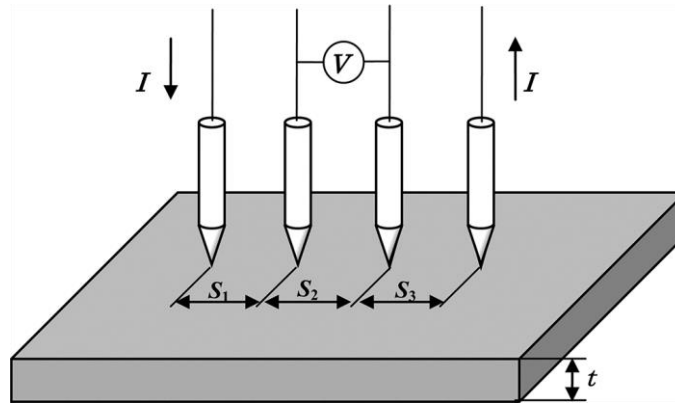
Figure 24 – Four-point probe apparatus [99].

The equipment, CMT-SR2000NW, lies within the cleanroom, and figure 25 depicts the same.
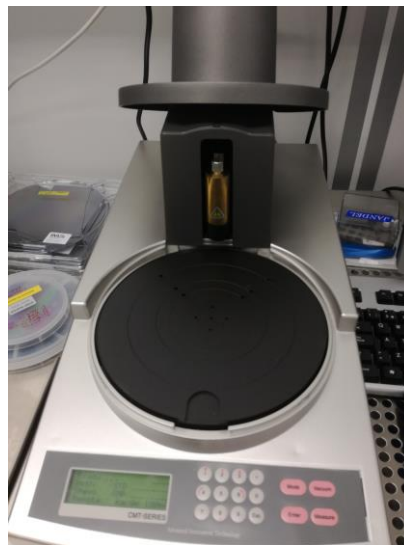
Figure 25 – Four-point probe equipment.

5.8.1 Methodology

As mentioned in a 1957 paper published by F. M. Smits [100], a current source in an infinite sheet gives rise to a logarithmic potential according to equation 24:

$$\varphi - \varphi_0 = -\frac{I\rho_s}{2\pi}\ln r$$

Eq. 24

, where φ is the potential, I is the current, ρ_s represents the sheet resistivity, and r stands for the distance from the current source.

For a dipole in particular, the potential is given by equation 26:

$$\varphi - \varphi_0 = \frac{I\rho_s}{2\pi}\ln\frac{r_1}{r_2}$$

Eq. 26

In the four-point probe on a sheet, the outer points become the dipole, thus the potential difference between the two inner points, for an infinite sheet, is represented by equation 27:

$$\Delta\varphi = V = \frac{I\rho_s}{\pi}\ln 2 \qquad\qquad \textit{Eq. 27}$$

, where only equal point spacing is considered. This way, sheet resistivity values are obtained from equation 28, considering that the distance between the electrodes is much smaller than the sample size:

$$\rho_s = \frac{V}{I}\frac{\pi}{\ln 2} = \frac{V}{I}4.5324 \qquad\qquad \textit{Eq. 28}$$

RESULTS AND DISCUSSION

6. CDS RESULTS

To study and calibrate the CdS films growth and in order to achieve thicknesses around 50-70 nm as for the common and optimized buffer layers for CIGS solar cells, several experiments were performed. These experiments were carefully designed to allow the determination of which parameters are the most sensitive and each ones should be finely tuned, in order to obtain CdS films with the desired thickness and also with a small amount of segregates.

Firstly, an evolution of the bath temperature experiment was run. The outer bath is kept at constant temperature, but the deposition bath gradually increases its temperature when it enters the outer bath, up to a certain temperature. This experiment consists on running a deposition with no samples to deposit on, measuring the temperature every minute after the manual stirring, and on taking photographs to check on the colour of the bath over time as well.

Secondly, several series of grown samples were performed. The main objective is to obtain a relationship between the resulting (measured) thicknesses and several parameters, such as the time of deposition, the amount of ammonia, the bath temperature and the amount of cadmium acetate, to test the reproducibility of the depositions and to calibrate the deposition technique to achieve the desired sample thicknesses of 50-70 nm. Pictures of the grown samples will be shown to demonstrate that a relation between the colour of the samples and their thicknesses can be established. The establishment of such procedure allows for a much quicker feedback, since it avoids the use of the complicated thickness profilometry measurements.

The characterization of the CdS thin films was performed with techniques such as contact profilometry, to measure the samples' thickness, and XRD to check on the structural properties of the deposited films. Further analysis was performed with a simple colour-thickness relation and optical microscopy. The first allows a rapid thickness estimation of the samples with simple naked-eye observations. The latter was performed to run a statistical particle analysis on average particle area percentage and area size in order to infer on the dominant deposition process, previously described in chapter *4.1 Chemical bath deposition*.

6.1 Evolution of the bath temperature experiment

The parameters used for this experiment were: 11 minutes "deposition", 60º C outer bath temperature, 15 ml ammonia, 130 ml deposition bath liquid, 0.13 g cadmium acetate and 1.33 g thiourea.

Table 1 shows the temperature evolution of the deposition bath with time.

Table 1 – Temperature evolution of the deposition bath overtime. Colour pattern for timeline assessment easiness.

t (min)	0	1	2	3	4	5
T (ºC)	25	30	34	38	44	48
t (min)	6	7	8	9	10	11
T (ºC)	52	53	54	55	55	55

Figure 26 graphically represents the deposition bath temperature evolution overtime.
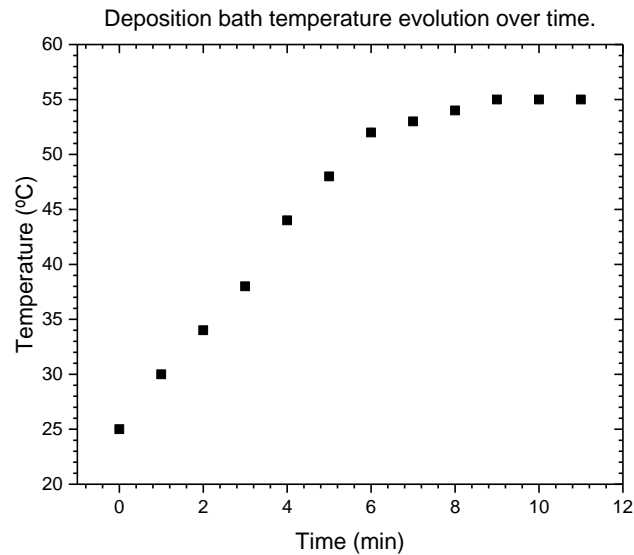
Figure 26 – Deposition bath temperature evolution overtime.

Figure 27 shows the deposition bath colour evolution over time.
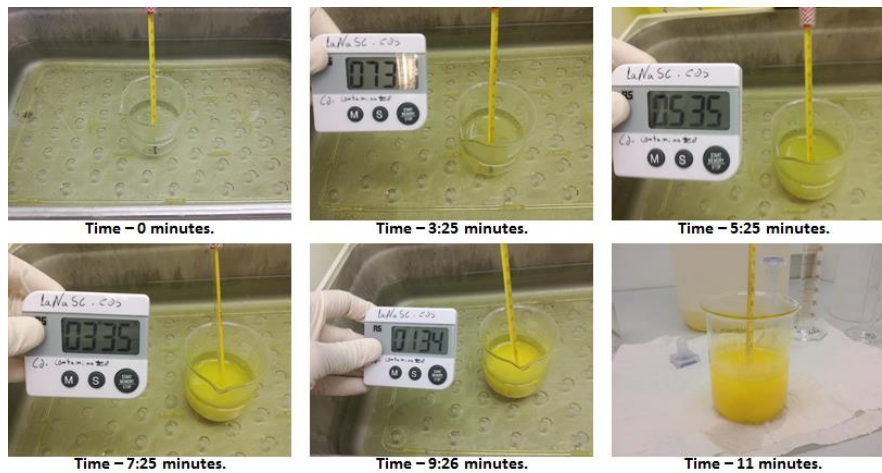
Figure 27 – Deposition bath colour evolution with time. Outer bath colour change due to camera contrast.

At a first stage, the deposition bath temperature steadily increases in the first 6 minutes. During this time, the deposition bath barely changes its colour, merely turning yellowish. This is the estimated period of time during which the deposition rate of CdS onto the samples will be very small, as the temperature is not high enough for the chemicals to interact and for the CdS to cluster.

During the second stage, the temperature increasing rate slows down, and the temperature stabilizes at 55º C. In this period the deposition bath gradually becomes more opaque and turns into a more intense yellow, as the chemicals react more intensively with the increase of the temperature, and clusters of molecules become visible inside the deposition bath. During this stage the deposition of bigger clusters of CdS is expected to occur, leading to an increase of the deposition rate and roughness of the samples.

This change in colour with the temperature of the deposition bath is associated with the deposition phenomena previously described in chapter *4.1 Chemical bath deposition*. During the first stage, ion-by-ion deposition is expected to be dominant, while the cluster-by-cluster is expected to dominate the second stage of the deposition.

6.2   Calibration experiments

All thickness measurements were performed with contact profilometry. Since the chemical bath deposition occurs everywhere on the sample, a Kapton tape was inserted in the surface of the Mo substrates. This tape is most suited for this purpose, as it does not degrade or chemically react with the bath during the deposition. After each deposition, this tape was ripped out, and the measurements were performed in this non-deposited area.

The thickness measurements have certain complications concerning their reproducibility. Firstly, the tape can lift off during the deposition (partially or completely), which precludes the measurement by either leaving no non-deposited area to measure on or by leaving a very rough surface to measure on. These complications got less relevant overtime, as extra focus was applied to this step. Secondly, a shadow effect can occur, by forming a ramp of extra material in the lateral sides of the tape. Finally, as the measurements are local, the best way to obtain reliable values is to perform a series of measurements for each sample, uncertain of the uniformity of the sample's topology on each measured area.

Therefore, for each sample, several measurements were performed and thickness values were averaged from all extracted data. Exceptional obvious outliers were not accounted for. Roughness values shown are the highest measured. Some samples do not present a thickness value (or roughness) due to measurement difficulties presented above.

Table 2 summarizes the series grown and the respective purpose of each series.

Table 2 – Grown CdS series and the respective objectives.

Series	Objective
S1	Reproducibility test
S2	Deposition time variation
S3	Outer bath temperature variation
S4	Ammonia quantity variation
S5	Deposition bath water volume variation
S6	Cadmium acetate variation
S7	Two parameters' small variation: ammonia and outer bath temperature

The default parameters are the ones that are not being changed in each series. For each series, all but the changing parameters stay with the default parameters, and these are represented in table 3.

Table 3 – Default parameters' values.

Parameter	Value
Time (min)	7
Outer bath temperature (º C)	60
Ammonia (ml)	15
Deposition bath water volume (ml)	130
Cadmium acetate (g)	0.13
Thiourea (g)	1.33

6.2.1 Series 1 – Reproducibility test

The first series of depositions, S1, is the reproducibility test, in which four default samples were grown with the following parameters: 7 min deposition, 60º C outer bath temperature, 15 ml ammonia, 130 ml deposition bath water volume, 0.13 g cadmium acetate and 1.33 g thiourea. Table 4 shows the thickness and roughness values obtained for the four samples, all rounded to integer values.

Table 4 – Thickness and roughness measurements of series 1 samples. Values rounded to integer units.

Sample	Thickness (nm)	Roughness (nm)
TL (top left)	64	20
TR (top right)	58	20
BL (bot left)	57	30
BR (bot right)	49	15

All samples present similar thicknesses, with no substantial difference between them. It is normal to obtain a thickness margin of error for samples grown with the same parameters, as CBD is a chemical method. More samples were grown with these parameters and will be presented in the next series.

Figure 28 depicts the colour of the S1 grown samples.
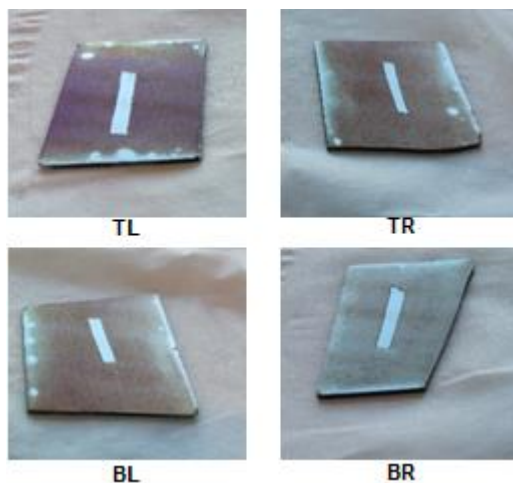
Figure 28 – S1 series grown. Middle marks correspond to the taped areas for thickness measurements.

Since the objective is to obtain CdS thicknesses of 50-70 nm, this default parameters fit the requirements. This test shows that the developed deposition system meets its objectives and also establishes a baseline for the error measurements. Due to reproducibility errors and intrinsic roughness of the films, a 15 nm variation is thus expected.

6.2.2 Series 2 – Time variation series

The second series of deposition, S2, is the time variation series. Samples were grown with deposition times between 5 minutes and 11 minutes. All parameters, other than the duration of the deposition, were kept constant throughout this series: 60º C outer bath, 15 ml ammonia, 130 ml deposition bath water volume, 0.13 g cadmium acetate and 1.33 g thiourea. For some samples, the tape was placed in the corner of the samples, to obtain more accurate measurements from both optical spectroscopy and GIXRD.

The samples with 7 minutes deposition will be called the default samples, for they were grown with the same parameters as the four samples from the reproducibility test. The sample with an asterisk will be presented in several series for comparison purposes.

Table 5 shows the deposition time *vs* thickness and roughness relation, all rounded to integer values.

Table 5 – Thickness and roughness measurement values of series 2 samples. Values rounded to integer units. Asterisk sample for comparison purposes.

Deposition time (min)	Thickness (nm)	Roughness (nm)
6	29	10
7*	64*	25*
7	109	30
7	81	30
8	100	25
9	-	-
9	186	50
9	130	40
10	163	40
11	-	-
11	225	65
11	226	65

The tape from samples with 9 and 11 minutes with no thickness values lifted off (totally or partially) during the deposition.

Figure 29 shows the deposition time *vs* thickness relationship for S1 and S2 together for all time variation samples' comparison purposes. The error bar represents the maximum roughness value extracted.
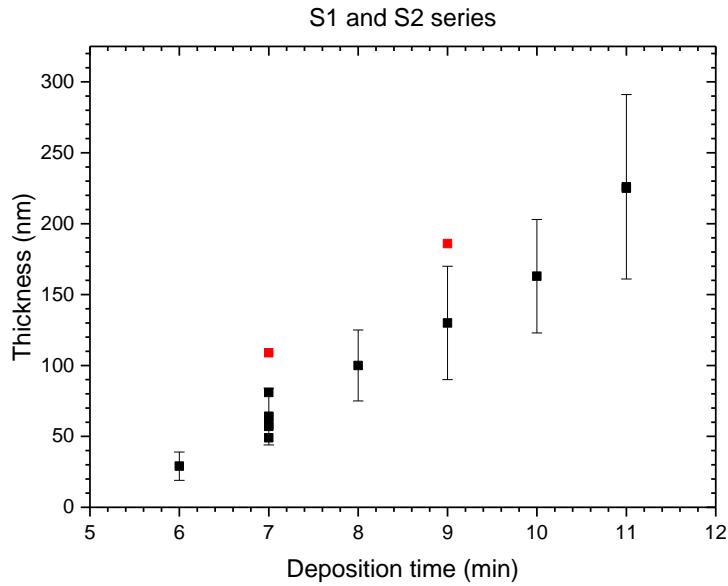
Figure 29 – S1 and S2 graphical representation. Error bar for roughness. Red marked samples' thickness deviate from expected margin of error.

Both thickness and roughness increase linearly with the deposition time. Since the longer the deposition takes the more dominant the cluster-by-cluster deposition is expected, it is anticipated to obtain higher roughness values and higher thickness discrepancy between samples with the same deposition times above 8 minutes.

The red marked samples depart from the roughness margins of error, with deposition times and thicknesses of 7 min with 109 nm and 9 min with 186 nm, respectively. These samples were some of the first samples personally grown, and it is therefore possible that the protocol of deposition was not strictly conducted, and thus these two samples can be a consequence of some minor conducting lapses such as different weighting or non-constant stirring of the bath. Nevertheless, it is important to note that, with increasing thickness and roughness values, it is predictable to obtain more discrepant values. The sample's roughness is not uniform throughout the whole sample, presenting fluctuations over the entire surface, and, again, the thickness measurements are local, presenting thus information on specific sites of the sample.

This linear deposition time *vs* thickness relationship is thus a very good result.

Figure 30 depicts the colour of the S2 grown samples.
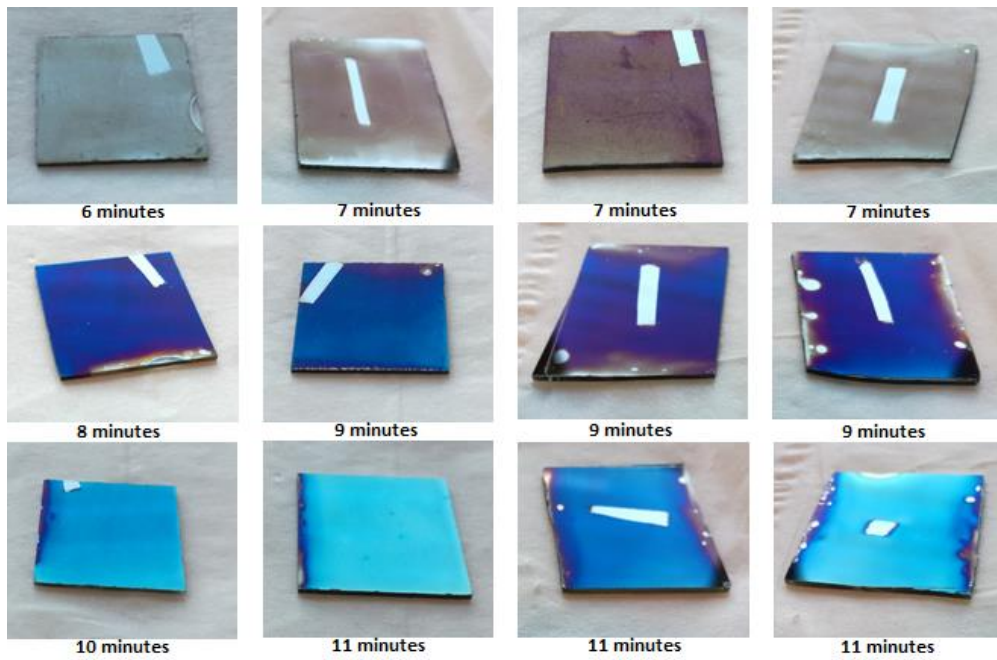
Figure 30 – S2 samples grown. Middle/corner marks correspond to the taped areas for thickness measurements.

With increasing thickness, the colour switches from greyish to brown, dark blue and then lighter blue. This colour change is due to inference of the light within the bulk of the grown film, as predicted from Bragg's law (equation 17, chapter 5.5 *X-ray diffraction*).

Hereby, a colour pattern starts to emerge and will be further analysed later on this work.

6.2.3   Series 3 – Outer bath temperature series

The third series of deposition, S3, is the outer bath temperature series. Samples were grown with outer bath temperatures between 50º C and 70º C. All parameters, other than the bath temperature, were kept constant throughout this series: 7 minutes deposition, 15 ml ammonia, 130 ml deposition bath water volume, 0.13 g cadmium acetate and 1.33 g thiourea.

Table 6 shows the outer bath temperature *vs* thickness and roughness relation, all rounded to integer values. The sample with an asterisk is a default sample, presented for comparison purposes.

Outer bath temperature (ºC)	Thickness (nm)	Roughness (nm)
50	-	-
55	43	20
60*	64*	25
65	76	35
	96	40
70	167	45
	161	50

The sample grown at 50º C was too thin to perform the measurements.

Figure 31 shows the outer bath temperature *vs* thickness relationship. The error bar represents the maximum roughness value extracted.
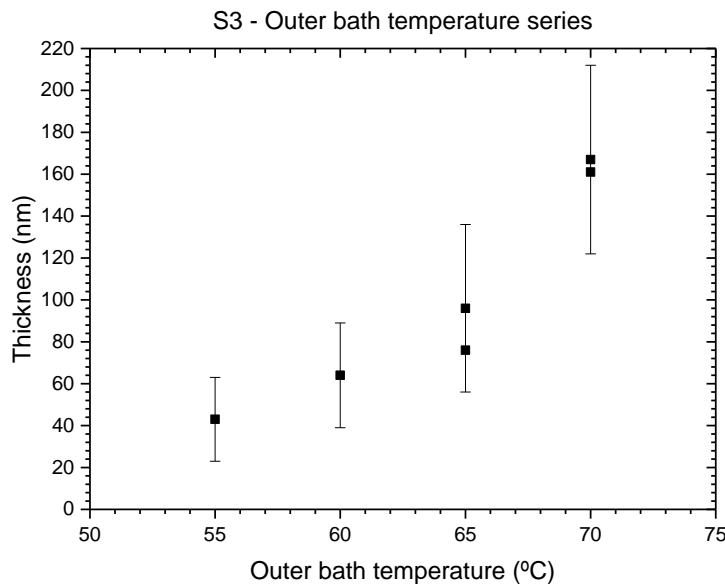
Figure 31 – S3 graphical representation. Error bar for roughness.

The thickness of the S3 resulting CdS films increases with the outer bath temperature. All of the depositions took 7 minutes, and the plot shows a small increase in the thickness values for from outer bath temperature of 55º C to 65º C, and a subtle increase for the samples deposited at 70º C. A hypothesis for the subtle thickness increase for the samples grown at 70º C might be the fact that, at those bath temperatures, the cluster-by-cluster deposition is more dominant over the ion-by-ion deposition, and thus providing with a significant thickness increase. Such assumption is based in the fact that, when comparing these depositions with the evolution of the bath temperature experiment, it is clear that both 55º C and 60º C depositions barely transited from a ion-by-ion dominant deposition into a cluster-by-cluster deposition, due to their

relatively low deposition rate. The samples deposited at 65º C and 70º C possibly took less time to transit from the first stage into the second, simply due to the higher temperature. Moreover, 65º C and 70º C samples possibly finalized the deposition with the deposition bath above 55º C, as extrapolated from the dummy experiment. The small temperature over time gradient increase is different for every outer bath temperature, and thus a linear variation was not expected.

Figure 32 depicts the colour of the S3 grown samples.
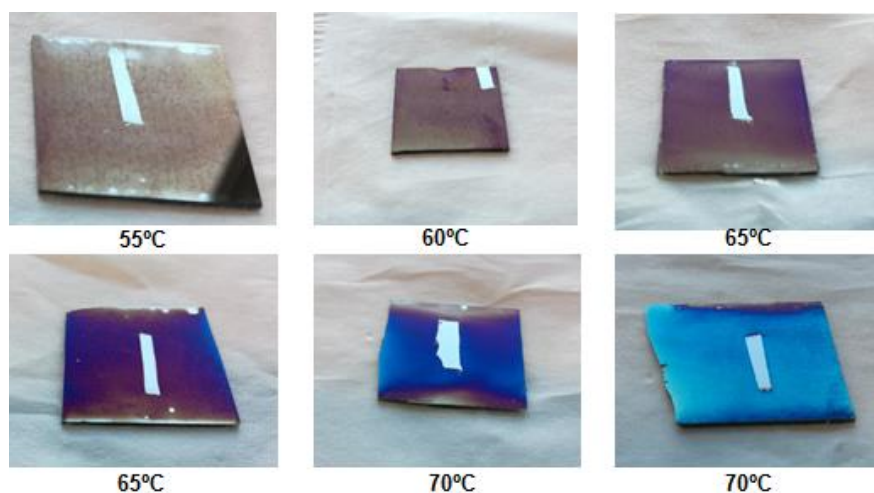
Figure 32 – S3 series grown. Middle/corner marks correspond to the taped areas for thickness measurements.

The colours from this series follow the same pattern as in the first series, turning from brown to dark blue and then into lighter blue. An intermediate colour is born between the brown and the dark blue, with a purplish tone as a mixture of these two colours. The lighter blue tonality must appear somewhere around 150-170 nm, as both 70º C samples present practically the same thicknesses of 161 nm and 167 nm and both clearly show different colours of darker blue and lighter blue, respectively.

6.2.4 Series 4 – Ammonia series

S4 represents the ammonia quantity series. Samples were grown with ammonia quantities between 9.5-18 ml. All parameters, other than the ammonia quantity, were kept constant throughout this series: 7 minutes deposition, 60º C outer bath, 130 ml deposition bath water volume, 0.13 g cadmium acetate and 1.33 g thiourea.

Table 7 shows the ammonia quantity *vs* thickness and roughness relation, all rounded up to integer values. The sample with an asterisk is a default sample, present for comparison purposes.

Ammonia (ml)	Thickness (nm)	Roughness (nm)
9.5	288	70
11	183	45
13	153	30
15*	64*	25*
17	66	15
18	27	10

Figure 33 shows the ammonia *vs* thickness relationship. The error bar represents the maximum roughness value extracted.
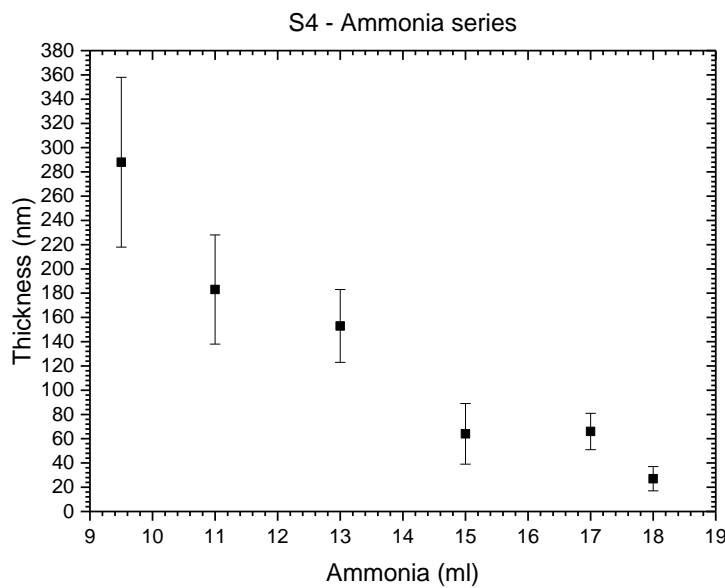
Figure 33 – S4 graphical representation. Error bar for roughness.

With increasing ammonia, the thickness of the resulting CdS samples lowers. The ammonia is responsible for the pH control of the deposition bath, and the higher the ammonia the higher the pH, i.e. the higher the basicity of the bath. The chemical reactions that take place for the CdS to form and precipitate onto the substrate are enabled with lower pH, so this relationship is expected. The sample with 17 ml ammonia presents the same thickness as the default sample (15 ml), which is not expected, since half the ammonia gradient from 18 ml to 17 ml shows a 30 nm thickness change, doubling the thickness of the 17 ml sample.

By considering Figure 33 alone, one might conclude that the sample with 15 ml ammonia is the one that does not follow the tendency. However, this is a default sample which was proven from series 1 to be well calibrated, and its thickness fits within the range of the calibrating experiment indicating thus, that the 17 ml is the outlier.

Figure 34 depicts the colour of the S4 grown samples.

Figure 34 – S4 series grown. Middle/corner marks correspond to the taped areas for thickness measurements.

Again, the same colour pattern is shown with this series.

It is noticed that the sample whose thickness deviates from the pattern, the 17 ml sample, appears with a grey colour, while the default sample (15 ml) appears brown. As the colour of the samples is clearly related with its thickness, it is very likely that the 17 ml sample has thickness lower than 60 nm, and thus this sample's thickness might not correspond to the extracted values from the contact profilometer.

6.2.5 Series 5 – Deposition bath water volume series

S5 represents the deposition bath water volume series. Samples were grown with deposition bath quantities of 110 ml and 150 ml, two growths for each one. Only deionized water was added/subtracted to obtain these deposition bath quantities, and thus the overall ratios between the chemical concentrations remained unchanged. All parameters, other than the deposition bath water volume, were kept constant throughout this series: 7 minutes deposition, 60º C outer bath, 15 ml ammonia, 0.13 g cadmium acetate and 1.33 g thiourea.

Table 8 shows the deposition bath quantity *vs* thickness and roughness relation, all rounded up to integer values.

Table 8 – Thickness and roughness measurement values of series 5 samples. Values rounded to integer units.

Deposition bath (ml)	Thickness (nm)	Roughness (nm)
110	37	15
	39	15
150	63	25
	55	25

Figure 35 shows the deposition bath quantity *vs* thickness relationship. The error bar represents the maximum roughness value extracted. The default sample was added for comparison purposes.
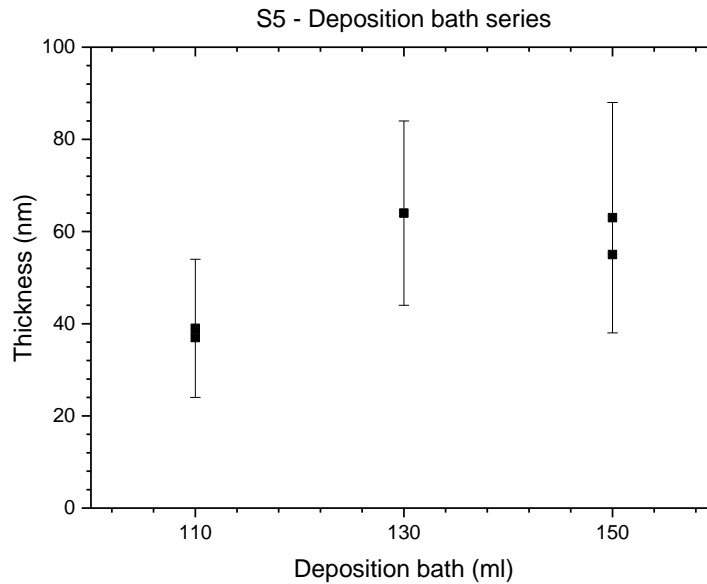
Figure 35 – S5 graphical representation. Error bar for roughness.

Samples grown with a deposition bath volume of 110 ml present lower thicknesses when compared with the other two deposition bath quantities of 130 ml and 150 ml, which roughly present the same thickness.

Different deposition bath quantities should alter some physical processes. Even though each chemical's concentrations vary, their inter-chemical concentration ratios are the same. The temperature evolution over time should change as well, as more time is needed to heat more quantity of material, which would suggest an increase of the thickness with lower deposition bath quantities. On the other hand, too low quantities make it harder and longer to dissolve the powder chemicals. These results suggest that this dissolution uneasiness surpasses the heating readiness for 110 ml deposition, while they cancel each other out for 150 ml. In general, it can be concluded that the reaction is not very sensitive to changes in the volume of the solution. Figure 36 depicts the colour of the S5 grown samples.
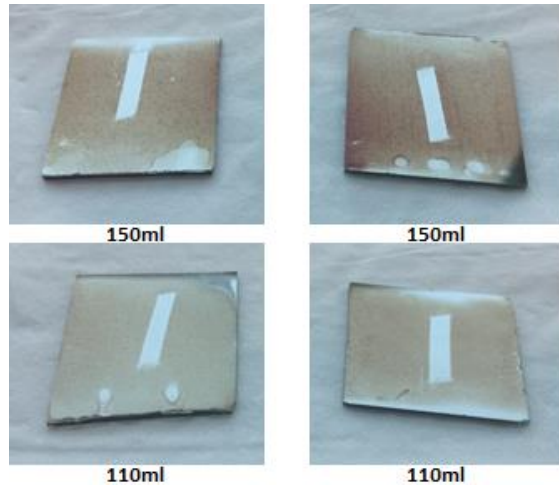
Figure 36 – S5 series grown. Middle marks correspond to the taped areas for thickness measurements.

Samples grown with 110 ml of deposition bath water volume present a lighter blue than those with 150 ml, and therefore in agreement with the thickness measurements extracted.

6.2.6   Series 6 – Cadmium acetate series

S6 is the series with different cadmium acetate quantities. Samples were grown with cadmium acetate weight varying from 0.05 g to 0.20 g. All other parameters were kept constant throughout this series: 7 minutes deposition, 60° C outer bath, 15 ml ammonia, 130 ml deposition bath water volume and 1.33 g thiourea.

Table 9 shows the relation between the cadmium acetate quantity and both thickness and roughness, all rounded up to integer values. The sample with an asterisk is a default sample, present for comparison purposes.

Table 9 – Thickness and roughness measurement values of series S6 samples. Values rounded to integer units. Asterisk sample for comparison purposes.

Cadmium acetate (g)	Thickness (nm)	Roughness (nm)
0.05	14	2
0.10	25	6
0.13*	64*	25*
0.20	58	25

Figure 37 shows the cadmium acetate quantity *vs* thickness relationship. The roughness is represented by an error bar. The error bar represents the maximum roughness value extracted.
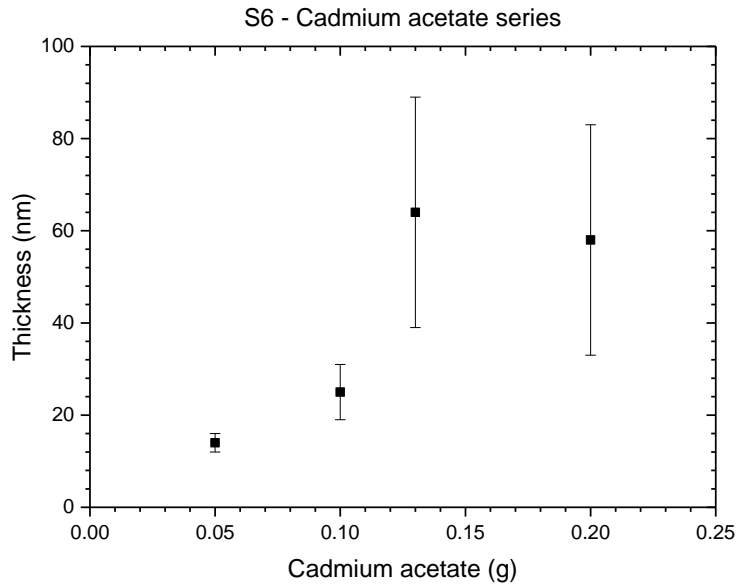
Figure 37 – S6 graphical representation. Error bar for roughness.

The thickness increases with the cadmium acetate up to 0.13 g. At 0.13 g it stabilizes with thickness values comprehended within the default expectations. The amount of cadmium with 0.05 g and 0.10 g is too small and so a limiting factor in the reaction.

Figure 38 depicts the colour of the S6 grown samples.

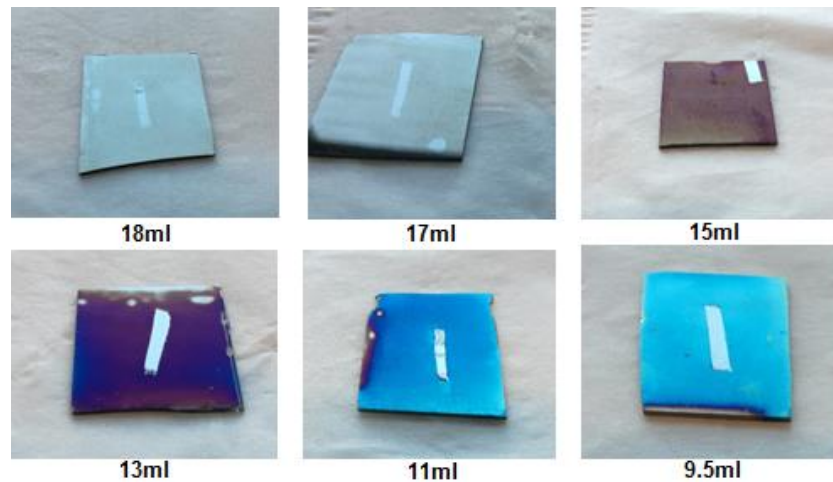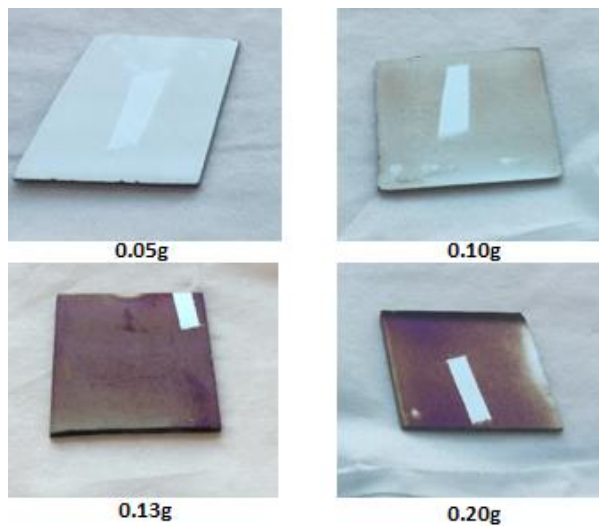*Figure 38 – S6 series grown. Middle/corner marks correspond to the taped areas for thickness measurements.*

The sample with 0.20 g presents a darker brown colour than the 0.13 g default sample, which was mistaken as an increase of the thickness with a possible increase in the density of the sample. One can hypothesize that, as the deposition only took 7 minutes, the most dominant deposition during this growth was ion-by-ion deposition. The extra cadmium in the bath deposited in very small grains, filling the empty spaces between bigger grains in the sample,

but not contributing for an increase of the thickness. Further SEM analysis on these samples could provide with this information.

It is anticipated that further and longer growths, with higher deposition times and cadmium acetate quantities, would lead to a notable thickness discrepancy between samples with different cadmium acetate amounts. This series could be completed in future work if one looks to better study this relationship.

6.2.7 Series 7 – Two parameters' small variation

S7 gathers all samples grown with more than one changing parameter. Several parameters were kept constant throughout this series: 7 minutes deposition, 130 ml deposition bath water volume, 0.13 g cadmium acetate and 1.33 g thiourea.

Table 10 shows the different parameter grown samples and the respective thicknesses and roughnesses.

Table 10 – Thickness and roughness measurement values of series 3 samples. Values rounded to integer units.

Sample	Parameters	Thickness (nm)	Roughness (nm)
S7-1	Ammonia – 16.5 ml Outer bath temperature – 55ºC	17	2
S7-2	Ammonia – 14 ml Outer bath temperature – 55ºC	93	30
S7-3	Ammonia – 13.5 ml Outer bath temperature – 65ºC	204	50

Sample S7-1, with increasing temperature and ammonia, presents 17 nm of thickness, which was expected since both increasing parameters thin down the grown film. Sample S7-2 stands with 93 nm thickness with a decrease of outer bath temperature and ammonia quantity. Even though it was not anticipated a 30 nm thickness increment when compared with a default sample, this result indicates that the ammonia has more influence than the outer bath temperature in the CBD deposition of CdS samples. S7-3 presents a natural thicker sample, with 204 nm corresponding to an increase in the outer bath temperature and a decrease of the ammonia quantity.

Figure 39 depicts the colour of the S7 grown samples.
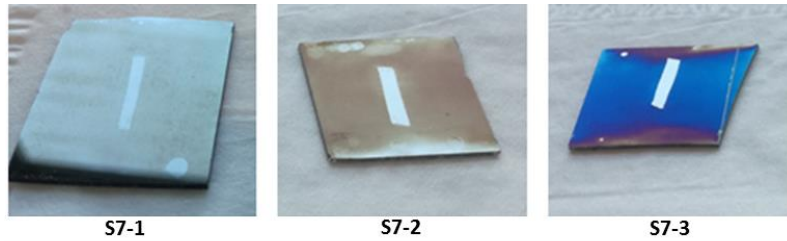
Figure 39 – S7 series grown. Middle marks correspond to the taped areas for thickness measurements.

6.3   Colour-thickness relation

Given all samples' colours, a colour framework can be generalized. Some samples were chosen from each section of thicknesses and colours, including the most deviated samples from the thickness tendency, and are depicted in figure 40.
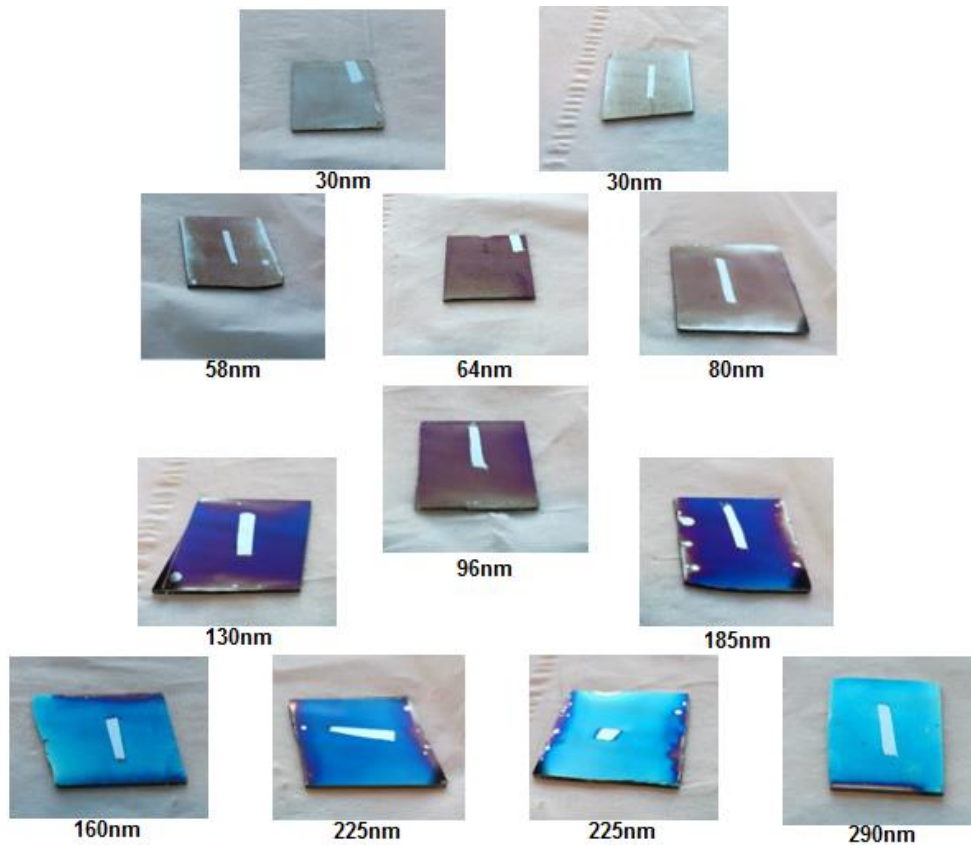
Figure 40 – Grown samples from each series.

Table 11 correlates the colour of the samples with the range of thicknesses that they belong to.

Colour	Grey/greyish	Brown/brownish	Purple	Dark blue	Light blue
Thickness (nm)	0-30	30-80	80-100 (somewhere in-between)	100-180	180-300

With this analysis, it is possible for future depositions to instantly have a very good idea of the thickness range of a sample after its deposition, merely by looking at the tonality of the sample, avoiding thus the complicated step of measuring with the profilometer.

6.4 Grazing incidence XRD

Given the low thickness range of the samples, GIXRD was performed in an 11 minutes sample from the S2 series. This sample was chosen due to its higher thickness, to assure that the GIXRD measurements would collect signals corresponding to diffracted radiation inside the CdS layer. For each measurement, the receiving detector angle scanned from 15°-65°, while the incident angle, *w*, was fixed at certain chosen angles, ranging from 0.3° up to 0.65°, with increment of 0.05°.

Figure 41 shows all GIXRD measurements taken from 11 minutes sample.
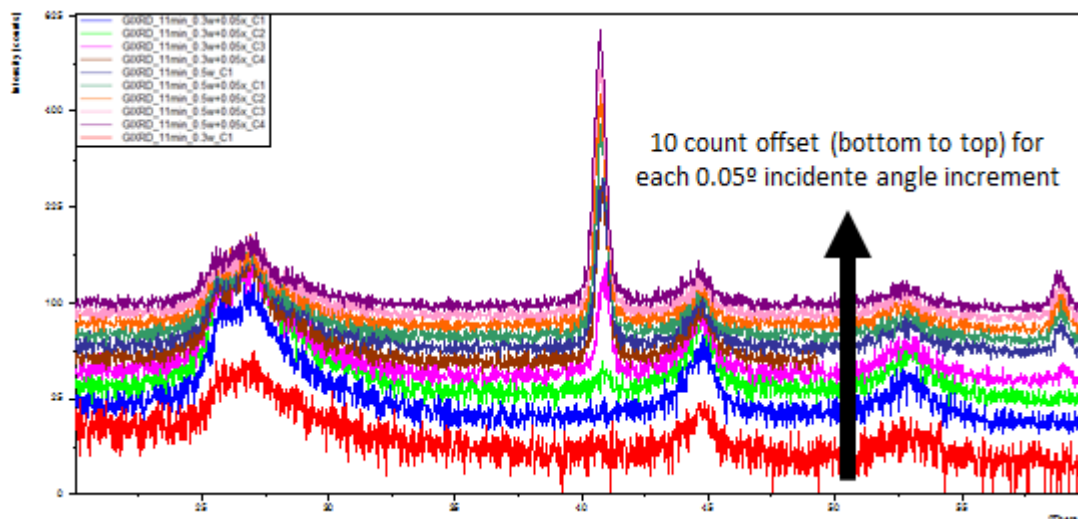
Figure 41 – 11 minutes sample's GIXRD data. 10 count offset for each 0.05° incident angle increment.

With each 0.05° incident angle increment, the peaks corresponding to 2θ angles of 40.7° and 58.8° gradually intensify, while the others peaks, corresponding to 2θ angles of 26.6°, 44° and 52.2°, either remain approximately constant or start to disappear.

Further analysis was performed to the spectra with incident angles of 0.3°, 0.45° and 0.65°, with the *Highscore* software. The software allows to input the chemical elements to look for peak

matches. The chemical elements inserted to perform the peak match were: Cd, S, Mo and O. Then the match is performed, and additional information can be acquired from the software, such as the compound name, phase and chemical structure of the material and the matching score of each peak and an overall percentage quantification of the matching peaks to the respective compounds of each XRD measurement.

This analysis is depicted in figures 42 to 44.
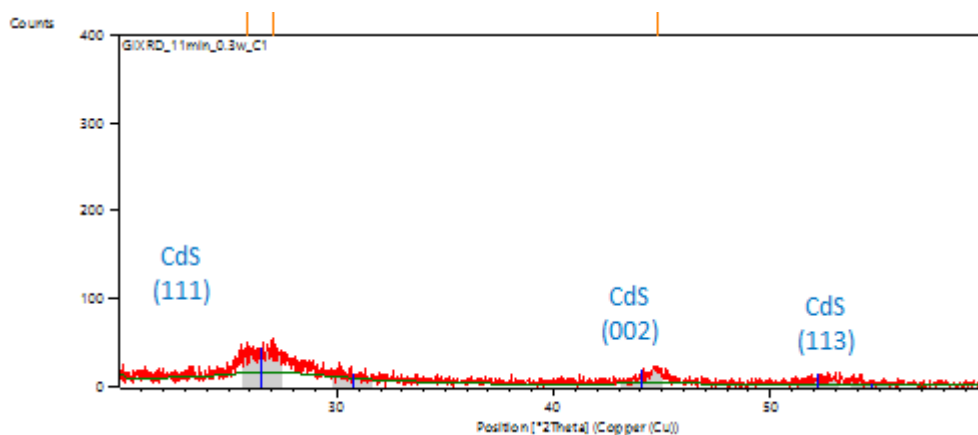
Figure 42 – 11 minute sample's GIXRD data, incident angle w of 0.30°. Blue lines correspond to CdS matching peaks retrieved from the software.
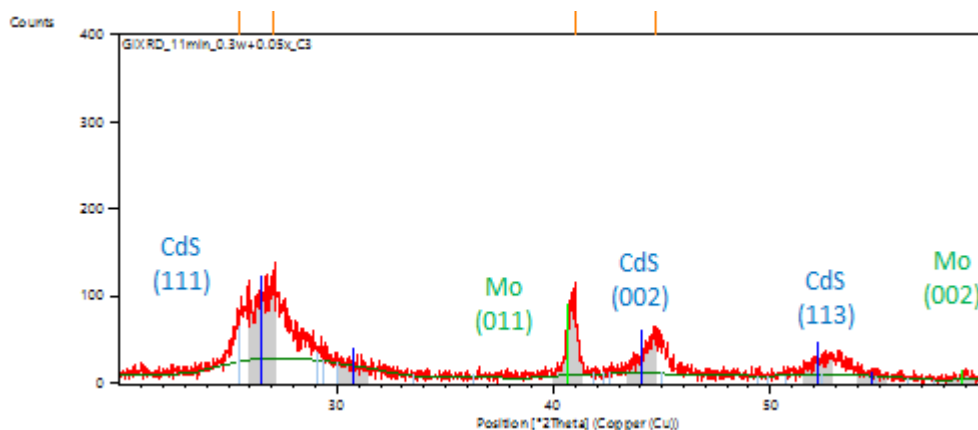
Figure 43 – 11 minute sample's GIXRD data, incident angle w of 0.45°. Blue and green lines correspond to CdS and Mo matching peaks retrieved from the software, respectively.
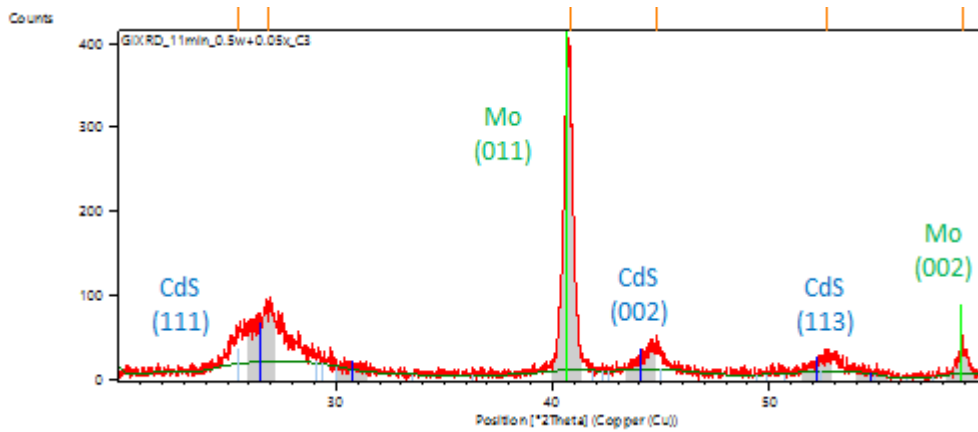
Figure 44 - 11 minute sample's GIXRD data, incident angle w of 0.60º. Blue and green lines correspond to CdS and Mo matching peaks retrieved from the software, respectively.

Table 12 shows the analysis performed by *Highscore* software on these previous GIXRD spectra. Colour pattern for graphic assessment easiness.

Table 12 – Highscore data analysis of S2 series 11 minute sample's GIXRD measurements. Colour pattern for graphic assessment easiness.

Incident angle, w (º)	Compound/chemical formula/colour	Peak matching line colour	Semi Quant. (%)	Phase
0.3	Hawleyite, Cd_4S_4	Blue	100	Cubic
0.45	Hawleyite, Cd_4S_4	Blue	62	Cubic
	Molybdenum, Mo_2	Lime	38	Cubic
0.65	Hawleyite, Cd_4S_4	Blue	11	Cubic
	Molybdenum, Mo_2	Lime	89	Cubic

With increasing incident angle, the intensity of both green peaks greatly increases, along with their percent quantity. These peaks match to the cubic Molybdenum phase and present *2θ* angles of 40.7º and 58.8º, with respective plane correspondence of (011) and (002).

Regarding the three peaks related to the cubic CdS phase, *2θ* angles and corresponding planes of 26.6º (111), 44º (022) and 52.2º (113), their count intensify from 0.30º of incidence to 0.45º, and then reduces for 0.60º.

As the incident angle increases, the incident radiation penetrates further into the sample and the collected XRD signal results from deeper layers of the sample. The Mo peaks start to appear with incident angle of 0.4º, while the CdS peaks are present in every measurement.

Literature confirms the accuracy of Mo and CdS peak matches. Several papers present the exact same peak correspondence for the CdS growths by CBD [49, 101-104], and both cubic Mo peaks corresponding to *2θ* of 40.7º and 58.8º are known as well [105, 106].

Such accurate peak correspondence evidences the presence of CdS in the cubic phase, and possible lattice strains are not of concern.

6.5 Statistical particle analysis

Optical microscopy measurements were performed in order to obtain good resolution images of the CdS clusters in the sample. The images were analysed with the software *ImageJ* to approximate the size of the clusters, their area percentage and other statistical values that enable the inference on the amount of bigger clusters in thicker samples.

Figure 45 depicts some of the images retrieved from the optical microscopy measurements on some samples from the series S2, 100x magnification lens.
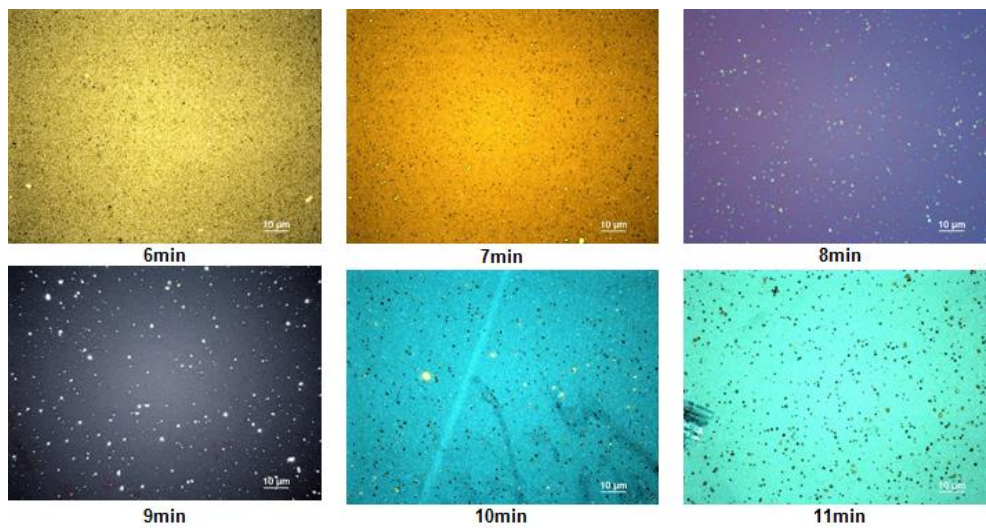
Figure 45 – Optical microscopy imaging of the S2 series samples, 100x magnification.

These images were then analysed with *ImageJ*. Figure 46 present some screenshots of the software.
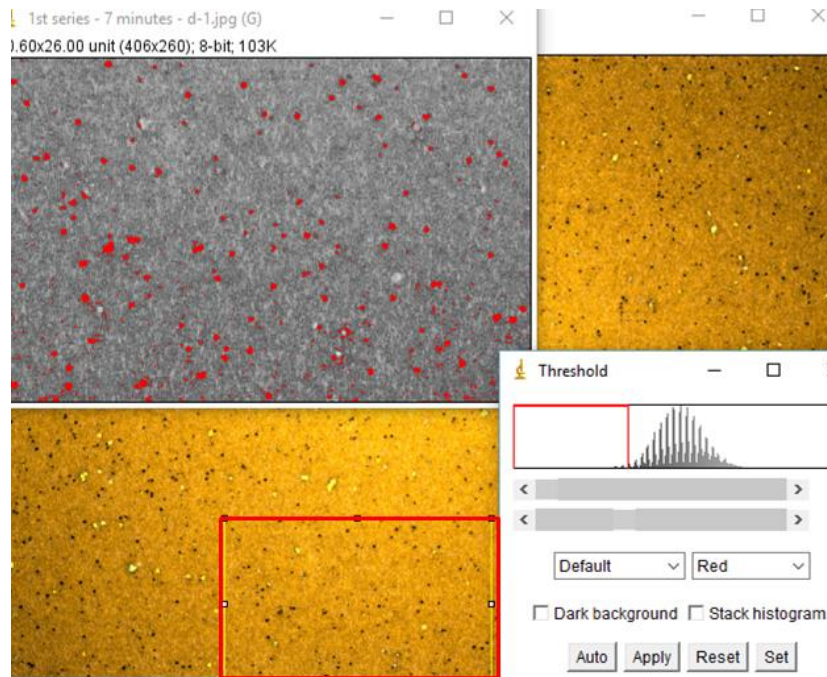
Figure 46 – ImageJ analysis windows of the default sample. Background (brown) image is the original optical microscopy image. Bottom left area (red outline) is the chosen section of the image Top left (grey) area is the chosen area in 8-bit format. Bottom right window for the grain threshold quantities to analyse.

The original image is selected, from which an area of interest is outlined. The image is converted into an 8-bit image, enabling the software to perform a statistical analysis of the chosen area and threshold.

The most important statistic factors to proceed with this analysis are both area percent and average size of the particles. Several images from each sample were taken and analysed. Figures 47 and 48 show both average size and average area percent of the particles, averaged for each sample.
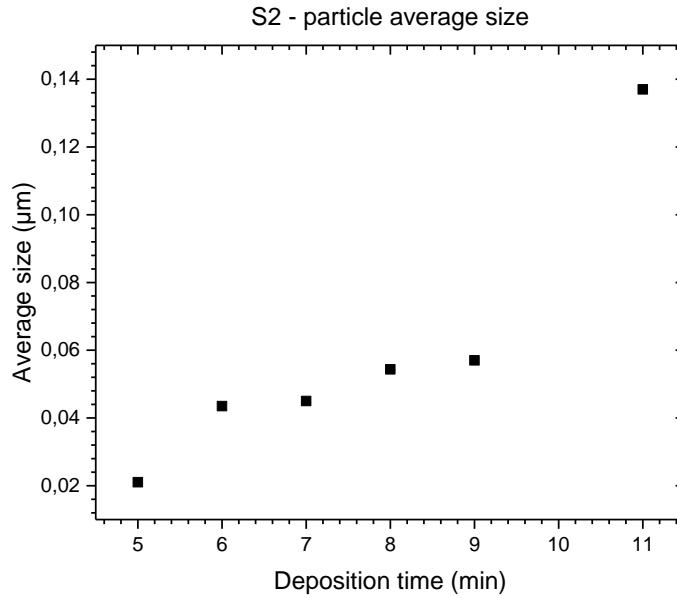
Figure 47 – S2 particle average size relation with deposition time.
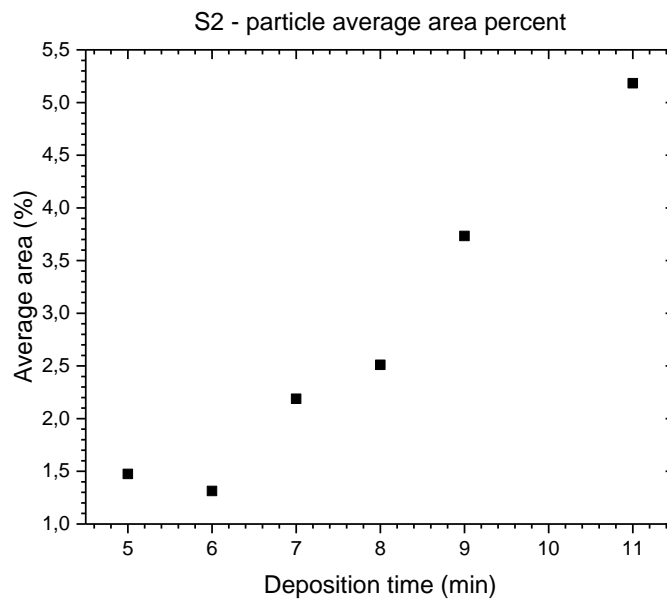
Figure 48 – S2 particle area percent relation with deposition time.

Images taken from 10 minutes sample were too dark to evaluate the grain parameters. With increasing deposition time, and therefore increasing thickness, the samples present bigger grains and larger amount of grains. This tendency is only broken with the average area percent of the sample with 6 minutes, which is somehow smaller than the 5 minutes, sample but still a small difference. Noting that the threshold selection is very tricky, given that it is very hard to always pick the same percentage of the darkest particles from the 8-bit images, and that the

average size of the particles of this 6 minutes sample still matches the tendency, the differences between the two samples are within error margins.

All the data analysed from *ImageJ* strongly supports the hypothesis presented in chapter *6.1 Evolution of the bath temperature experiment*. The small increases in both particle parameters up to 9 minutes of deposition suggest the dominance of the ion-by-ion deposition, and the appearance of the middle-stage mixed deposition, showing the arising of the cluster-by-cluster deposition dominance. Both grain size and area percent greatly increase from 9 minutes to 11 minutes samples, hereby limiting the threshold between mixed deposition and cluster-by-cluster dominance deposition. From a solar cell point of view, it should be noted that the presence of big CdS particles is unwanted, since it increases the roughness of this layer and it can ultimately lead to reduced light absorption in the CIGS layer.

7. ZnO:Al RESULTS

Four samples were firstly grown for this work. More samples were anxiously anticipated and programed, but could not be grown due to technical difficulties with the ALD equipment, as the precursor gases' path into the deposition chamber was compromised and it was realized that the deposition process compromised the quality of the CIGS absorber layer.

Several measurements were performed to characterize the ZnO:Al samples grown for this work. Firstly, optical spectroscopy was performed, in order to obtain transmittance measurements, followed by thickness and bandgap energy calculations. SEM and AFM images were taken, in order to obtain topography elements from the surface of the samples. XRD was performed to obtain chemical and structural characterization. Hexagonal structure equation, Bragg's law and Sherrer equation were used to further assess some important structural parameters. Finally, a chemical etching was performed in the samples in order to confirm the thickness calculations from optical spectra with contact profilometry measurements.

Most results are compared with the results of a state-of-the-art sample prepared at Uppsala University by sputtering. Further details and comparison with results from the literature on each analysis are described throughout the chapter.

7.1 Optical spectroscopy

Transmittance measurements performed on ZnO:Al samples were made with the 2D Detector Module, with scanned wavelengths ranging from 250 nm to 2000 nm (250-1000 nm for the Uppsala reference sample).

Due to the nature of this transmittance technique, a glass sample was placed in the reference position to be compared with the ZnO:Al transmittance measurements.

Figure 49 shows the transmittance data collected from the glass substrate.
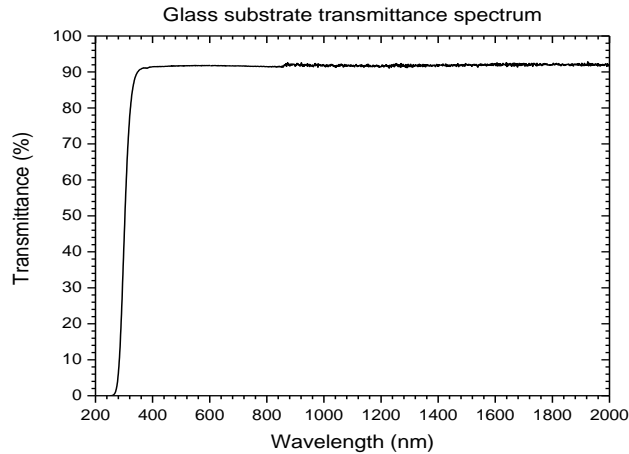
Figure 49 – Glass substrate transmittance spectrum.

All the remaining transmittance spectra data presented take into account the glass substrate reference spectrum.

The main CIGS solar cell performance occurs with incident radiation wavelengths ranging from 520-1100 nm [2, 66]. With the interference fringes of the transmittance spectra of the samples, a broader range of wavelengths was considered to better estimate an average transmittance of the samples, from 450-1200 nm.

Figure 50 reflects the transmittance spectra of the ZnO:Al samples and the Uppsala sample, and presents the estimate average transmittance within the reported range.
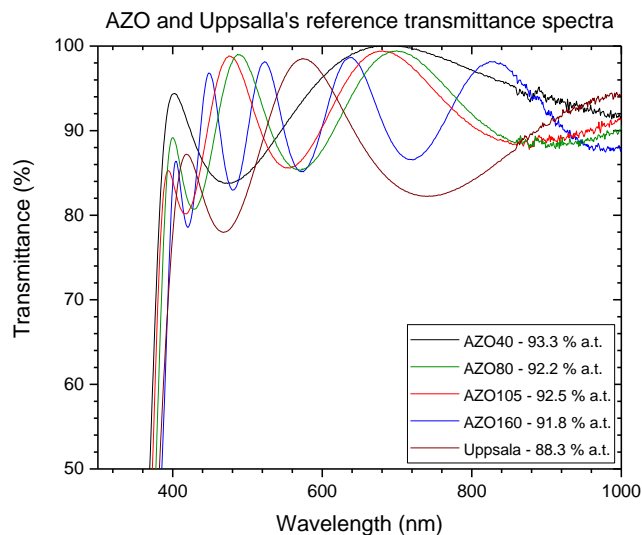
Figure 50 – Transmittance spectra of ZnO:Al samples and Uppsala's reference sample. Average transmittance (a.t.) (450-1200 nm wavelength range) in caption.

All average transmittance values are superior to 90 %, and the increase in the thickness reduces the transmittance, as it is expected.

Other similar growths in the literature, concerning deposition temperatures, materials and Zn:Al ratios, obtain transmittance values above 80 % for ZnO:Al samples with thickness around 50-100 nm [31, 33, 83, 85]. These transmittance values would be lower for thicker samples with 400-700 nm, confirming the high transmittance (above 90 %) of the ZnO:Al samples grown in this work.

With the optical spectra data, it is possible to calculate both bandgap energies and thicknesses of the samples. These calculations will be now described and evaluated.

7.1.1 Bandgap calculation

Firstly, the bandgap energy was calculated. The absorption coefficient can be calculated through the Beer-Lambert equation, given by equation 29:

$$\alpha = log_{10} \frac{I_0}{I} \qquad \textit{Eq. 29}$$

, where α is the absorbance, I_0 is the intensity of light passing through the reference cell during the optical spectroscopy measurements and I is the intensity of light passing through the sample. Plotting α^2 vs hv (Planck's constant times the frequency) gives a straight line in a given hv range, from which the bandgap energy value can be extrapolated at $\alpha^2=0$.

Figure 51 plots α^2 vs hv for the ZnO:Al samples and the extrapolated straight lines to $\alpha^2=0$.
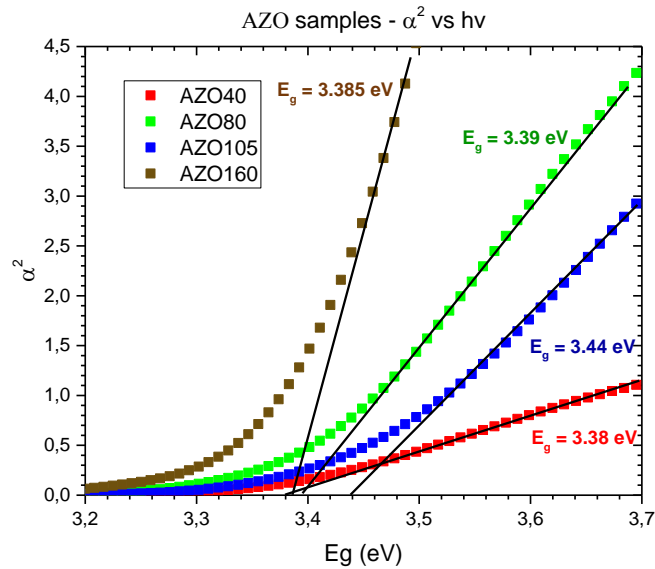
Figure 51 – ZnO:AL samples' α^2 vs hv curves.

AZO40 presents a bandgap energy of 3.38 eV, while AZO80's bandgap energy is closer to 3.39 eV and AZO106's stands in between. Such small deviations are not relevant. AZO105, with

lower Zn:Al deposition cycle ratio, presents a slightly higher bandgap energy of approximately 3.44 eV. This result is expected, as most results throughout the literature link higher bandgap energies with a higher Al doping in ZnO:Al samples [57, 84, 85, 107].

7.1.2 Thickness assessments

Secondly, the Swanepoel method was applied to the transmittance spectra data. Two consecutive minimum fringes from each graphic were picked to start the calculations. The value of the refractive index of the substrate, *s*, was calculated from equation 20, chapter *5.6.2 Swanepoel method*. It is a function of the transmittance data of the substrate, $T_s(\lambda)$, which is a function of the wavelength. Nevertheless, as the glass substrate transmittance is fairly constant throughout the wavelengths ranging 350-2000 nm, a medium average value of 1.52 for its refractive index was estimated and used in every calculation for each sample.

Table 13 shows chosen minimum transmittance values and respective diffraction index values, and the thickness, *t*, calculated for each sample, along with AZO40 fit value.

Table 13 – Swanepoel parameters for each ZnO:Al sample. λ_1 and n_1 for the wavelength and refractive index of the first peak chosen, λ_2 and n_2 for the respectives of the second peak chosen, d for the thickness calculated.

Sample	λ_1 (nm)	n_1	λ_2 (nm)	n_2	t (nm)
AZO40	-	-	-	-	240
AZO80	917	1.67	571	1.75	400
AZO105	877	1.67	557	1.74	410
AZO160	721	1.71	575	1.76	735
Uppsalla reference	739	1.85	468	1.98	290

AZO40 sample did not present sufficient peaks to apply the Swanepoel method, thus its thickness was estimated through a linear fit of the remaining samples. Three points are seldom enough to plot a linear fit, but this is a peculiar case. On one hand, this should suffice for an approximate thickness value of the AZO40 sample, due to the straightforward scale-up nature of the ALD deposition technique [74, 76]. On the other hand, it is known that every deposited material presents an interface thickness adaptation, where the lattice of the deposited material is still adjusting to the substrate's structure, and there is therefore an offset thickness from which the deposition rate stands unaltered. The presence of this deposition rate threshold is usually evidenced by a negative thickness offset. Through the linear fit, the obtained value for the AZO40 thickness is 240 nm.

Figure 52 graphically represents the relation between the thickness and the total ZnO cycles of each sample obtained for the Swanepoel method calculations and the extrapolated AZO40 as well. Only the ZnO cycles were considered in order to fairly compare the samples with different Zn:Al cycle ratio depositions.

Equation	y = a + b*x
Plot	Thickness
Weight	No Weighting
Intercept	81,19756
Slope	0,20421
Residual Sum of Squares	114,67244
Pearson's r	0,99955
R-Square(COD)	0,9991
Adj. R-Square	0,99865
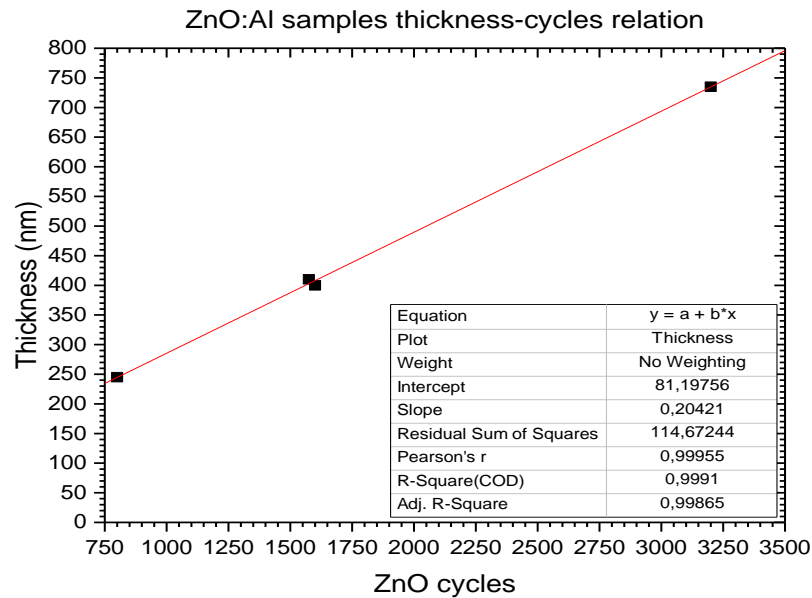
Figure 52 – ZnO:Al samples' thickness-ZnO cycle relation.

The linear fit curve intercepts the thickness axis in a positive position, which is obviously evidence that this fit does not represent the real event evolution overtime. The conclusion is that the thickness of the sample AZO40 is most certainly overestimated, and that further points would be needed for a more precise estimation. The resolution granted with this fit is however good enough for the performed evaluations.

After obtaining the optical thickness values, contact profilometry was performed for thickness comparison assessments.

To do so, as the film is continuous throughout the whole sample, an etching was performed in order to expose the substrate by fully removing the ZnO:Al layer. Chloride acid was carefully handled to delimitate the area of etching, and then the measurements were made after cleaning and drying the samples. This etching approach does eliminate the deposited film, but it also compromises the measurements, for the vapours of the acid alone can react with the deposited material and partially remove it. Thus, very accurate values are not expected, but very approximate values are desired.

Presented values were averaged from all values obtained, and are available in table 14, along with the thickness values obtained from optical calculations.

Table 14 – Averaged optical and profilometry thickness of ZnO:Al samples.

Sample	AZO40	AZO80	AZO105	AZO160
Thickness (nm) Profilometry	-	391	392	695
Thickness (nm) Optical calc.	240	400	410	735

Sample AZO40 did not allow to obtain precise measurements, as the sample was too damaged from the etching, and it is therefore impossible to accurately infer on its thickness. Samples AZO80 and AZO105 present very surprisingly accurate values of profilometry thickness, with an irrelevant error considering the measurement conditions. AZO160 presents a higher thickness discrepancy, but still too low to be considered. Through a fit of the profilometry thickness results, the AZO40 sample also obtains a 240 nm thickness.

It can be concluded that the optical thickness calculations are effectively very good approximations, and thus only the thicknesses calculated with the Swanepoel method will be considered from this point on.

7.1.3   Deposition rate

To proceed with the deposition rate calculations of the ZnO:Al samples, some considerations were taken into account. Firstly, the Al concentration is significantly smaller than the Zn concentration, as the Zn:Al deposition cycle ratios of 20:1 and 15:1 are very high. Secondly, the deposition rate is higher for ZnO when compared with Al_2O_3, as observed in many ZnO:Al-by-ALD papers [31, 33, 56, 57, 108]. For the same chemistry as the one used in this work, typical values for the ZnO deposition ratios range between 1.75-2.25 Å, while Al_2O_3 deposition ratios vary between 1-1.4 Å. Both ZnO and Al_2O_3 deposition ratios don't seem to vary much with different substrates and they are not considerably affected by the temperature.

Considerations made clear, the deposition rates of the samples were calculated by dividing the total number of ZnO cycles alone by the thickness of the respective samples, neglecting then the minimal thickness influence of the Al_2O_3 cycles.

Table 15 presents these values.

Table 15 – Deposition rates calculated for ZnO:Al samples, considering optical thickness values and ZnO deposition cycles.

Sample	ZnO cycles	Optical Thickness(nm)	Deposition rate (nm/cycle)
AZO40	800	240*	0.31*
AZO80	1600	400	0.25
AZO105	1575	410	0.26
AZO160	3200	735	0.23

AZO80, AZO105 and AZO160 present very closely acceptable values for deposition ratios. AZO40 presents an unexpected deposition rate of 0.31 nm per cycle, which is particularly high. This result further evidences the irregularly high thickness fit for this sample, for an expected lower thickness would lead to an also expected lower deposition rate.

The deposition rates obtained for the other samples are slightly higher than those previously reported. Some papers associate a higher deposition rate per cycle for specific temperatures of 150ºC [33, 83], even though they present deposition ratios within the usual ranges [31, 33, 56, 57, 83, 108].

Considering that the deposition rates are slightly overestimated, as the Al_2O_3 layers were set aside for along the calculations, and that each ALD setup results in different deposition rates, the obtained deposition rates for samples AZO80, AZO105 and AZO160 stand within expectations.

7.2 Resistivity

Sheet resistivity measurements were performed on the four grown samples and on the reference sample from Uppsala. All measurements were performed in the middle of each sample.

Table 16 shows the sheet resistivity values measured for each sample and the samples' respective resistivity values.

Table 16 – Sheet resistivity values obtained and calculated resistivity of ZnO:Al samples.

Sample	Sheet resistivity ($\Omega.\square^{-1}$)	Optical thickness (nm)	Resistivity ($\Omega.cm$)
AZO40	222.6	240	$5.45*10^{-3}$
AZO80	99.9	400	$3.63*10^{-3}$
AZO105	99.8	410	$3.69*10^{-3}$
AZO160	78.4	735	$5.24*10^{-3}$
Uppsalla reference sample	36.2	290	$1.05*10^{-3}$

All ZnO:Al samples present the expected low resistivities within the order of magnitude of 10^{-3} $\Omega.cm$, which are compatible with the best values found in the literature [32, 56, 57]. It is interesting that samples AZO80 and AZO105 have practically the same resistivity, for, even though they have practically the same thickness, their Zn:Al cycle ratio is different.

Concerning the Uppsala's reference sample, the respective resistivity of $1.05*10^{-5}$ $\Omega.cm$ is indeed a reference, as it stands between the best values on the literature. This sample is thus a great term of comparison for the samples grown in this work, noticing once more that it was deposited by sputtering which normally provides films with lower resistivity values than ALD-deposited films.

Even though the resistivity values are good, the expected sheet resistivity values were of 30-50 $\Omega.\square^{-1}$, as the sheet resistivity from Uppsala's sample. Fortunately, these can be changed by increasing the thickness of the samples. The resistivity is an intrinsic parameter for each chemical structure, but the sheet resistivity can be improved with the thickness.

The next steps for the development of the ZnO:Al layers would require the deposition of thicker samples. The main anticipated changes would be a small decrease of the transmittance, down to those values found in the state-of-art ZnO:Al layers, approximately above 85 %, and a decrease in the sheet resistivity down to values around 50 $\Omega.\square^{-1}$.

Better sheet resistivity values can be obtained after thermal annealing treatments or by other deposition methods [86], which are not compatible with CIGS solar cells and thus those were not explored in this work.

7.3 SEM and AFM

Figures 53 and 54 show the SEM images taken to the ZnO:Al samples, with magnification of 82 880x and 414 400x, respectively.
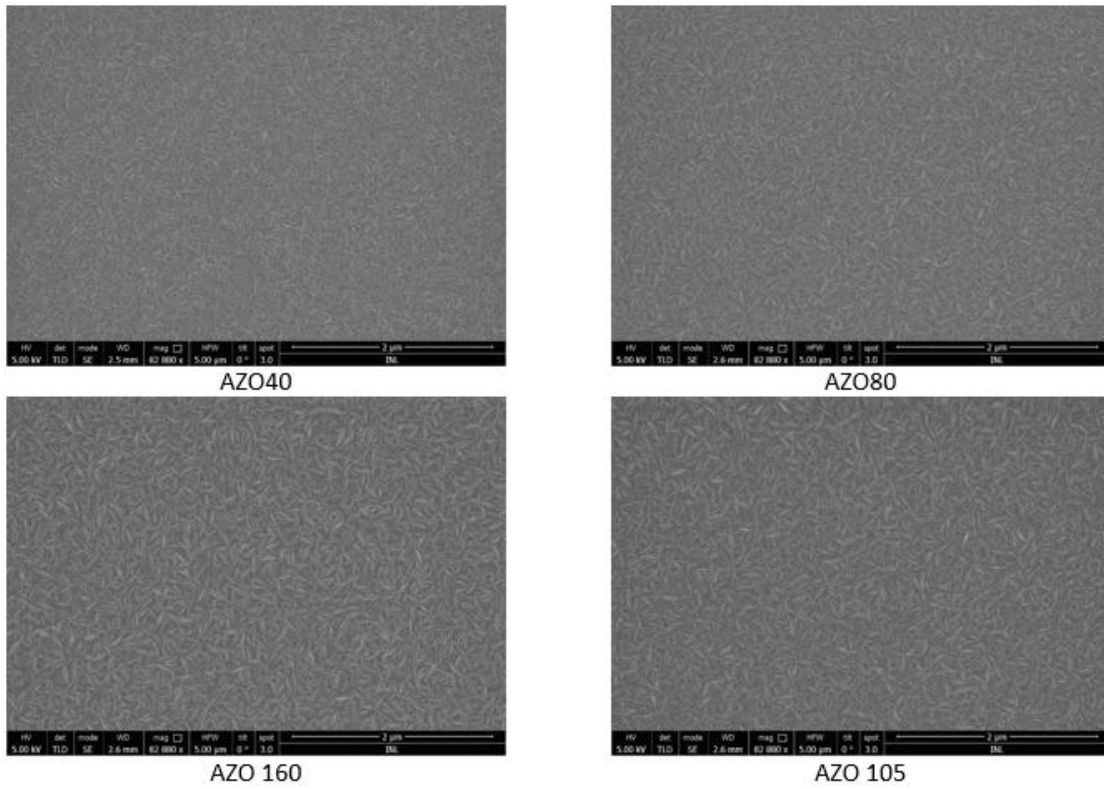
Figure 53 – ZnO:Al samples' SEM imaging, 82 880x magnification.
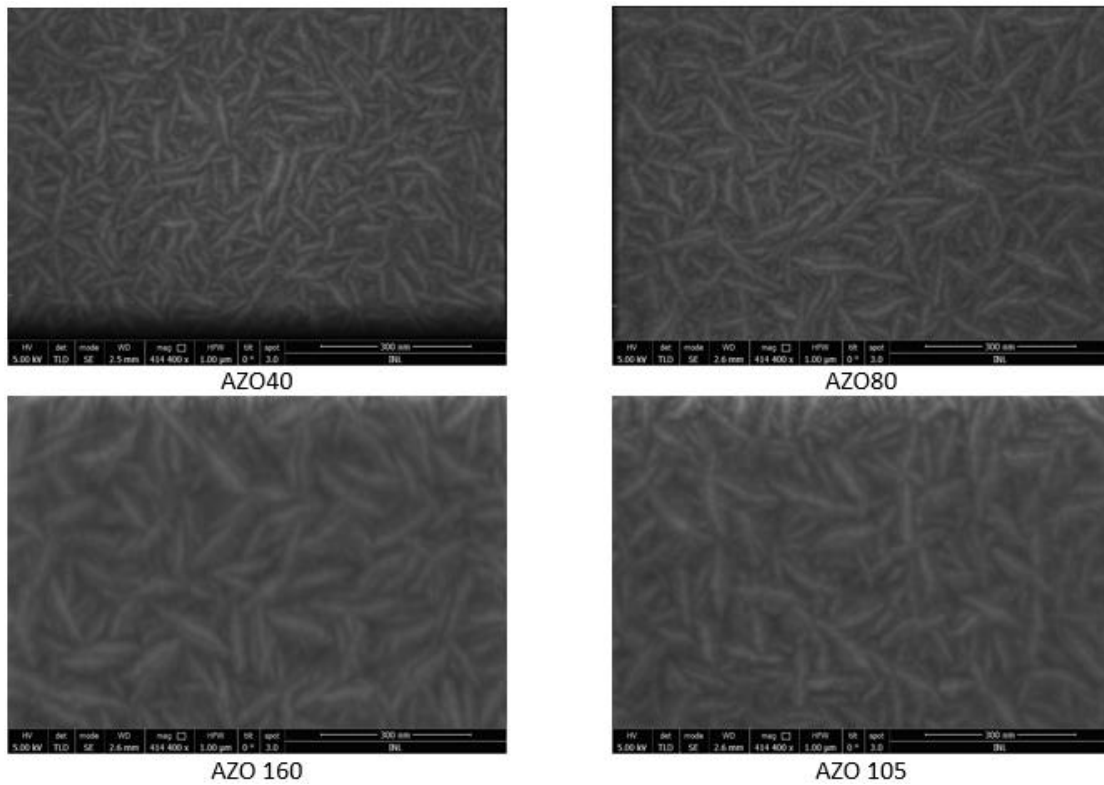
Figure 54 – ZnO:Al samples' SEM imaging, 414 400x magnification.

The films are relatively smooth with a uniform distribution of grains, and the grains have the same type of rice-like morphology, randomly distributed over the surface. The grain sizes

increase with the thickness of the sample. AZO40 and AZO80 grain sizes' are approximately 60-100 nm length and 10-20 nm width. AZO105 and AZO160 grains have approximately 80-150 nm length and 15-30 nm width. Since AZO105 clearly presents larger grains than AZO80, it can be concluded that, even though the change in the Zn:Al cycle ratio does not change the thickness nor the resistivity, it does change the morphology of the samples.

Both grain size and sample's uniformity are very close to those found in the literature [86]. Specified studies on the relation between grain size and Zn:Al deposition ratios were not found, and thus it would be interesting to perform such a study. Comparing different deposition temperatures within each deposition ratio would be useful as well, in order to calibrate the grain size for each Zn:Al cycle ratio with the best resistivity values. An accurate study on the grain size, GS(Zn:Al), *vs* resistivity, ρ(Zn:Al) relation would ease further studies on ZnO:Al by ALD. EDX measurements were performed during the SEM picture captions. These were not considered due to the nature of the measurements themselves. Even though the size of volume interaction depends on the accelerating voltage applied, this volume of interaction does not provide an accurate EDX measurement for such thin films.

Figures 55 and 56 show the AFM images taken to the ZnO:Al samples. Images retrieved by the software present 1x1 μm and 3x3 μm image sizes.
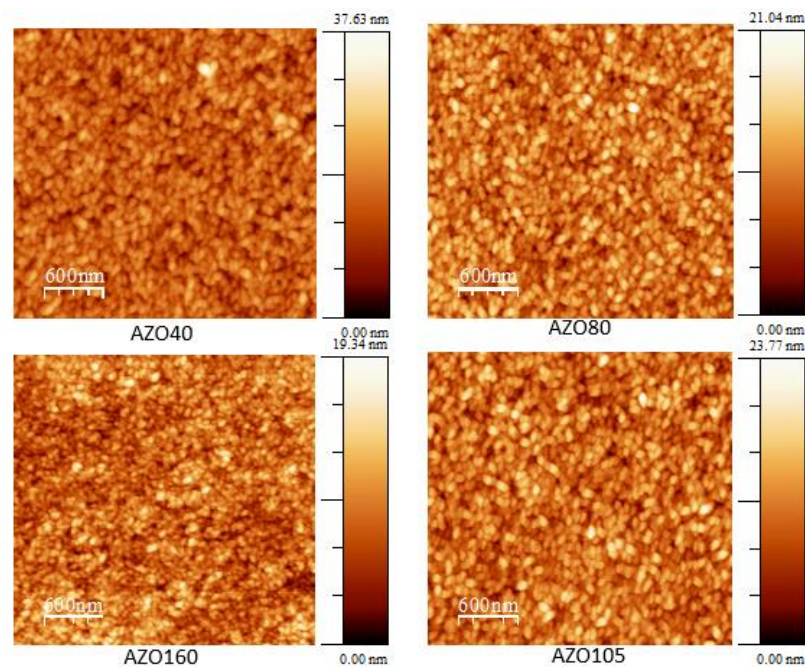
Figure 55 – ZnO:Al samples' AFM imaging, 3x3 μm image size.
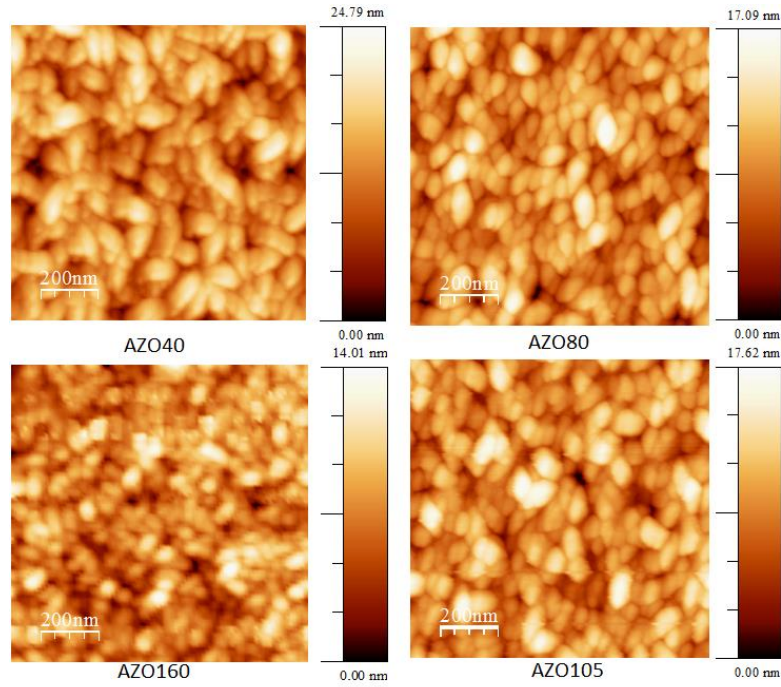
Figure 56 – ZnO:Al samples' AFM imaging, 1x1 μm image size.

Table 17 shows the roughness average of each image taken of the ZnO:Al samples and the respective root mean square roughness, collected from the imaging analysis software incorporated with the AFM equipment.

Table 17 – Average roughness of AFM images taken to the ZnO:Al samples. Colour pattern for comparison purposes.

Sample	Size (μm)	Roughness average (nm)
AZO40	3x3	3.73
	1x1	3.0
AZO80	3x3	2.11
	1x1	1.96
AZO105	3x3	2.41
	1x1	2.1
AZO160	3x3	2.0
	1x1	1.68

Comparing the samples with the same Zn:Al deposition cycle ratios, AZO40, AZO80 and AZO160, it is clear that the average roughness decrease with increasing number of supercycles and thus with the thickness of the sample.

Nevertheless, these roughness values are indeed very small. Additionally, the substrates on which the Al:ZnO layers were deposited naturally present an intrinsic roughness. Therefore,

these roughness values can be considered almost irrelevant and a proof of the uniformity and homogeneity provided by the ALD technique.

Both imaging and roughness values are very similar to those on the literature, such as 0.75-1.25 nm and 0.1-3 nm [31, 57].

7.4 XRD

XRD measurements in the Bragg-Brentano configuration were performed, and the respective analysis was performed with the software *Highscore*, whose operating principles were previously mentioned in chapter *5.4 Grazing incidence XRD*. The elements introduced were Al, Zn, O and Mo, i.e. the deposited elements and the Molybdenum from the substrate.

Figures 57 to 60 present the XRD measurements taken from the ZnO:Al samples, along with the respective peak correspondence. Following tables 18 to 21 present the data analysis from the software *Highscore*, respective to the preceding figure.
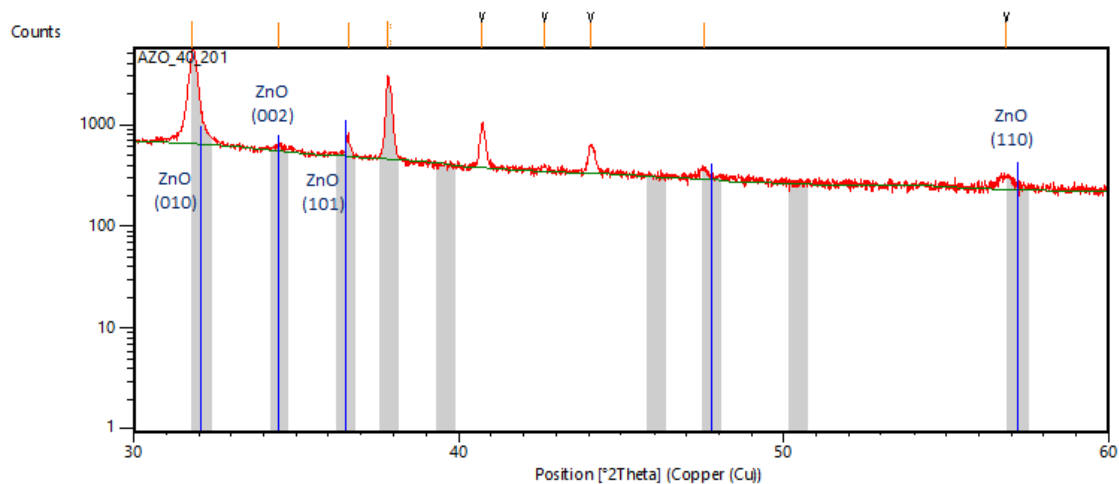
Figure 57 – AZO40 (240 nm) XRD data. Vertical blue lines correspond to the matching peaks found by software Highscore, corresponding to Zincite compound.

Table 18 – Highscore data analysis of AZO40 sample's XRD measurements. Colour pattern for comparison purposes.

Peak colour	Compound	Chemical formula	Phase
Blue	Zincite	Zn_2O_2	Hexagonal

80
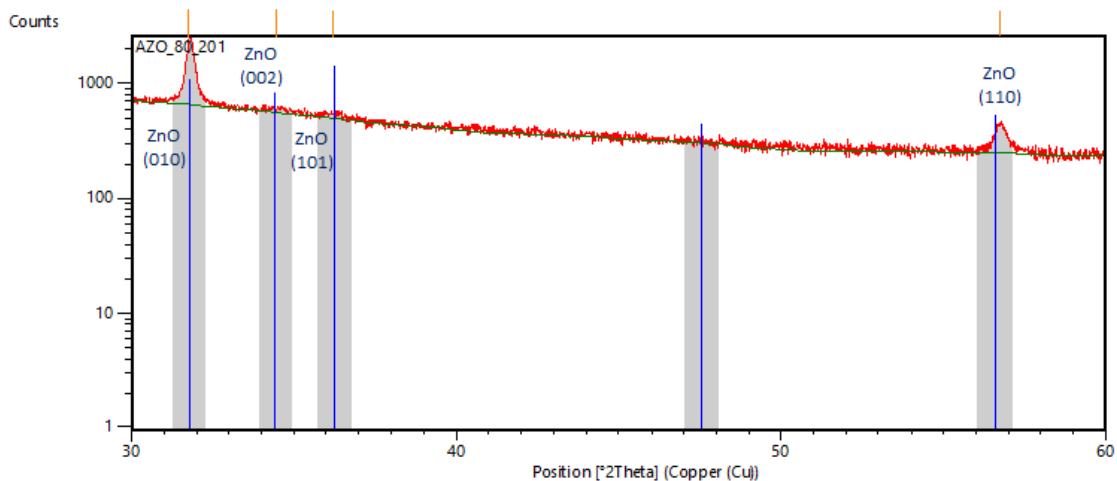
Figure 58 – AZO80 (400 nm) XRD data. Vertical blue lines correspond to the matching peaks found by software Highscore, corresponding to Zincite compound.

Table 19 – Highscore data analysis of AZO80 sample's XRD measurements. Colour pattern for comparison purposes.

Peak colour	Compound	Chemical formula	Phase
Blue	Zincite	Zn_2O_2	Hexagonal
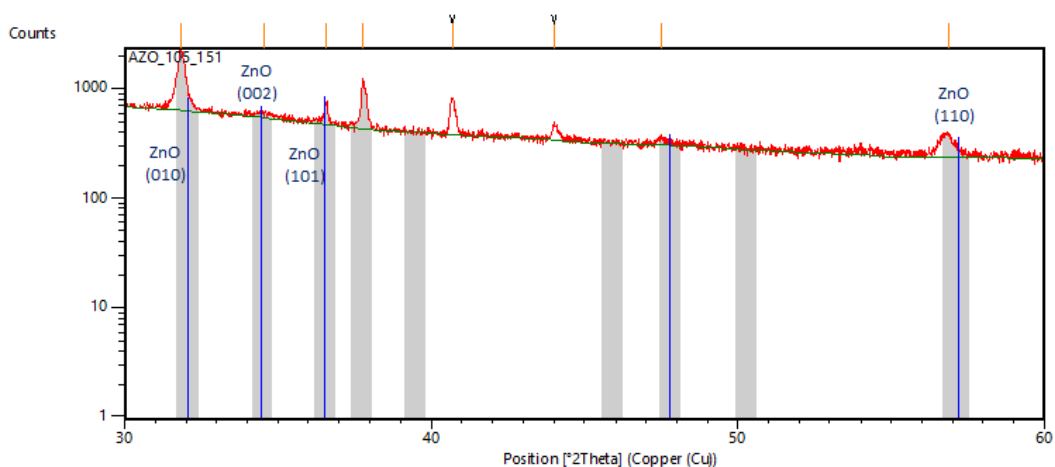
Figure 59 – AZO105 (410 nm) XRD data. Vertical blue lines correspond to the matching peaks found by software Highscore, corresponding to Zincite compound.

Table 20 – Highscore data analysis of AZO80 sample's XRD measurements. Colour pattern for comparison purposes.

Peak colour	Compound	Chemical formula	Phase
Blue	Zincite	Zn_2O_2	Hexagonal
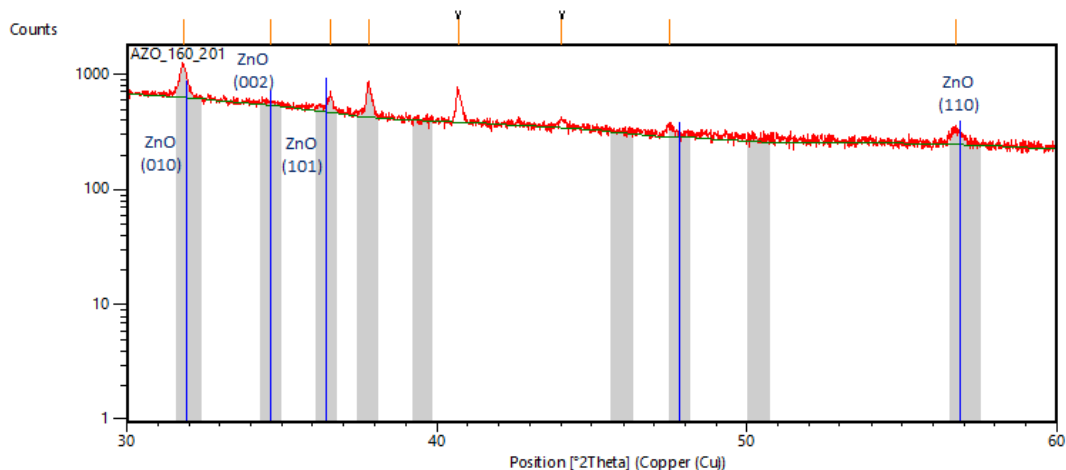
Figure 60 – AZO160 (735 nm) XRD data. Vertical blue lines correspond to the matching peaks found by software Highscore, corresponding to Zincite compound.

Table 21 – Highscore data analysis of AZO80 sample's XRD measurements. Colour pattern for comparison purposes.

Peak colour	Compound	Chemical formula	Phase
Blue	Zincite	Zn_2O_2	Hexagonal

Peak analysis reveals that the most intense reflections occur for the (010) and (110) planes, corresponding to Zincite compound, *2θ* of 31.8º and 56.8º respectively. Peaks with *2θ* of 34.5º and 36.3º correspond to the Zincite compound as well, planes (002) and (011) respectively.

Other peaks present in three of the XRD measurements (samples AZO40, AZO105 and AZO160) have *2θ* angles of 37.8º, 40.7º and 44.1º. The first one might be vaguely related with the Ghanite compound ($Zn_8Al_{16}O_{32}$), plane (113). However, since it is the only matching peak with the compound, no relation can be established. The others have no peak match to the inserted chemical elements, which suggests that these peaks might be related with the sample holder or with the substrate, since these depend on the alignment of the system and on how much film is exposed. These assumptions are supported by the fact that the peaks are all in the same position and by the fact that one of the samples (AZO80) does not present any peaks unrelated to the ZnO compound.

Peaks with *2θ* of 31.8º, (010), and 34.6º, (002), are very common in the literature [31-33, 57, 86], and 56.8º, (110), is fairly common [31, 57, 86]. Peak with 31.8º, (010), is matched in the literature to the plane (100), which might be caused by a different axis reference of the software *Highscore*.

Table 22 lists the main peaks which are common to every sample.

Table 22 – Main peaks common to all ZnO:Al XRD's measurements.

Angle (*2θ*)	Compound name	Plane match (hkl) Reference code: 96-101-1259	Plane match in the literature (hkl)
31.8º	Zincite	(010)	(100)
34.6º	Zincite	(002)	(002)
36.5º	Zincite	(011)	(101)
56.8º	Zincite	(110)	(110)

These four peaks will be further analysed concerning the grain size and the crystal structure of the hexagonal phase of the Zincite compound. To this purpose, three equations will be used: Bragg's law, hexagonal structure equation and Sherrer equation. Both Bragg's law and equation for the hexagonal structure equation will be used compare the interplanar distances and the crystal structure parameters with those provided by the *Highscore* database in order to look up for small deviances which might be evidence of existing residual tensions of traction or compression in the samples.

7.4.1   Bragg's law

Table 23 show the values of the interplanar distances, *d*, both calculated with Bragg's law and extracted from the *Highscore* database matches, for each of the four chosen peaks, of every ZnO:Al sample. Different colours for each peak are presented to ease inter-peak comparisons.

Table 23 – Interplanar distances, d, calculated from Bragg's law for each main peak of every sample. Comparison with Highscore data. Colour pattern for comparison purposes.

Sample	Angle (2θ)	Calculated d(nm)	Database d(nm)
AZO40	31.8º	0.281	0.280
	34.5º	0.260	0.260
	36.6º	0.245	0.246
	56.8º	0.162	0.162
AZO80	31.8º	0.281	0.281
	34.5º	0.260	0.260
	36.3º	0.247	0.248
	56.7º	0.162	0.162
AZO105	31.8º	0.281	0.279
	34.5º	0.260	0.260
	36.6º	0.246	0.248
	56.9º	0.162	0.162
AZO160	31.8º	0.281	0.280
	34.6º	0.260	0.260
	36.5º	0.246	0.248
	56.7º	0.162	0.162

Bragg's law results will be analysed along with the hexagonal structure equation results in the next section.

7.4.2 Hexagonal structure equation

The hexagonal structure equation allows the calculation of the crystal structure parameters with the values of the interplanar distance, d, and the Miller indexes of the given plane (hkl), and is represented by equation 30 [8]:

$$\frac{1}{d^2} = \frac{4}{3}\left(\frac{h^2 + h*k + k^2}{a^2}\right) + \frac{l^2}{c^2} \qquad \textit{Eq. 30}$$

, where d stands for the interplanar distance, h, k and l are the Miller indexes of the given plane and a, b and c represent the crystal structure parameters. This equation allows the direct calculation of the crystal structure parameters. If both h and k equal zero, c can be extracted from l, and a and b (which are equal in the hexagonal structure) can be extracted from h and k when l equals zero. Equations 31 and 32 sum these conditions [8]:

$$a = \sqrt{\frac{4}{3}} * d\sqrt{h^2 + hk + k^2}, \qquad l = 0 \qquad\qquad \text{\textit{Eq. 31}}$$

$$c = l * d, \qquad h = k = 0 \qquad\qquad \text{\textit{Eq. 32}}$$

Table 24 shows the values of the hexagonal structure parameters, both calculated with equations 31 and 32, and extracted from the *Highscore* database matches, which are presented in the left column. Different colours for each peak are presented to facilitate interpeak comparisons.

Table 24 – Calculated hexagonal structure parameters for each peak of every sample. Highscore hexagonal structure parameters in the left, along with the respective sample. Colour pattern for comparison purposes.

Sample/ Database structure parameters	Angle (2θ)	Calculated a/b (nm)	Calculated c (nm)
AZO40	31.8°	0.325	0
	34.5°	0	0.521
a=0.322	36.6°	-	-
c=0.521	56.8°	0.324	0
AZO80	31.8°	0.325	0
	34.5°	0	0.520
a=0.322	36.3°	-	-
c=0.517	56.7°	0.325	0
AZO105	31.8°	0.325	0
	34.5°	0	0.520
a=0.322	36.6°	-	-
c=0.521	56.9°	0.324	0
AZO160	31.8°	0.325	0
	34.6°	0	0.518
a=0.323	36.5°	-	-
c=0.518	56.7°	0.325	0

All interplanar distance and hexagonal structure parameter calculated values match the ones retrieved from *Highscore* database matching system with an error below 1 %. One can thus conclude the veracity of the peak correspondence, stating that the planes retrieved from *Highscore* correspond to the peaks obtained from the XRD data collection. These results further evidence the presence of ZnO in the hexagonal phase in every sample.

7.4.3 Sherrer equation

Sherrer equation is one of the most common methods to approximately calculate the mean size of the crystallites of a sample. It is important to note that the definition of crystallite stands for an ordered crystalline domain, and not necessarily the size of the grain itself. It is described by the following equation 33:

$$\tau = \frac{K * \lambda}{\beta * \cos\theta} \qquad \text{Eq. 33}$$

where τ stands for the mean size of the crystallite, K is a shape factor, λ is the wavelength of incident radiation, β represents the full width at half maximum of the peak and θ is the Bragg's angle. All these parameters are fetched from the XRD data collected. Given so, λ equals $1.5418*10^{-1}$ nm, K is most commonly taken as 0.9, and the rest of the parameters will depend on the Miller indexes of each plane's peak [109].

The calculations were performed for the four selected angles corresponding to 2θ of 31.8º, 34.5º, 36.6º and 56.8º. The peak corresponding to of 31.8º confirmed an interesting result from the literature, which relates the crystallite size of the (010) orientation with the resistivity of the samples [84]. The calculations for the other peaks showed no trends, and are more unreliable due to their low FWHM, thus only this peak's analysis will be presented here.

Table 25 shows the Sherrer equation results for the 31.8º peak for each sample, related to a (010) plane orientation, and their relation with the resistivity of the samples.

Table 25 – Calculated mean size of the crystallites for 2θ peak of 31.8º for the AZO samples and the respective sample's resistivity.

Sample	τ (nm)	Resistivity (Ω.cm)
AZO40	52.5	$5.45*10^{-3}$
AZO80	105.0	$3.63*10^{-3}$
AZO105	93.3	$3.69*10^{-3}$
AZO160	59.9	$5.24*10^{-3}$

It is very interesting that the longer the crystallite domain size along the plane (010), the lower the resistivity of the sample. This relationship is extrapolated in the literature [84], but it does not seem to be broadly acknowledged. A further interpretation can be performed, by linking the lower resistivity of the AZO80 and AZO105 with its thickness of approximately 400 nm, which is the optimized thickness for the ZnO:Al layer for CIGS solar cells found in the literature.

8.   CIGS SOLAR CELLS RESULTS

Four solar cells were grown to test the optimized CdS and ZnO:Al layers in this work. Three solar cells were used to test the CdS layer, with three different sets of deposition parameters, and one solar cell was used to test the ZnO:Al layer. All the remaining layers and the grids were grown in Uppsala, following the deposition techniques mentioned in chapter 3 *Cu(In,Ga)Se₂ solar cell*. The scribing of the cells within each solar cell was made to achieve cell areas of 1 cm^2.

For the three CdS depositions on CIGS cells, the CdS was grown at the same time in both Uppsala's CIGS cell and a Mo substrate, using the two-sample holder, in order to measure the thickness of the layer. One of these samples, sample C, was grown and characterized, but will not be introduced in this work due to excessive fluctuations in every measurement performed, possibly due to fabrication complications.

Table 26 shows the parameters for the respective layer deposition for each solar cell sample and the thicknesses of both expected thickness of the ZnO:Al layer (through the fit presented in chapter 7.1.2 *Thickness assessments*) and measured from the solar cell's respective Mo substrate duplicate.

Table 26 – Solar cell samples' developed layer, with respective deposition technique, deposition parameters and thickness measured in the duplicated sample.

Solar Cell sample	Grown layer/ deposition method	Parameters/notes	Thickness (nm)
A	ZnO:Al (ALD)	220 supercycles 20:1	950 (expected)
B	CdS (CBD)	Default deposition	59
D	CdS (CBD)	65ºC outer bath temperature; 13.5ml ammonia.	210

Solar cell A's ZnO:Al sample was deposited with 220 supercycles with Zn:Al ratio of 20:1, and so the expected thickness for this layer through the linear fit is 950 nm.

Solar cell B was deposited with default parameters, and its measured thickness of 59 nm was anticipated. Solar cell D was grown with the same deposition parameters as S7-3, from chapter *5.2.7 Series 7 – Two parameter variation*, and its thickness matches perfectly with the twin sample from S7.

Figure 61 depicts the grown samples in the Mo substrates.
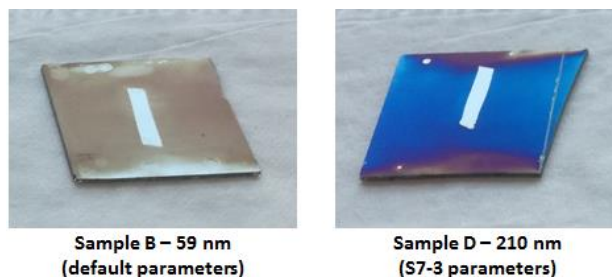
Figure 61 – CdS layers grown in Mo, during the CdS deposition of solar cells B and D. Middle marks correspond to the taped areas for thickness measurements.

From the colour-thickness pattern stipulated in chapter 5.3 *Colour-thickness relation*, the colour-thickness correlation stands within expectations.

It is important to note that the growth of the CdS layer onto CIGS is different from the growth of the same CdS onto a Mo sample. The thickness gradient with the variation of the different parameters should present the same kind of behaviour, i.e. linear with time, inverted with increasing ammonia, etc. For each parameter variation, a small offset is expected on the parameters of the respective tendency curve.

8.1 *J-V* curves

J-V curves were measured for some cells within each sample, under illumination and in the dark.

8.1.1 ZnO:Al – solar cell A

Figure 62 shows the *J-V* curves measured for two solar cells from sample A, A1 and A2.
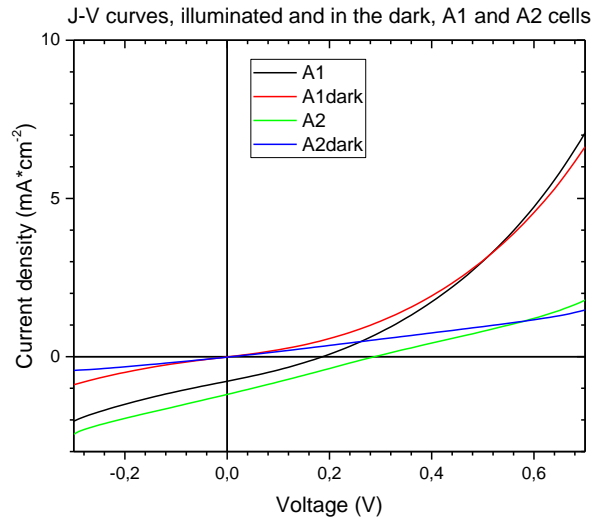
Figure 62 – J-V curves (illuminated and dark) of two cells within sample A, A1 and A2.

Sample A had two cells, A1 and A2. Cell A1 presents V_{oc} and J_{sc} values of 0.19 V and -0.78 mA.cm^{-2}, while cell A2 presents values of 0.290 V and -1.20 mA.cm^{-2} respectively. These results correspond to FF values of 0.29 for cell A1 and 0.26 for A2, and respective efficiencies of 2 % and 4.4 %. Solar cell A presents thus very poor photovoltaic effect.

These results might be a consequence of an overheat of the CIGS absorber layer during the ALD deposition process. As mentioned in chapter 5.2.1 *ZnO:Al growth by atomic layer deposition*, the whole deposition is performed at a temperature of 150º C under vacuum conditions, and this deposition of 220 supercycles of 20:1 Zn:Al monolayer ratios took about more than 24 hours. It is well known that CIGS is a fairly sensitive semiconductor and these conditions appear to be detrimental for the solar cell performance.

The overheat issue is not reported in literature's work of the development of ZnO:Al layers by ALD. The major overheating problem is probably due to the necessity of long purging times because of the scale of the deposition chamber. Further growths of thicker ZnO:Al will only be possible with an optimization of the ALD setup process. This might imply a development of new recipes for the ZnO:Al deposition by ALD, concerning purging times, deposition temperatures and possibly new reactants to allow the changing of the previous parameters. This way, a full study on the ZnO:Al deposition system is further required. Otherwise, this technique will be left aside for future work and replaced with the conventional sputtering.

Figure 63 and 64 shows the *J-V* curves, both under illumination and in the dark, of two cells within sample B (B2 and B4) and two cells within sample D (D6 and D8), respectively.
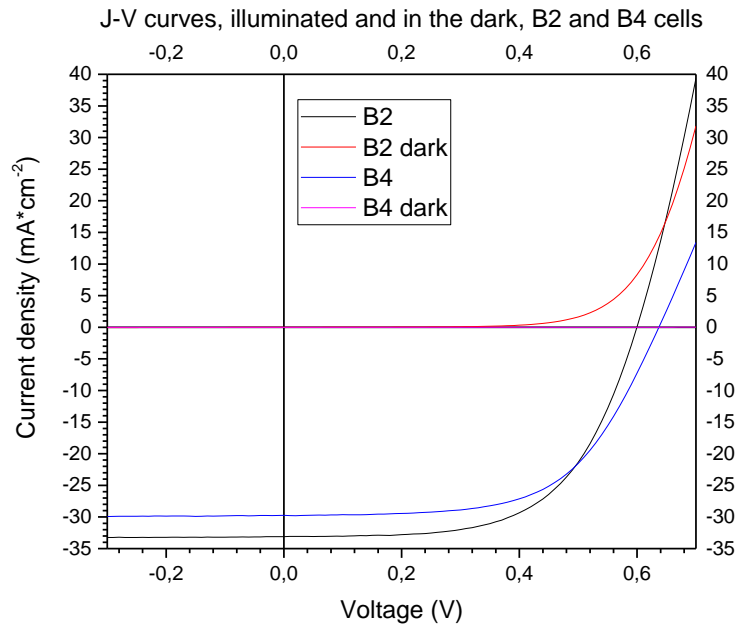
Figure 63 – J-V curves (illuminated and dark) of two cells within sample B, B2 and B4.
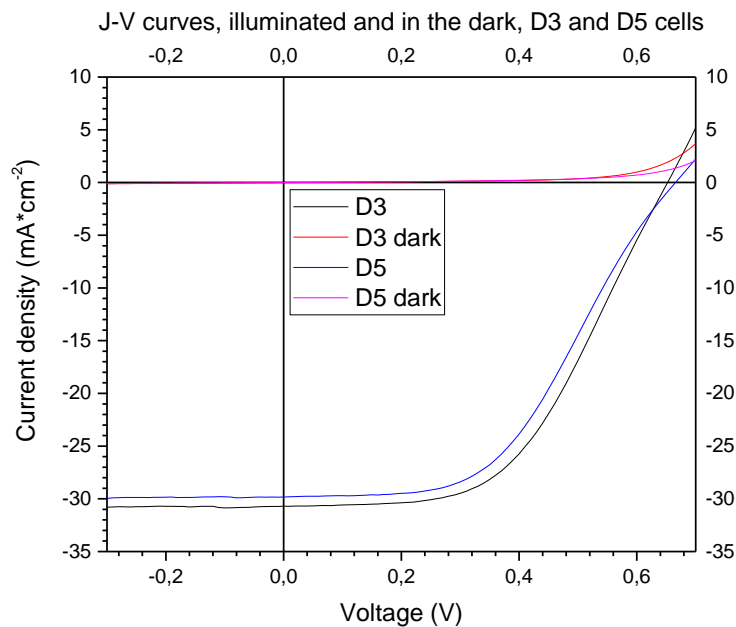
Figure 64 – J-V curves (illuminated and dark) of two cells within sample D, D3 and D5.

Cells B2 and B4 present V_{oc} and J_{sc} values of 0.599 V and -33.11 mA.cm^{-2}, 0.637 V and -29.74 mA.cm^{-2}, respectively. Concerning D3 and D5, values of 0.652 V and -30.69 mA.cm^{-2}, 0.666 V and -29.82 mA.cm^{-2}, respectively.

Table 27 displays averaged solar cell parameters, amongst inner individual cells, for samples B and D.

Table 27 – Solar cell parameters of samples B and D. Averaged cell values for each solar cell sample: 5 inner cells for sample B, 2 inner cells for sample D.

Sample	V_{oc} (V)	J_{sc} (mA.cm^{-2})	η (%)	FF
B (59 nm)	0.618	31.43	11.6	0.60
D (210 nm)	0.658	29.83	9.8	0.50

With increasing thickness for the CdS layer, the solar cells present increasing V_{oc}, but decreasing J_{sc}, efficiency and fill factor. Sample B, with the CdS layer deposited with the default parameters from the calibrating experiment, presents the higher efficiency of approximately 11.6 % and fill factor of 0.6, with thickness within the desired range of 59 nm.

8.2 External quantum efficiency

For sample A no EQE was measured, given such low values for fill factor and efficiency. Figure 65 graphically represents the data retrieved from the external quantum efficiency measurements for samples B and D.
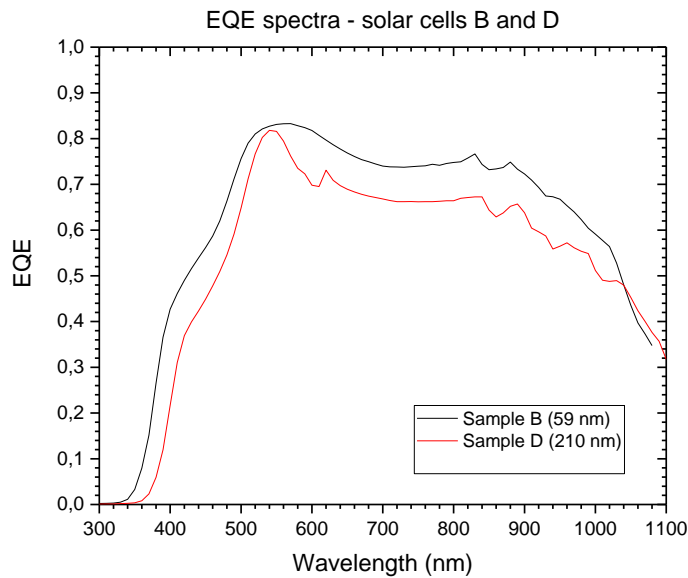
Figure 65 – External quantum efficiency spectra of samples B and D.

Sample B presents higher EQE than sample D throughout the entire spectra. The slope between 400-500 nm is an indicator of the thickness of the CdS layer, i.e. the EQE signal is lower for lower CdS thickness, and so this spectra's range match qualitatively with the CdS thicknesses obtained.

A thicker CdS layer not only absorbs more light but, since it has a poor value of hole mobility, leads to electrical losses due to recombination of photo-generated holes in the CdS region. Therefore, the behaviour of solar cell D is expected in terms of EQE(λ) and FF, as its CdS layer has a thickness value of 210 nm.

Despite the efforts to obtain a solar cell fully grown by Uppsala with the Mo/CIGS stack from the same batch as the used in this thesis, for a comparison of the CdS developed in this work with theirs, the saved solar cell was compromised due to technical reasons and thus no comparison was performed with such a sample.

Literature EQE(λ) plots of solar cells with higher efficiency naturally present more elegant spectra (more squared spectra) [1, 2, 66]. Nevertheless, the obtained results are good given that it was possible to compare solar cells grown with different CdS thicknesses, and the ZnO:Al grown by ALD was proven to damage the solar cell performance.

Moreover, the fact that the samples were subjugated to many different atmospheric conditions and the fact that, in the meantime, other optimizations are being performed on every layer, better solar cell results are anxiously expected in future developing works.

9. CONCLUSIONS

The objective of this thesis was twofold: firstly, to develop a CBD system for CdS and to evaluate the influence of the deposition parameters on the film properties; secondly, to evaluate if ALD can be used to deposit ZnO:Al layers to be used in thin film solar cells. With regards to the CBD, a detailed study highlighted the most important parameters for a precise control of the film thickness. An exhaustive characterization of ALD-deposited films showed limitations that make this technique still not mature enough to be used in CIGS solar cells.

Several series of CdS depositions by CBD permitted to infer on the influence of several parameters on the thickness of the layer. The evolution of the bath temperature experiment allowed to establish a near-logarithmic evolution of the deposition bath temperature overtime. A successful reproducibility series was performed, from which a standard contact profilometer thickness measure error of 15 nm was estimated for this series' samples. The parameters were successfully altered one at a time, providing an individual evaluation of each one of them. The fastening of the chemical reactions was directly linked with an increase of the time and temperature of the deposition and with the decrease of ammonia, indirectly bond with the increase of the acidity of the deposition bath. The amount of cadmium acetate was related with the saturation of the chemical reactions, not implying a thickening of the sample with increasing cadmium acetate, but indicting a possible higher compaction of the film.

A colour relation was established to allow a naked-eye estimative of the sample's thickness by colour appearance. GIXRD confirmed the presence of the CdS cubic phase, evidencing the polycrystalline nature of the films. The anticipated relation between the thickening of the samples and an increase of both average particle size and area covered by the particles was confirmed with *ImageJ* analysis on the optical spectroscopy imaging. This analysis was corresponded with the transition from a dominant ion-by-ion deposition to a dominant cluster-by-cluster deposition during the CBD. Most importantly, the objective of achieving 50-70 nm thick CdS buffer layer was accomplished, using default parameters described throughout the chapter *6 CdS results*.

Four ZnO:Al thin film samples of were grown, and several results were compared with a state-of-the-art 240 nm sample prepared by RF-sputtering. Two compositional concentrations were tested: $ZnO:Al_2O_3$ cycle ratios of 20:1 and 15:1. Optical spectroscopy revealed an average transmittance above 91 % from wavelengths ranging from 450-1200 nm. The transmittance

spectra allowed to perform thickness calculation of the samples, which were confirmed with a later etching and contact profilometry measurements, with very closely reliable results. Bandgap energy values were also calculated from the optical transmittance spectra, confirming an increase of the bandgap energy with the amount of aluminium of the sample, from 3.39 eV (20:1 Zn:Al ratio) to 3.44 eV (15:1 Zn:Al ratio). The deposition rates estimated were considerable higher than usual, and indicated possible errors while measuring the thickness of the thicker sample. Sheet resistivity measurements showed lower results with the increase of the thickness, as expected. The sample with best sheet resistivity was the thickest sample (735 nm) with 78.4 $\Omega.\square^{-1}$. When compared with the state-of-the-art ZnO:Al layer deposited by TF-sputtering, the ALD films present higher transmission, but present lower resistivity, which can be related with a lower doping concentration.

SEM and AFM showed a uniform grain distribution, morphology and smooth roughness throughout all the samples. XRD confirmed the presence of the zinc oxide compound in the hexagonal phase. Bragg's law and hexagonal structure equation allowed to extrapolate the smoothness of the growth due to the relation of the small peak position deviation with the lack of lattice stress forces. Sherrer equation allowed to relate the decrease of the layers' resistivity with the increase of the grain domains through the plane (010).

CdS and ZnO:Al layers were separately inserted in CIGS solar cells grown at Uppsala University, and all solar cells were characterized concerning *J-V* curves and external quantum efficiency. The ZnO:Al grown by ALD solar cell was severely damaged, presumably due to the long exposure to high temperatures during the ALD deposition. These results show that the ALD setup used in this thesis is not suited for the deposition of the ZnO:Al layer on CIGS solar cells, despite the excellent ZnO properties of the layers that were deposited individually. The best solar cell with CdS layer from this work, with a thin CdS layer, resulted in fill factor and efficiency values of 0.6 and 11.6 %, and its EQE(λ) shows better overall features throughout the whole spectrum.

10. FUTURE WORK

Concerning the CdS buffer layer and its setup, the samples' reproducibility with the desired thickness was achieved. The most important aspect that can be improved to assure a better reproducibility is the acquisition of a more accurate scale, as the powder weight measurements can be improved. Nevertheless, many aspects can be studied, and further characterization can be performed. For the same thickness, many parameters can be simultaneously calibrated. For example, higher deposition temperatures and ammonia quantities can be easily counterbalanced to achieve the 50-70 nm thickness CdS layer, and could ultimately result with better solar cell performances. However, such studies could only be performed after obtaining the results achieved in this thesis. Other parameter that can be further studied is the cadmium acetate quantity. A cadmium saturated deposition is presumed to lead to films with higher conformity, which can be studied in order to check on its influence. Furthermore, many efforts have been taken for a better understanding of the physical properties that give rise to the performance improvement of the CIGS solar cells, provided by the CdS buffer layer. One can study the influence of the dominant deposition process, ion-by-ion or cluster-by-cluster, by varying several parameters, and by checking the relation between CIGS solar cells that incorporate such grown cells with SEM and AFM imaging of the individually grown samples.

As for the ZnO:Al TCO, a proper study of this layer's properties in order to develop a baseline deposition process would require two steps: i) more sample growths and parameter variations; ii) the development of new chemical recipes for the deposition of ZnO:Al, with lower deposition temperatures and equally good (or better) optical and electrical properties of the resulting film. The current limitations are the high deposition temperature and time, and thus new processes have to overcome such limitations.

Most of all, next works would require more solar cells to grow these layers on in order to analyse the influence of the under develop layers on the solar cells electrical performance. It would be essential to obtain more Mo/CIGS stacks to perform a regular Uppsala's baseline growth and to obtain a reference sample that allows for a direct comparison of the grown CdS layers with a standard one as well. It would be most suitable to be able to grow the whole CIGS solar cell stack at INL, layer after layer with as small time difference between depositions as possible, to avoid oxidation or damage of the separated layers. The Mo substrates are obtainable, the CIGS absorber layer is under development and the remaining layers can be grown as well: CdS by CBD, i-ZnO and ZnO:Al with sputtering. Initial efforts to develop a

metallic grid were performed through inkjet printing, and silver nanoparticle inks were obtained, but further understanding of both the equipment and the technique are lacking and need to be obtained.

REFERENCES

[1]   P. Jackson et al, (2016). *Effects of heavy alkali elements in Cu(In,Ga)Se2 solar cells*. Frankfurt, Germany. Phys. Status Solidi RRL, **10**, No. 8, 583-586.

[2]   Lindahl et al, (2013). *Inline Cu(In,Ga)Se2 Co-evaporation for High-Efficiency Solar Cells and Modules*. IEEE Journal of Photovoltaics, Vol 3, No. 3, 1100-1105.

[3]   K. Sharp and F. Matschinsky, (2015). *Translation of Ludwig Boltzmann's paper "On the Relationship between the Second Fundamental Theorem of the Mechanical Theory of Heat and Probability Calculations Regarding the Conditions for Thermal Equilibrium"*. Entropy, **17**, 1971-2009.

[4]   M. Plack, (1914). *The theory of heat radiation, second edition*.

[5]   A. Einstein, (1990). *The Collected Papers of Albert Einstein, Volume 2: The Swiss Years*.

[6]   N. Bohr, (1913). *On the Constitution of Atoms and Molecules, Part II Systems Containing Only a Single Nucleus*.

[7]   (Edited from) http://141.7.70.48/images/theory_abb3.gif. Consulted in 07/10/2016.

[8]   C. Kittel, (2005). *Introduction to Solid State Physics*, Eighth edition.

[9]   Y. Hahn, (1997). *Electron-ion recombination processes – an overview*. Rep. Prog. Phys. **60**, 691-759.

[10]   (Edited from) http://www.thequartzcorp.com/en/blog/2014/09/15/cell-lifetime-and-recombination-part-i/91, *Cell Lifetime and Recombination, Part I*. Consulted in 07/10/2016.

[11]   A. G. Milnes, (1970). *Heterojunctions and Metal Semiconductor Junctions*.

[12]   (Edited from) http://hyperphysics.phy-astr.gsu.edu/hbase/solids/imgsol/pn2.gif. Consulted in 07/10/2016.

[13]   (Edited from) Notes from Professor Pedro Alpuim, *Instrumentation and Dispositives*, Master in Applied Physics, 2nd semester, Universidade do Minho.

[14]   P. Hersch and K. Zweibel, (1982). *Basic Photovoltaic Principles and Methods*. SERI/SP-290-1448.

[15]   J. Lindhal, (2015). *Atomic layer deposition of zinc tin oxide buffer layers for Cu(In,Ga)Se2 solar cells*. PhD dissertation, Uppsala University, 106 pages.

[16]   (Edited from) P. S. Priambodo et al., (2013). *Chapter book: Solar Cell Technology*, INTECH Open Access Publisher, ISBN 978-953-307-316-3.

[17]   L. W. Turner, (1976). *Electronics Engineer's Reference Book*. 4th Edition, Newnes.

[18]   J. Sterner, (2004). *ALD Buffer Layer Growth and Interface Formation on Cu(In,Ga)Se₂ Solar Cell Absorbers*. PhD dissertation, Uppsala University, 52 pages.

[19]   (Edited from) A. Chirilă et al., (2011). *Highly efficient Cu(In,Ga)Se₂ solar cells grown on flexible polymer films*. Nature Materials, Vol 10.

[20]   M. Bodegård, L. Stolt, J. Hedström J, (1994). *Proc. 12th Euro. Conf. Photovoltaic Solar Energy Conversion*. 1743-1746.

[21]   M. Bodegård, K. Granath, A. Rockett, L. Stolt, (1999). *Sol. Energy Mater*. Sol. Cells **58**, 199–208.

[22]   W. N. Shafarman, S. Siebentritt and L. Stolt, (2011), *Cu(In,Ga)Se₂ Solar Cells*. Integrated in A. Luque, S. Hegedus, (2011). *Handbook of Photovoltaic Science and Engineering, Second Edition*.

[23]   S. Wei, A. Zunge, (1998). *Appl. Phys. Lett*., **72**, 2011–2013

[24]   N. Khoshsirat and N. Yurus, (2016). *Copper-Indium-Gallium-diSelenide (CIGS) Nanocrystalline Bulk Semiconductor as the Absorber Layer and Its Current Technological Trend and Optimization*. Available in http://dx.doi.org/10.5772/64166.

[25]   A. E. Potter, Jr., R. Schalla, (1967). *Mechanism of cadmium sulfide film cell*. Lewis Research Center.

[26]   D. Lincot, R. Ortega-Borges, (1992). *Electrochem. Soc.* **139**, 1880-1889.

[27]   D. Hariskos et al., (2005). *Buffer layers in Cu(In,Ga)Se₂ solar cells and modules*. Thin Solid Films, 480-481, 99-109.

[28]   F. Larsson, (2015). *Study of CVD deposited i-ZnO layers in CIGS thin film solar cells*. Dissertation, Uppsala University, 38 pages.

[29]   A. E. Delahoy and S. Guo, (2011), *Transparent Conducting Oxides for Photovoltaics*. Integrated in A. Luque, S. Hegedus, (2011). *Handbook of Photovoltaic Science and Engineering, Second Edition*.

[30]   C. I. Bright, (2007). *Review of Transparent Conductive Oxides (TCO)*. 3M Company, 2008 Fall Bulletin.

[31]   Banerjee et al., (2010). *Structural, electrical, and optical properties of atomic layer deposition Al-doped ZnO films*. Journal of Applied Physics, **108**, 043504.

[32]   Dasgupta et al., (2010). *Atomic Layer Deposition of Al-doped ZnO films: Effect of Grain Orientation on Conductivity*. Chem. Mater., Vol. 22, No. 16.

[33]   W. J. Maeng et al., (2011). *Studies on optical, structural and electrical properties of atomic layer deposited Al-doped ZnO thin films with various Al concentrations and deposition temperatures*. J. Phys. D: Appl. Phys., **44**, 445305.

[34] M. Shabana, M. Saleh, M. Soliman, (1989). *Optimization of grid design for solar cells at different illumination levels*. Solar Cells, 26, 177-1

[35] L. Wen et al., (2010). *Optimization of grid design for solar cells*. Journal of Semiconductors, Vol. 31, No. 1.

[36] J. M. Delgado-Sanchez et al., (2017). *Front contact optimization of industrial scale CIGS solar cells for low solar concentration using 2D physical* modelling. Renewable Energy, **101**, 90-95.

[37] D. Abou-Ras et al., (2005). *Structural and chemical investigations of CBD- and PVD-CdS bufferlayers and interfaces in Cu(In,Ga)Se$_2$-based thin film solar cells*. Thin solid Films, 480-481, 118-123.

[38] B. S. Moon, et al., (2006). *Comparative studies of the properties of CdS films deposited on different substrates by R.F. sputtering*. Thin Solid Films, 511–512, 299–303.

[39] H. J. Muffler, et al., (2001). *ILGAR – A novel thin-film technology for sulfides*. Solar Energy Materials & Solar Cells, **67**, 121-127.

[40] N. Naghavi et al., (2010). *Buffer layers and transparent conducting oxides for chalcopyrite Cu(In,Ga)(S,Se)$_2$ based thin film photovoltaics: present status and current developments*. Prog. Photovolt. Res. Appl., **18**, 411-433.

[41] Nakada T, Kunioka A, (1999). *Appl. Phys. Lett.* **74**, 2444–2446 (1999).

[42] K. Ramanathan et al., (1998). *Proc. 2nd World Conf. Photovoltaic Solar Energy Conversion*. Pp 477–482.

[43] A. Kylner, (1999). *J. Electrochem. Soc.* **143**, 1816–1823.

[44] R. F. Pierret, (2003). *Advanced Semiconductor Fundamentals, second edition*. Modular series on solid state devices, vol. 6.

[45] S. Kijima and T. Nakada, (2008). *High-Temperature Degradation Mechanism of Cu(In,Ga)Se$_2$-Based Thin Film Solar Cells*. Appl. Phys. Express, **1**, 075002.

[46] M. A. Contreras et al., (2002). *Optimization Of CBD CdS process in high-efficiency Cu(In,Ga)Se$_2$-based solar cells*. Thin Solid Films, 403-404, 204-211.

[47] J. P. Enriquez, X. Mathew, (2003). *Influence of the thickness on structural, optical and electrical properties of chemical bath deposited CdS thin films*. Solar Energy Materials & Solar Cells, **76**, 313-322.

[48] S. M. Shamim, S. Islam, Md F. Huq, Md. A. A. Jobair, (2015). *Design, performance analysis and efficiency optimization of copper indium gallium selenide (CIGS) solar cell*. European Scientific Journal, edition vol. 11, No. 6.

[49] H. Khallaf et al., (2008). *Characterization of CdS thin films grown by chemical bath deposition using four different cadmium sources*. Thin Solid Films, **516**, 7306-7312.

[50]   H. Zhan et al., (2015). *Preparation and properties of CdS thin films deposited by chemical bath deposition*. Optik, **126**, 1411-1414.

[51]   W. G. C. Kumarage et al., (2016). *Influence of Bath Temperature on CBD-CdS Thin Films*. Procedia Engineering, **139**, 64-68.

[52]   T. J. Coutts, J. D. Perkins, D. S. Ginley, T. O. Mason, (1999). *Transparent Conducting Oxides: Status and Opportunities in Basic Research*. 195th Meeting of the Electrochemical Society, Seattle, Washington.

[53]   H. Liu et al., (2010). *Transparent conducting oxides for electrode applications in light emitting and absorbing devices*. Superlattices and Microstructures, **48**, 458-484.

[54]   O. Madelung, (1996). *Semiconductors – Basic Data*. 2nd edition, Springer-Verlag, Berlin.

[55]   Y. Igasaki, H. Saito, (1991). *J. Appl. Phys.* **70**, 3613.

[56]   D. J. Lee et al., (2011). *Structural and Electrical Properties of Atomic Layer Deposited Al-Doped ZnO Films*. Adv. Funct. Mater., **21**, 448-455.

[57]   Mundle et al., (2012). *Electrical conductivity and photoresistance of atomic layer deposited Al-doped ZnO films*. J. Vac. Sci. Technol., 01A146.

[58]   C. H. Huang et al., (2011). *Comprehensive Characterization of DC Sputtered AZO Films for CIGS Photovoltaics*. Journal of The Electrochemical Society, **158** (5).

[59]   B. L. Williams et al., (2016). *The competing roles of i-ZnO in $Cu(In,Ga)Se_2$ solar cells*. Solar Energy Materials & Solar Cells, **157**, 798-807.

[60]   G. A. Kitaev and T. S. Terekhova, (1970). *Russ. J. Inorg. Chem.* **15**, 25.

[61]   M. Z. Najdoski, I. S. Grozdanov, and B. Minceva-Sukarova, (1996). *J. Mater. Chem.* **6**, 761.

[62]   M. Perakh and H. Ginsburg, (1978). *Thin Solid Films*, **52**, 195.

[63]   P. Pramanik and S. Bhattacharya, (1989). *Mater. Res. Bull.* **24**, 945

[64]   I. O. Oladeji and L. Chow, (1999). *Thin Solid Films*, **339**, 148.

[65]   H. Khallaf et al., (2009). *J. Phys. D: Appl. Phys.* **42**, 135304

[66]   P. M. P. Salomé et al., (2017). *CdS and $Zn_{1-x}S_xO_y$ buffer layers for CIGS solar cells*. Solar Energy Materials & Solar Cells, **159**, 272-281.

[67]   C. Schwartz et al., (2016). *Electronic structure study of the CdS buffer layer in CIGS solar cells by X-ray absorption spectroscopy: Experiment and theory*. Solar Energy Materials & Solar Cells, **149**, 275-283.

[68]   S. Lee et al., (2015). *Effect of annealing treatment on CdS/CIGS thin film solar cells depending on different CdS deposition temperatures*. Solar Energy Materials & Solar Cells, **141**, 299-308.

[69]   W. Witte et al., (2011). *Comparison of charge distributions in CIGS thin-film solar cells with ZnS/(Zn,Mg)O and CdS/i-ZnO buffers* Thin Solid Films, **519**, 7549-7552.

[70]   J.-f. Han et al., (2014). *TEM and XPS studies on CdS/CIGS interfaces* Journal of Physics and Chemistry of Solids, **75**, 1279-1283.

[71]   H. M. Khallaf, (2005). *Chemical bath deposition of group II-VI semiconductor thin films for solar cells applications*. PhD dissertation, University of Central California, 208 pages.

[72]   P. O'Brien and J. McAleese, (1998). *Developing an understanding of the processes controlling the chemical bath deposition of ZnS and CdS*. J. Mater. Chem., **8**, 2309-2314.

[73]   J. Y. Choi et al., (1998). *Properties of cadmium sulfide thin films deposited by chemical bath deposition with ultrasonification*. Solar Energy, Vol. 64, Nos 1-3, 41-47.

[74]   T. Suntola, J. Antson, inventors (1977). *Method for producing compound thin films*. Patent 4058430.

[75]   R. W. Johnson, A. Hultqvist, S. F. Bent, (2014). *A brief review of atomic layer deposition: from fundamentals to applications*. Materials Today, Vol. 17, No. 5.

[76]   R. L. Puurunen, (2005). *Surface chemistry of atomic layer deposition: A case study for the trimethylaluminum/water process*. J. Appl. Phys., Vol. 97, No. 12, 121301.

[77]   (Edited from) http://cnx.org/resources/730c627141ba4375f2dd67b40b7cda4931d4032f/graphics1.jpg. Consulted in 12/10/2016.

[78]   S.M. George, (2010). *Atomic Layer Deposition: An Overview*. Chem. Rev., **110**, 111–131.

[79]   M. Knez, K. Nielsch, L. Niinistö, (2007). *Synthesis and Surface Engineering of Complex Nanostructures by Atomic Layer Deposition*. Adv. Mater., **19**, 3425–3438.

[80]   A. Hultqvist, M. Edoff, T. Törndahl, (2011). *Evaluation of $Zn_xSn_{1-x}O$ buffer layers for $CuIn_{0.5}Ga_{0.5}Se_2$ solar* cells. Prog. Photovoltaics Res. Appl., **19**, pp 478–481.

[81]   A. Kosola, et al., (2003). *Effect of annealing in processing of strontium titanate thin films by ALD*. Appl. Surf. Sci., **211**, 102–112.

[82]   M. Ritala, J. Niinistö, (2009). *Chemical Vapour Deposition: Precursors, Processes and Applications*. Royal Society of Chemistry.

[83]   E. B. Yousfi et al., (2001). *Atomic layer deposition of zinc oxide and indium sulfide layers for $Cu(In,Ga)Se_2$ thin-film solar cells*. Thin Film Solids, **387**, 29-32.

[84]   G. Luca et al., (2011). *Aluminium-doped zinc oxide films grown by atomic layer deposition for transparent electrode applications*. J. Mater. Sci: Mater Electron, **22**, 1810-1815.

[85]   Z. Baji et al. *Al doped ALD ZnO for CIGS buffer layer*. 26th European Photovoltaic Solar Energy Conference and Exhibition.

[86]   T. Dhakal et al., (2012). *Transmittance from visible to mid infra-red in AZO films grown by atomic layer deposition system*. Solar Energy, **86**, 1306-1312.

[87]   (Edited from) http://www.warsash.com.au/suppliers/beneq.php. Consulted in 15/09/2016.

[88]   H. Q. Li, (1997). *The Common AFM* Modes. http://www.chemistry.uoguelph.ca/educmat/chm729/afm/details.htm. Consulted in 15/09/2016.

[89]   (Edited from) https://commons.wikimedia.org/wiki/File:AFM_schematic_(EN).svg. Consulted in 15/09/2016.

[90]   (Edited from) https://www.purdue.edu/ehps/rem/rs/sem.htm. Consulted in: 15/09/2016.

[91]   http://www.nanoscience.com/technology/sem-technology/. Consulted in: 15/09/2016.

[92]   A. Bogner et al., (2007). *A history of scanning electron microscopy developments: Towards "wet-STEM" imaging*. Micron, **38**, 390-401.

[93]   (Edited from) https://chemie.uni-paderborn.de/en/arbeitskreise/technische-chemie/cmp/facilities/fib/. Consulted in: 15/09/2016.

[94]   B. D. Cullity, (1978). *Elements of X-Ray Diffraction, second edition*. Addison-Wesley Publishing Company Inc.

[95]   C. Tams, N. Enjalbert, (2009). *The Use of UV/Vis/NIR Spectroscopy in the Development of Photovoltaic Cells*. PerkinElmer, Inc.

[96]   R. Swanepoel, (1983). *Determination of the thickness and optical constants of amorphous silicon*. J. Phys. E: Sci. Instrum., Vol. 16.

[97]   G. Franceschinis. *Surface Profilometry as a tool to Measure Thin Film Stress, A Practical Approach*. RIT MicroE Graduate Student.

[98]   http://www.nanoscience.com/technology/optical-profiler-technology/how-profilometer-works/. Consulted in: 16/09/2016.

[99]   (Edited from) http://pressurevesseltech.asmedigitalcollection.asme.org/article.aspx?articleid=1672011. Consulted in 17/09/2016.

[100]   F. M. Smits, (1957). *Measurement of Sheet Resistivities with Four-Point Probe*. The Bell System Technical Journal.

[101]   M. Rusu et al., (2013). *Optimization of the CBD CdS deposition parameters for ZnO/CdS/CuGaSe$_2$/Mo solar cell*. Journal of Physics and Chemistry of Solids, **64**, 1849-1853.

[102]   D. Fernando et al., (2015). *Control of the crystalline phase and morphology of CdS deposited on microstructured surfaces by chemical bath deposition*. Materials Science and Semiconductor Processing, **30**, 174-180.

[103]   E. Yücel, O. Sahin, (2016). *Effect of pH on the structural, optical and nanochemical properties of CdS thin films grown by chemical bath deposition*. Ceramics International, **42**, 6399-6407.

[104]   O. Vigil-Galán et al., (2016). *Optimization of CBD-CdS physical properties for solar cell applications considering a MIS structure*. Materials and Designs, **99**, 254-261.

[105]   L. Wang and J. Sun, (2013). *Molybdenum modified AISI 304 stainless steel bipolar plate for proton exchange membrane fuel cell*. J. Renewable Sustainable Energy, **5**, 021407.

[106]   H. Yoon et al., (2015). *Three-dimensional web-like fibrous CuInS$_2$ films*. Applied Surface Science, **351**, 588-593.

[107]   Z. Baji, (2013). *Compound semiconductor layers for optoelectronic and photovoltaic purposes*. PhD thesis, Budapest University of Technology and Economics, 95 pages.

[108]   M. Moret et al., (2014). *Atomic Layer Deposition of zinc oxide for solar cell applications*. Superlattices and Microstructures, **75**, 477-484.

[109]   A. L. Patterson, (1939). *The Sherrer Formula for X-Ray Particle Size Determination*. Physical Review, Vol. 56.
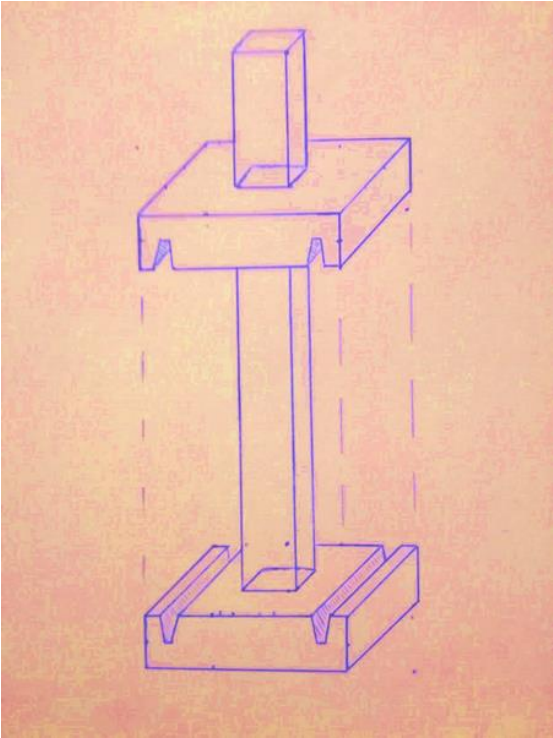
ANNEX I – CdS SUBSTRATE HOLDER DESIGN

Figure 66 – First sketch of the sample holder's design. Highlight on the middle column passing through the top piece. Contrast applied. Not to scale.
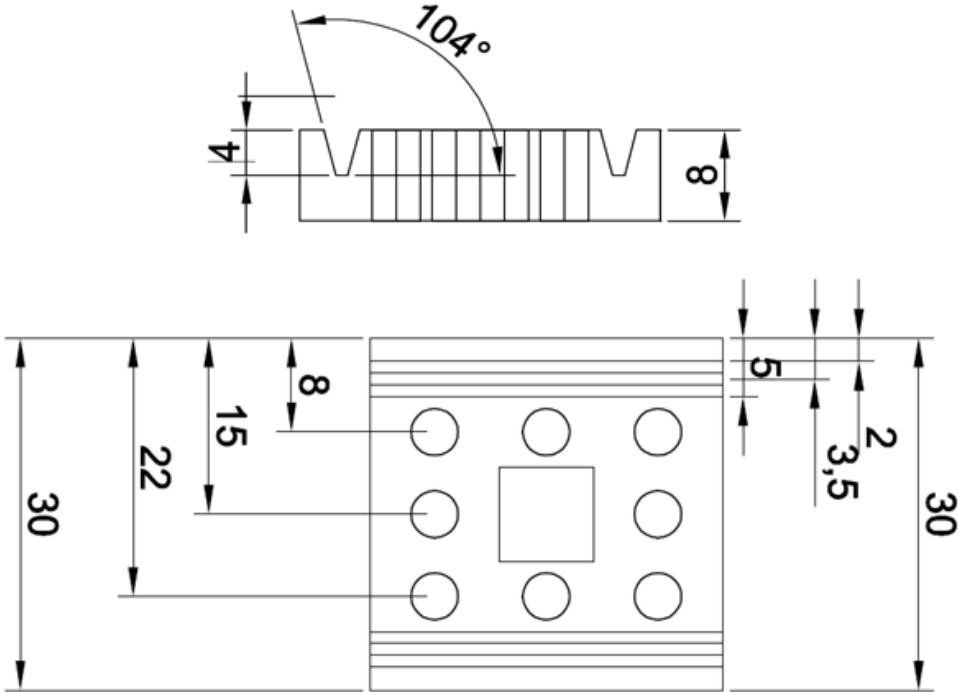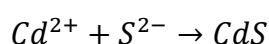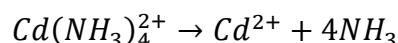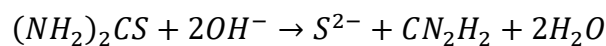

Figure 67 – Autocad imaging of the developed sample holder design. Rear-side design of the top and bottom parts of the sample holder (top). Base-side design of the top part of the holder (bottom). Scale in mm.

ANNEX II – CBD EXPERIMENTAL PROTOCOLE FOR CDS

"To produce CdS thin films, an alkaline solution of cadmium salt and a thiourea solution are prepared. The film growth takes place though ion-by-ion condensation of Cd^{2+} and S^{2-} ions on the substrate when Cd^{2+} and S^{2-} ions exist over the solubility limit (Lincot and Ortega, 1992). Typical reaction steps involving cadmium acetate are as follows:

$$(NH_2)_2CS + 2OH^- \rightarrow S^{2-} + CN_2H_2 + 2H_2O$$
$$Cd(NH_3)_4^{2+} \rightarrow Cd^{2+} + 4NH_3$$
$$Cd^{2+} + S^{2-} \rightarrow CdS$$

Sulfide ions are released by the hydrolysis of thiourea, but Cd^{2+} ions form tetraaminecadmium (II) complex ions by combining with NH_3 in the range of pH 10-11 (Rieke and Bentjen, 1993). These $Cd(NH_3)^{2+}_4$ complexes adsorb on the glass, then the heterogeneous nucleation and growth takes place by ionic exchange reaction with S^{2-} ions (Pavaskar et al, 1977). This process is called ion-by-ion process. In this manner, CdS is deposited in the form of transparent, uniform and adherent film. In contrast, CdS colloidal particles which precipitate randomly on thw growing film, and thus form opaque, non-uniform and poorly adherent "B-quality" films (Kaur et al., 1980; Lincot and Ortega, 1992). This is called a colloid-by-colloid process and usually happens at a later stage of the deposition."

Direct citation from: **J. Y. Choi *et. al.*, 1998.**

Inventory

- 3x150 ml beaker → 1 for the CdS deposition (labelled as "CdS-dep LaNaSC"); 1 for the cleaning (labelled as "for CdS cleaning") and 1 with deionized water (labelled as H2O).
- 2x25 ml beaker → 1 to measure 15 ml deionized water + 1 to measure ammonia.
- 1x100 ml beaker → to measure 85 ml deionized water, marked with "NH3".
- 2 flasks → 1x50 ml flask to dissolve the thiourea + 1x 25ml to dissolve the cadmium acetate.
- 2 funnels → 1 for the thiourea (marked with a "T") + 1 for the cadmium acetate (marked with a "Cd").
- 1 metal spatula → to apply and remove the tape from the sample.

- 2 disposable small boats + 2 disposable spatulas (for each deposition) → to measure the cadmium acetate and the thiourea.
- 1.33 g thiourea + 0.13 g cadmium acetate + ammonia (desired quantity, usually 10-20 ml).
- HCl → to clean the CdS contaminated equipment during the deposition.
- Deionized water → to clean the equipment (before and after usage).
- Sample holder → to hold the samples during the deposition.
- Ultra-sound → to fasten the dissolution of thiourea.
- Scale → to measure the powders.
- Lab coat + goggles + 2 pairs of gloves + mask → safety.

Step-by-step CdS deposition procedure

- Check the water level of the hot bath. Fill it until it reaches the 175ml mark of the deposition beaker (when under water). Heat the bath to the desired temperature (60ºC, takes about 30 minutes).
- Clean all the inventory needed to proceed with the deposition: 2 times with tap water, 3 times with deionized water.
- Measure the thiourea and cadmium acetate quantities (double pair of gloves and mask for safety guarantee):

1. Measure 15 ml of deionized water in the respective recipient.
2. Starting with thiourea, takes longer to fully dissolve: prepare the material for the thiourea measurement: 50ml flask with the big lid, funnel on top (marked with a "T"), 15 ml deionized water ready to use.
3. Measure 1.33 g of thiourea in a small boat with a disposable spatula and immediately dispose of the spatula to the solid waste container. Use the 15 ml deionized water, small quantities at a time, to help the powder into the flask. Clean as best as possible the small boat (with the 15 ml water) in order to minimize the wasted material and to stick to the desired quantity of thiourea for the deposition. Dispose of the small boat immediately into the solid waste container. Agitate the 50 ml flask (after carefully closing it) in all possible ways to dissolve the thiourea. Insert the thiourea flask into the ultrasound to improve the dissolution while the other steps are done.

Figure 68 – Powder measurement (left). Mixing the powder with deionized water (middle). Thiourea in the ultra-sound (right).

4. Measure 15ml deionized water in the respective recipient.

5. Prepare the material for the cadmium acetate measurement: 25 ml flask with the small lid, funnel on top (marked with a "Cd"), 15 ml deionized water ready to use.

6. Measure 0.13 g of cadmium acetate in a small boat with a disposable spatula and immediately dispose of the spatula to the solid waste container. Use the 15 ml deionized water, small quantities at a time, to help the powder into the flask. Clean as best as possible the small boat (with the 15 ml water) in order to minimize the wasted material and to stick to the desired quantity of cadmium acetate for the deposition. Dispose of the small boat immediately into the solid waste container. Agitate the 25 ml flask (after carefully closing it) in all ways possible to dissolve the cadmium acetate (must be much easier than the thiourea due to much smaller quantities).

Figure 69 – Sample holder with two samples facing each other

- Pick the substrate to deposit on, and carefully attach a small tape in the middle of the face of the substrate that you want to deposit the CdS on. Use the metal spatula to do so, easing the tape into the substrate and trying to leave no air in between. Place the substrate in the holder, tape facing the pole.

- Gather all material for the deposition to take place:

1. Measure 85 ml of deionized water in the 100 ml beaker (this one is marked with NH3, even though the ammonia won't be measured in this beaker).

2. Gather both flasks with dissolved thiourea and cadmium acetate.

3. Gather all beakers necessary for the deposition: 1 for the deposition (empty, marked with "CdS-dep LaNaSC), 1 for the CdS cleaning (half filled with deionized water,

marked with "for CdS cleaning"), and 1 to place the cleaned material (half filled with deionized water, marked with "H2O").

4. Gather the sample holder with the samples to deposit on near the deposition bath.

5. Prepare the 15 ml beaker to measure the ammonia desired quantity (marked with "NH3 LaNaSC"), and place the ammonia bottle next to it.

6. Gather the timer with the desired deposition time next to the bath.

7. Be sure that the bath temperature is already the desired.

8. Turn on the ventilation system of the hotte.

- When everything is set, measure the desired quantity of ammonia. Agitate the ammonia bottle before opening it.

- After measuring the ammonia, the deposition is ready to take place (goggles for guaranteed safety):
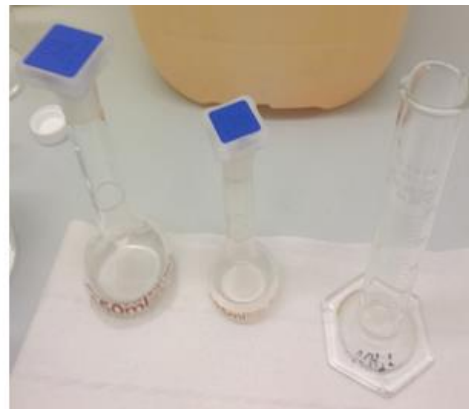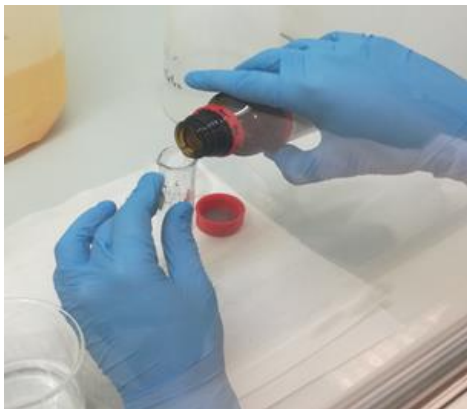

Figure 70 – Measuring the ammonia (left). Ammonia, cadmium acetate, thiourea, from the right (right).

1. Carefully pour all the liquids into the deposition beaker in the following specific order: Deionized water; Ammonia; Cadmium acetate; Thiourea.

2. Carefully place the deposition beaker in the middle of the bath. Insert the holder with the substrate at the same time that the deposition beaker contacts the bath. Click the timer.

3. Stir the solution for 10 seconds in the beginning of every minute (0-10 seconds, 60-70 seconds…). Stir it again when there are 75 seconds left (1 minute and 15s), for 10 seconds, and again where there are 30 seconds left, for 10 seconds. The stirring can be easily done by holding the holder downwards onto the beaker and circularly moving the
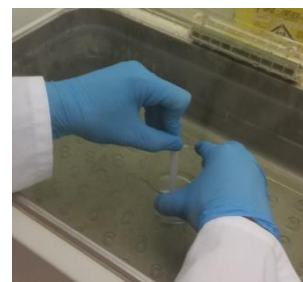

Figure 71 - Deposition beaker in the middle of the Outer Bath, stirring occurring.

beaker. Always pay attention to the substrate(s): they might move while the deposition occurs, be sure that the substrate never falls out of the holder.

4. Take the deposition beaker out of the hot bath when the timer rings.

5. Carefully take the holder with the samples out of the deposition beaker, and place it inside the cleaning beaker.

6. Take out the sample(s) out of the holder, one at a time, and jet it with deionized water in both sides. Clean it with pumping nitrogen, until it is fully dried. Put the sample in the sample box.
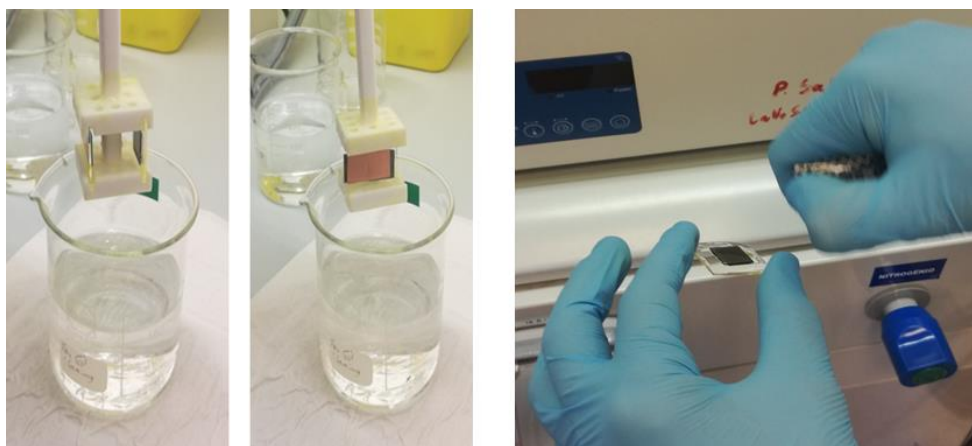

Figure 72 – Deposited samples dipping in deionized water, front and lateral views (left). Drying the deposited sample with pumping nitrogen.

- Start the cleaning process:

  1. Carefully pour the deposition solution (inside the deposition beaker) into the liquid waste container (marked with "CdS waste").

  2. Pour the HCl into the deposition beaker to clean it. Lean the beaker to fully clean the inside of the beaker. Leave the HCl inside the deposition beaker.

  3. Use the metal spatula to take the tape out of the sample. Put the tape into the solid waste container. Dive the spatula and the substrate holder into the HCl to clean them, and then put them into the H2O beaker.

  4. Carefully pour the content of the cleaning beaker into the liquid waste container. Pour the HCl from the deposition beaker into the cleaning beaker and carefully clean the inside of the cleaning beaker.

  5. After all the material is cleaned with the HCl (metal spatula, sample holder, cleaning beaker and deposition beaker), pour it again into the initial recipient (HCl is reusable).

  6. Carefully clean all the equipment used to measure all liquids and powders:

a. Carefully clean the ammonia 15 ml beaker inside and outside (some ammonia always drips from the outside while measuring it).

b. Carefully clean the thiourea 50 ml flask by half filling it with deionized water, closing it and agitating the deionized water inside, 3 times).

c. Carefully clean the cadmium acetate funnel with jet deionized water into the liquid waste container.

d. Carefully clean the cadmium acetate 25 ml flask by half filling it with jet water, closing it and agitating the deionized water inside (3 times). Carefully all content into the liquid waste container.

e. Clean all the remaining equipment with tap water (2 times) and deionized water (3 times).

2. Carefully clean the liquid waste container bottleneck with cleaning paper and put it into the solid waste container.

3. Turn off the ventilation system of the hotte.

4. Store all the equipment for the next deposition.